

Direct Numerical Simulation of a Confined Three-Dimensional Gas Mixing Layer with One Evaporating Hydrocarbon-Droplet Laden Stream

R.S. MILLER and J. BELLAN

Jet Propulsion Laboratory, MS 125-121, California Institute of Technology, Pasadena, CA 91109-8099

(Submitted to Journal of Fluid Mechanics)

Abstract

Direct numerical simulations are performed of a confined three-dimensional, temporally developing, initially isothermal gas mixing layer with one stream laden with as many as 7.3×10^5 evaporating hydrocarbon droplets, at moderate gas temperature and subsonic Mach number. Complete two-way phase couplings of mass, momentum and energy are incorporated which are based on a thermodynamically self-consistent specification of the vapor enthalpy, internal energy and latent heat of vaporization. Effects of the initial liquid mass loading ratio (ML), initial Stokes number (St_0), initial droplet temperature and flow three-dimensionality on the mixing layer growth and development are discussed. The dominant parameter governing flow modulation is found to be the liquid mass loading ratio. Variations in the initial Stokes number over the range $0.5 \leq St_0 \leq 2.0$ do not cause significant modulations of either first or second order gas phase statistics. The mixing layer growth rate and kinetic energy are increasingly attenuated for increasing liquid loadings in the range $0 \leq ML \leq 0.35$. The laden stream becomes saturated before evaporation is completed for all but the smallest liquid loadings due to: (1) latent heat effects which reduce the gas temperature, and (2) build up of the evaporated vapor mass fraction. However, droplets continue to be entrained into the layer where they evaporate due to contact with the relatively higher temperature vapor-free gas stream. The droplets within the layer are observed to be centrifuged out of high vorticity regions and to migrate towards high strain regions of the flow. This results in the formation of concentration streaks in spanwise braid regions which are wrapped around the periphery of secondary streamwise vortices. Persistent regions of positive and negative slip velocity and slip temperature are identified. The velocity component variances in both the streamwise and spanwise directions are found to be larger for the droplets than for the gas phase on the unladen stream side of the layer; however, the cross stream velocity and temperature variances are larger for the gas. Finally, both the mean streamwise gas velocity and droplet number density profiles are observed to coincide for all ML when the cross stream coordinate is normalized by the instantaneous vorticity thickness; however, first order thermodynamic profiles do not coincide.

1 Introduction

The ability to model and predict two-phase gas-liquid turbulent flows with evaporation is currently impeded by a relatively limited understanding of the underlying physics governing their evolution. In order to simplify the following analysis, we restrict the discussion to cases for which the dispersed phase: (1) has a relatively small and negligible volume fraction, (2) is composed of discrete, non-connected and approximately spherical droplets, (3) has negligible effects due to droplet collisions, breakup and coalescence, and (4) has no chemical reactions. Note that these restrictions do not limit the flow to small liquid mass loadings (ratios of liquid to gas phase densities are generally $\sim 10^3$), and are often applicable to the early stages of two-phase combustion for which the liquid must first be evaporated prior to reacting (e.g. Williams 1965[52]). Therefore, the present study is of interest to a variety of gas-liquid flows with both fundamental and applied relevance; e.g. spray mixing, spray

combustion, atomization, painting and weather prediction (see e.g. Elghobashi 1994[12]). Of particular interest to the investigation are the characterization of the droplet size and concentration distributions, as well as an elucidation of flow modulation due to phase couplings of mass, momentum and energy in a planar mixing layer configuration.

Evaporating dispersed droplet flows are expected to display many of the physical effects prevalent in solid particle flows which have received a much greater scrutiny due to their relatively simpler physics and mathematical descriptions. For example, it is well understood that solid particles tend to be centrifuged away from high vorticity regions and migrate into high strain ‘convergence’ regions of homogeneous turbulence (Squires & Eaton 1991[48]). This phenomena is referred to as ‘preferential concentration’ and has additionally been observed for a wide variety of flow configurations (see Eaton & Fessler 1994[11] for a review). The extent to which preferential concentration occurs depends on the ratio of the particle time constant to the relevant flow time scales (i.e. the Stokes number, St): Very small particles ($St \ll 1$) closely follow local flow motions and behave essentially as fluid elements, very large particles ($St \gg 1$) are predominantly unaffected by the flow due to inertial dominance; however, particles with intermediate Stokes numbers ($St \sim 1$) experience the combined influences of both the turbulence structures and finite velocity slip resulting in complex dispersion patterns (Wen, Kamalu, Chung & Crowe 1992[51]; Martin & Meiburg 1994[29]; Elghobashi 1994[12]).

It is also understood that solid particle flows can be described as either ‘one-way’ coupled, when the dispersed phase mass loading is small and the flow remains essentially unaltered by the particles, or as ‘two-way’ coupled when the loading is increased to the point at which the particles modulate the flow primarily through integrated particle drag effects (e.g. Elghobashi & Truesdell 1993[13]). Gore & Crowe (1989)[15] compiled results from a variety of experiments which suggest that solid particles can act to either dissipate or enhance turbulence energy depending on the diameter of the particles relative to the integral length scale of the flow; however, no conclusions could be drawn as to the magnitude of the modulation. Kulick, Fessler & Eaton (1994)[23] conducted experiments of a fully developed channel flow with solid particles mass loadings as large as 80%. It was observed that the fluid turbulence intensity was attenuated by the particles; however, the mean fluid velocity profile remained essentially unaltered for all cases. Their results also confirmed several previous investigations which find a larger streamwise velocity component variance for particles relative to the corresponding fluid intensity in inhomogeneous flows (e.g. Soo, Ihrig & El Kouh 1960[45]; Carlson & Peskin 1975[6]; Tsuji & Morikawa 1982[50]; Steimke & Dukler 1983[49]; Rogers & Eaton 1990[42]). This phenomena has been predicted theoretically in the presence of a constant mean velocity gradient by Liljegren (1993)[27].

In comparison with solid particle flows, evaporating dispersed droplet flows can be expected to incorporate all of the above physical effects, while simultaneously introducing additional complexities. In addition to the drag force which predominantly governs phase coupling in solid particle flows, turbulence modulation in evaporating droplet flows is also governed by both mass and thermal energy exchange between the gas and liquid phases (heat transfer is generally neglected for solid particles; however, latent heat effects should amplify the relevance of thermal energy transfer in the presence of evaporation). In addition, the rate at which evaporation occurs is determined by the local flow conditions, thereby making the droplet time constant a function of both time and space, even for initially monodisperse distributions (Mashayek, Jaber, Miller & Givi 1997[32]; Harstad & Bellan 1997[16]). This may significantly alter the overall preferential concentration and turbulence modulation for evaporating droplets relative to the analogous effects observed for solid particles.

The present study focuses on direct numerical simulations (DNS) defined as those in which all length and time scales of the gas phase flow are resolved without resorting to either time averaged or subgrid turbulence models. The ‘Eulerian-Lagrangian’ approach is adopted in which every individual droplet is tracked in a time accurate manner using a Lagrangian reference frame (in contrast to the ‘Eulerian-Eulerian’ approach which describes the dispersed phase as an interpenetrating continuum derived by averaging over sufficiently large local ensembles of droplets: e.g. Zhou 1993[55]; Elghobashi 1994[12]). Present day supercomputers have been instrumental in the success of DNS for simulating single-phase turbulent flows at all scales for sufficiently low Reynolds numbers; however, for two-phase gas-droplet flows they are still not powerful enough to simultaneously resolve the spatial

scales interior and adjacent to individual droplets when the spatial flow scales are much larger than the droplet diameter. In this case, the Lagrangian description therefore involves the solution of modeled transport equations for the individual droplet position vectors, velocity vectors, temperatures and masses. Generally, the drag force, heat transfer rate and evaporation rate are related to the local slip velocity, slip temperature and slip vapor mass fraction evaluated at the droplet position (Miller, Harstad & Bellan 1998[35]). Such models typically assume infinite thermal conductivity of the liquid, and are based on analytic Stokes/quiescent flow solutions combined with empirical correlations to account for finite droplet Reynolds number effects.

Obtaining DNS solutions of the Eulerian-Lagrangian two-phase flow equations can be extremely computationally intensive due to the large numbers of droplets/particles involved (DNS of solid particle laden homogenous turbulence presently tracks as many as 10^6 individual particles; e.g. Squires & Eaton 1990[47]; Squires and Eaton 1991[48]). In the presence of evaporation, numerical solutions are even more computationally intensive relative to solid particles due to both: (1) additional conservation equations for the droplet temperature and mass evolutions, and (2) the need to solve the compressible form of the gas phase equations which is necessary due to gas density sources (the evaporating drops). Miller, Harstad & Bellan (1998)[35] recently evaluated eight Lagrangian droplet models applicable to DNS from the perspective of both accuracy and computational efficiency. They included both equilibrium and non-equilibrium evaporation models and evaluated them through comparisons with a variety of single isolated droplet vaporization experiments. All models were found to perform nearly identically for low evaporation rates; however, for high evaporation rates in which the carrier gas temperature is larger than the liquid boiling temperature, substantial deviations among the various model predictions were observed. A comparison of various methods for evaluating properties showed that an assumption of constant properties provides both accurate and computationally efficient model predictions when the properties are evaluated at either the liquid wet bulb or boiling temperatures. They further found that non-equilibrium effects can become important for relevant initial droplet diameters ($< 50\mu m$) when the evaporation rate is sufficiently large, and therefore suggest a model based on the Langmuir-Knudsen evaporation law combined with an analytic heat transfer correction for evaporation effects.

At the present time, the extent of previous DNS investigations into the physics of evaporating droplet turbulent flows is quite limited. Mashayek, Jaber, Miller & Givi (1997)[32] performed DNS of isotropic, incompressible turbulence seeded with liquid droplets obeying the ' D^2 Law' (Spalding 1953[46]; Godsave 1953[14]). They studied the effects of the initial droplet time constant, the vaporization rate and the droplet Schmidt number on the evolution of the probability density function (PDF) of the ensuing droplet size distribution. They found that initially monodisperse droplet size distributions develop PDFs which tend towards Gaussian for intermediate times. The assumptions of that investigation were somewhat restrictive because only one-way coupling with an incompressible, isotropic and isothermal flow was considered. Mashayek (1998a)[30] and Mashayek (1998b)[31] later relaxed these restrictions and performed low Mach number DNS of both forced isotropic and homogeneous shear turbulence with complete two-way coupling. Mashayek derived the phase coupling terms for the gas energy equation under the assumption that the heat capacities of the liquid and the evaporated vapor are constant and equal. These simulations tracked as many as 5.5×10^5 individual droplets obeying a relatively simple 'mass analogy' evaporation model which is strictly valid only for low vaporization rates (Miller, Harstad & Bellan 1998[35]). Results from these studies illustrate the effects of the mass loading ratio, the initial droplet time constant, and several thermodynamic droplet parameters on the turbulence evolution, and suggest that evaporation can be prematurely halted due to elevated vapor mass fractions in the gas phase. Mashayek (1998b)[31] also confirmed that the streamwise velocity variance of the droplets is larger than that of the fluid for evaporating droplets in the presence of a uniform mean velocity gradient. The above mentioned evaporation studies confirm that effects of preferential concentration and turbulence modulation prevail for evaporating dispersed droplet flows, but with increased complexity with respect to solid particle flows due in large part to the evaporative formation of polydisperse size distributions.

The planar mixing layer configuration provides a relatively simple, non-homogeneous flow geometry which removes some of the restrictions imposed by homogenous turbulence studies. In particular, the growth, devel-

oment and pairing of large scale spanwise vorticity structures (Winant & Browand 1973[53]; Brown & Roshko 1974[5]) are known to play a strong role in both the layer's development and the transition to turbulence (Huang & Ho 1990[17]; Moser & Rogers 1991[37]), and also in the dispersion of solid particles (e.g. see Eaton & Fessler 1994[11] for a related review). Chein & Crowe (1987)[7] studied the effects of vortex pairing on solid particle dispersion in a planar shear layer simulated using a discrete vortex method. They found that particles with intermediate Stokes numbers in the size range $0.5 < St < 5$ may be laterally dispersed farther than fluid particles; an effect which is increased by vortex pairing. Lazaro & Lasheras (1989)[24], Lazaro & Lasheras (1992a)[25] and Lazaro & Lasheras (1992b)[26] conducted a series of low gas temperature planar mixing layer experiments in which one stream is seeded with water droplets. Their results confirm the observation of increased particle dispersion in the presence of acoustic flow forcing, whereas all particles are found to disperse at a smaller rate than the fluid momentum in the absence of forcing. Martin & Meiburg (1994)[29] performed two-dimensional (2D), inviscid mixing layer simulations with one stream laden with as many as 10^6 solid particles in the Stokes number range $10^{-2} < St < 10^2$. They traced the particles backwards in time and found that the most highly dispersed particles originated from inclined narrow bands within the braid regions. Their results also support previous findings by several of the above investigators, as well as by Wen, Kamalu, Chung & Crowe (1992)[51], Longmire & Eaton (1992)[28] (for a jet), Kiger & Lasheras (1995)[21] and Kiger & Lasheras (1997)[22], confirming the existence of particle concentration 'streaks' forming in braid regions between spanwise vortices (see also Crowe, Troutt & Chung 1995[10]). In a related issue, Kiger & Lasheras (1995)[21] found that the vortex pairing process has a homogenizing effect on the particle distribution. Kiger & Lasheras (1997)[22] used the same experimental facility to study turbulence dissipation due to particles and observed regions of persistent positive and negative slip velocity corresponding to accelerating and decelerating fluid regions, respectively. The above measurements have all been made for either solid particles or for water droplets in low temperature flows with negligible evaporation rates. Furthermore, all of the results are for small liquid mass loadings $\sim 1\%$ (i.e. one-way coupling), and are based on either 2D simulations or predominantly 2D experimental mixing layers. However, the effects of evaporation, two-way coupling and three-dimensional (3D) large scale flow structures are potentially important in general dispersed droplet mixing layers.

The primary objectives of the present investigation are to: (1) Provide a detailed derivation of all phase coupling terms for gas-droplet turbulent flows in the realistic case where the liquid and evaporate heat capacities and the molecular weights of the carrier gas and the evaporated vapor are not equal, and (2) Obtain DNS solutions of the governing equations for the case of a 3D planar gas mixing layer where one stream is laden with initially monodisperse hydrocarbon droplets (for a variety of initial liquid mass loadings, initial Stokes numbers, initial droplet temperatures and streamwise forcing amplitudes). The simulated results are then used in order to study: (i) mixing layer development and evaporative flow saturation, (ii) droplet organization and preferential concentration, and (iii) flow structure and modulation. The paper is organized as follows: The governing equations describing the gas phase transport, droplet transport, and phase coupling terms are presented in Section 2. This section also includes a new and thermodynamically self-consistent derivation of the evaporated vapor enthalpy, the latent heat of evaporation, and the gas phase internal energy. The mixing layer configuration and numerical approach are described in Section 3. Results relevant to evaporative flow saturation, preferential concentration and flow modulation are presented in Section 4. Conclusions and further discussions are provided in Section 5.

2 Mathematical Formulation

Consider the case of two-phase gas-liquid flows with evaporation of dispersed droplets into a pure inert carrier gas having different molecular weight and heat capacity than the evaporate. It is assumed that all species are calorically perfect, the dispersed phase volume fraction is much smaller than the gas phase volume fraction, and gravity is neglected. It is further assumed that constant values of the gas phase viscosity, thermal conductivity and species diffusivity can be prescribed independently of the local mixture fraction. The dispersed phase is assumed to be composed of spherical droplets with diameter significantly smaller than the Kolmogorov length scale; droplet

momentum transport is considered to be only a function of the drag force (i.e. gravity, Basset history, added mass and other terms are neglected); the droplet temperature is assumed to be internally uniform with infinite liquid conductivity; and thermal exchange with the gas phase is only through convective/conduction heat transfer (negligible radiation effects). Furthermore, nucleation, coalescence, breakup and collisions of droplets are all neglected. Throughout the formulation, the subscripts C , V and L will be used to distinguish quantities specific to the carrier gas, the evaporated vapor and the liquid, respectively; whereas the subscript G refers to the carrier plus vapor gas phase mixture.

2.1 Gas Phase Conservation Equations

The compressible form of the governing equations for the gas phase (carrier plus vapor mixture) are derived to include mass, momentum and energy exchange between the gas and the dispersed evaporating liquid phase:

$$\frac{\partial}{\partial t}(\rho_G) + \frac{\partial}{\partial x_j}[\rho_G u_j] = S_I, \quad (1)$$

$$\frac{\partial}{\partial t}(\rho_G u_i) + \frac{\partial}{\partial x_j}[\rho_G u_i u_j + P_G \delta_{ij} - \tau_{ij}] = S_{II,i}, \quad (2)$$

$$\frac{\partial}{\partial t}(\rho_G E_G) + \frac{\partial}{\partial x_j} \left[(\rho_G E_G + P_G) u_j - \lambda_G \frac{\partial T_G}{\partial x_j} - u_i \tau_{ij} \right] = S_{III}, \quad (3)$$

$$\frac{\partial}{\partial t}(\rho_G Y_V) + \frac{\partial}{\partial x_j} \left[\rho_G Y_V u_j - \rho_G \Gamma_G \frac{\partial Y_V}{\partial x_j} \right] = S_I, \quad (4)$$

$$\frac{\partial}{\partial t}(\rho_G \phi) + \frac{\partial}{\partial x_j} \left[\rho_G \phi u_j - \rho_G \Gamma_G \frac{\partial \phi}{\partial x_j} \right] = 0, \quad (5)$$

$$P_G = \rho_G \bar{R} \left[\frac{Y_V}{W_V} + \frac{(1 - Y_V)}{W_C} \right] T_G, \quad (6)$$

where ρ_G is the gas phase density, u_i is the gas phase velocity, $E_G = e_G + u_i u_i / 2$ is the total gas energy (internal e_G , plus kinetic), P_G is the thermodynamic pressure, Y_V is the mass fraction of the evaporated liquid vapor species, W denotes the molecular weight and ϕ is a passive scalar ‘tracer’ (used in this study to mark the single-phase stream of the mixing layer). Furthermore, τ_{ij} is the viscous stress tensor:

$$\tau_{ij} = \mu_G \left[\frac{\partial u_i}{\partial x_j} + \frac{\partial u_j}{\partial x_i} - \frac{2}{3} \frac{\partial u_k}{\partial x_k} \delta_{ij} \right], \quad (7)$$

where δ_{ij} is the Kronecker delta function, \bar{R} the universal gas constant, and μ_G , λ_G and Γ_G are the constant gas phase viscosity, thermal conductivity and Fickian diffusion coefficient, respectively. The right hand side (rhs) terms S_I , $S_{II,i}$ and S_{III} describe the phase couplings of mass, momentum and energy, respectively (discussed below). Note that a variable density (compressible) formulation is necessary even for low velocity flows due to the presence of both the mass source term and to non-equal molecular weight effects.

2.2 Individual Droplet Conservation Equations

The calculation of the phase coupling source terms in Eqs.(1)-(5) requires the specification of a model governing the behavior of a single droplet. It is impossible with present supercomputer capabilities to resolve all of the relevant droplet scales (internal and external boundary layers) for every single droplet; therefore, the term DNS as applied to the present flow only implies a complete resolution of the gas phase on scales equal to and larger than the Kolmogorov length (η_k) and time (τ_k) scales. Thus, the dispersed droplet phase can only be fully resolved on temporal scales, whereas the spatial droplet scales (which are assumed to be $\ll \eta_k$) must be modeled in an appropriate manner. Under the assumptions described above, a non-equilibrium Langmuir-Knudsen evaporation

model (Bellan & Harstad 1987[3]) is chosen based on a recommendation by Miller, Harstad & Bellan (1998)[35] after comparing eight different vaporization models applicable to DNS with a variety of experimental results. Here, the Lagrangian modeled equations describing the transient position (X_i), velocity (v_i), temperature (T_d) and mass (m_d) of a single droplet are:

$$\frac{dX_i}{dt} = v_i, \quad (8)$$

$$\frac{dv_i}{dt} = \frac{F_i}{m_d} = \frac{f_1}{\tau_d} (u_i - v_i), \quad (9)$$

$$\frac{dT_d}{dt} = \frac{Q + \dot{m}_d L_V}{m_d C_L} = \frac{Nu}{3 Pr_G} \left(\frac{C_{p,G}}{C_L} \right) \left(\frac{f_2}{\tau_d} \right) (T_G - T_d) + \left(\frac{\dot{m}_d}{m_d} \right) \frac{L_V}{C_L}, \quad (10)$$

$$\frac{dm_d}{dt} = \dot{m}_d = -\frac{Sh}{3 Sc_G} \left(\frac{m_d}{\tau_d} \right) \ln[1 + B_M], \quad (11)$$

where the subscript d denotes individual droplet conditions, the particle time constant for Stokes flow is $\tau_d = \rho_L D^2 / (18 \mu_G)$, D is the droplet diameter, C_L is the heat capacity of the liquid and the latent heat of evaporation is L_V . Additionally, the gas mixture heat capacity is calculated using a mass averaging; $C_{p,G} = (1 - Y_V) C_{p,C} + Y_V C_{p,V}$ (evaluated at the droplet location) where $C_{p,C}$ and $C_{p,V}$ are the constant pressure heat capacities of the carrier gas and vapor, respectively (note that $C_{v,C}$ and $C_{v,V}$ are the corresponding constant volume heat capacities). The gas phase Prandtl and Schmidt numbers are $Pr_G = \mu_G C_{p,G} / \lambda_G$ and $Sc_G = \mu_G / (\rho_G \Gamma_V)$, respectively. The drag force is determined by the local ‘slip velocity’ vector $u_{sl,i} = u_i - v_i$ (subscript sl denotes slip variables), whereas the convective thermal energy transfer [Q in Eq.(10)] is driven by the local ‘slip temperature’ ($T_{sl} = T_G - T_d$), and the evaporation rate [Eq.(11)] is driven by the local ‘slip vapor mass fraction’ ($Y_{V,sl} = Y_{V,s} - Y_V$) in terms of the mass transfer number; $B_M = (Y_{V,s} - Y_V) / (1 - Y_{V,s})$ (calculated using the non-equilibrium surface vapor fraction; subscript s denotes droplet surface conditions). Note that the gas phase variables u_i , T_G and Y_V correspond to the far field conditions for the droplets and must be interpolated from the Eulerian numerical grid to the droplet location during the simulations. The steady gravitational settling velocity ($v_{g,i} \approx \tau_d g_i$, where g_i is the gravitational acceleration vector) is much smaller than the characteristic flow velocity for all cases considered in this study; therefore, gravity effects are neglected in the droplet formulation.

In Eq.(9), Stokes drag is empirically corrected for finite droplet Reynolds numbers ($Re_{sl} = \rho_G U_{sl} D / \mu_G$ is based on the slip velocity and $Re_b = \rho_G U_b D / \mu_G$ is based on the blowing velocity) by the correlation:

$$f_1 = \frac{1 + 0.0545 Re_{sl} + 0.1 Re_{sl}^{1/2} (1 - 0.03 Re_{sl})}{1 + a |Re_b|^b}, \quad (12)$$

$$a = 0.09 + 0.077 \exp(-0.4 Re_{sl}), \quad b = 0.4 + 0.77 \exp(-0.04 Re_{sl}),$$

where $U_{sl} = |u_i - v_i|$ is the slip velocity magnitude, and the blowing velocity (U_b) is obtained from the mass conservation relation at the droplet surface: $\dot{m}_d = -\pi \rho_G D^2 U_b$. The correlation of Eq.(12) is fit to the axisymmetric simulation results of Cliffe & Lever (1985)[8] and is valid for the ranges $0 \leq Re_{sl} \leq 100$ and $0 \leq Re_b \leq 10$. The Nusselt (Nu) and Sherwood (Sh) numbers are empirically modified for convective corrections to heat and mass transfer based on the Ranz-Marshall correlations (Ranz & Marshall 1952a[39]; Ranz & Marshall 1952b[40]):

$$Nu = 2 + 0.552 Re_{sl}^{1/2} Pr_G^{1/3}, \quad Sh = 2 + 0.552 Re_{sl}^{1/2} Sc_G^{1/3}, \quad (13)$$

respectively. Finally, the function $f_2 = \beta / (e^\beta - 1)$ is an analytical evaporative heat transfer correction to the solid sphere Nusselt number which results from the quasi-steady gas phase assumption, where the non-dimensional evaporation parameter (β):

$$\beta = -\left(\frac{3 Pr_G \tau_d}{2} \right) \frac{\dot{m}_d}{m_d} = -\left(\frac{\rho_L Pr_G}{8 \mu_G} \right) \frac{dD^2}{dt}, \quad (14)$$

is constant for droplets obeying the ‘ D^2 law’ (Spalding 1953[46]; Godsave 1953[14]).

Non-equilibrium (subscript neq) effects are included in the droplet model using the Langmuir-Knudsen evaporation law as applied through the definition of the vapor molar fraction at the droplet surface ($\chi_{neq,s}$):

$$\chi_{neq,s} = \chi_{eq,s} - \left(\frac{2L_K}{D} \right) \beta, \quad (15)$$

where the equilibrium (subscript eq) contribution is given by the Clausius-Clapeyron relation:

$$\chi_{eq,s} = \frac{P_{atm}}{P_G} \exp \left\{ \frac{L_V}{(\bar{R}/W_V)} \left(\frac{1}{T_{B,L}} - \frac{1}{T_d} \right) \right\}, \quad (16)$$

P_{atm} is atmospheric pressure, $T_{B,L}$ is the liquid boiling temperature (hereinafter assumed to be constant and equal to the saturation temperature at pressure P_{atm}), and the molecular Knudsen layer thickness (L_K) is defined by:

$$L_K = \frac{\mu_G^T \sqrt{2\pi T_d (\bar{R}/W_V)}}{Sc_G P_G}, \quad (17)$$

where the accommodation coefficient has been assumed equal to unity. In the present work, the Knudsen layer thickness is defined using the true carrier gas viscosity (μ_G^T) rather than the scaled simulation viscosity (discussed below) in order to maintain physically meaningful length scales for the Knudsen layer. Finally, the vapor surface mass fraction is calculated directly from the molar fraction:

$$Y_{V,s} = \frac{\chi_{neq,s}}{\chi_{neq,s} + (1 - \chi_{neq,s})W_C/W_V}, \quad (18)$$

in terms of the ratio of the carrier gas and the vapor molecular weights.

The droplet conservation equations (9)-(11) suggest that the response time constant is approximately equal to τ_d for the droplet velocity and temperature, as well as for the relative evaporation rate \dot{m}_d/m_d which appears in the latent heat term of the droplet energy equation. Furthermore, note that although Eq.(11) is implicit in \dot{m}_d [through the term β in Eq.(15)], Miller, Harstad & Bellan (1998)[35] have shown that this equation can be solved without iteration by using the previous time step values for β because: (1) β is in general a slowly varying parameter, and is a constant for droplets obeying the ‘ D^2 law’, and (2) for both low evaporation rates and for droplet sizes $D > 50\mu m$ non-equilibrium contributions to the surface mole fraction are generally small. In this sense, the Langmuir-Knudsen model is no more computationally intensive than the commonly used Rapid Mixing Model (Spalding’s ‘ D^2 law’ coupled with an infinite liquid thermal conductivity droplet temperature equation) which is recovered by the present model as $\beta L_K/D \rightarrow 0$ [see Eq.(15)]; however, the present model is applicable over a wider range of droplet sizes and evaporation rates for which non-equilibrium effects become significant. Additionally, the modeled droplet energy equation [Eq.(10)] can also be applied to non-evaporating (solid) particles using the limit $f_2 \rightarrow 1$ as $\beta \rightarrow 0$.

2.3 Phase Coupling, Enthalpy, Internal Energy and Latent Heat

The choice of a Lagrangian reference frame for the individual droplet conservation equations leads to the following general form for the phase coupling terms appearing in Eqs.(1)-(5):

$$S_I = - \sum_{\alpha} \left\{ \frac{w_{\alpha}}{\Delta V_{\alpha}} [\dot{m}_d]_{\alpha} \right\}, \quad (19)$$

$$S_{II,i} = - \sum_{\alpha} \left\{ \frac{w_{\alpha}}{\Delta V_{\alpha}} [F_i + \dot{m}_d v_i]_{\alpha} \right\}, \quad (20)$$

$$S_{III} = - \sum_{\alpha} \left\{ \frac{w_{\alpha}}{\Delta V_{\alpha}} \left[v_i F_i + Q + \dot{m}_d \left\{ \frac{v_i v_i}{2} + h_{V,s} \right\} \right]_{\alpha} \right\}, \quad (21)$$

where the summations are over local individual droplet contributions, $h_{V,s}$ is the evaporated vapor enthalpy at the droplet surface (discussed below), and the single droplet evaporation rate (\dot{m}_d), drag force (F_i) and heat transfer rate (Q) are specified by the modeled droplet conservation equations (9)-(11). The local summations in Eqs.(19)-(21) are necessarily grid dependent functions; the summations are over all droplets (subscript α indicates the individual droplet variables; no summation over Greek indices) residing within a local numerical discretization volume (ΔV_α) and employ a geometrical weighting factor, w_α (discussed below).

In the above form, the phase coupling terms are in agreement with the derivations of Jackson & Davidson (1983)[18] and Young (1995)[54] for Eulerian dispersed phase flow descriptions, and also with those of Mashayek (1998a)[30]; Mashayek (1998b)[31] which were used to simulate the Lagrangian evolution of evaporating droplets in homogeneous turbulence. Note that neither of the first two citations addresses the evaluation of $h_{V,s}$, whereas Mashayek only considers flows for which the liquid and vapor heat capacities are equal and constant, in which case the correct evaluation of the vapor enthalpy is greatly simplified. In the discussions below, a more general derivation of the vapor surface enthalpy and related variables is presented.

Specification of the vapor enthalpy must be considered carefully in order to provide a thermodynamically self-consistent description of the surface enthalpy ($h_{V,s}$), the latent heat of evaporation (L_V) and the gas phase internal energy (e_G) [e_G is used to evaluate the local gas temperature]. Consider the enthalpy definitions for the carrier gas (h_C), liquid (h_L) and evaporated vapor (h_V) for thermally perfect species:

$$h_C = \int_0^T C_{p,C}(T') \cdot dT', \quad (22)$$

$$h_L = \int_0^T C_L(T') \cdot dT', \quad (23)$$

$$h_V = \int_0^T C_{p,V}(T') \cdot dT' + h_V^0. \quad (24)$$

The reference enthalpies for both the gas and liquid are taken to be zero at $T = 0$ (i.e. $h_C^0 = h_L^0 = 0$), whereas a non-zero reference value is required for the vapor (h_V^0) because the evaporated vapor and the liquid enthalpies cannot be defined independently of one another (being the same species). The definition of the latent heat, $L_V = h_{V,s} - h_{L,s}$ (for all droplet surface temperatures), provides the relationship between the liquid and vapor necessary to determine h_V^0 . Substituting Eqs.(23) and (24) into this definition yields:

$$h_V^0 = L_V(T^*) + \int_0^{T^*} [C_L(T') - C_{p,V}(T')] \cdot dT', \quad (25)$$

which must be a constant to be a meaningful reference condition. As expected, the Clapeyron relation:

$$\frac{\partial L_V}{\partial T} = -[C_L(T) - C_{p,V}(T)], \quad (26)$$

reveals that h_V^0 is indeed a constant (as a result of the integration constant), and is therefore independent of the evaluation temperature T^* . Physically, Eq.(25) states that h_V^0 is simply the latent heat evaluated at the reference temperature [here $h_V^0 = L_V(T = 0)$] and can be determined using standard correlations for L_V as a function of temperature (although only if the correlation is physically meaningful at the reference temperature). However, for more restrictive thermodynamic assumptions, such as constant heat capacities, the 'best' determination of h_V^0 is not so readily apparent.

In the present study all species are assumed to be calorically perfect and therefore have constant heat capacities. This assumption simplifies numerical calculations substantially by removing the necessity of integrating heat capacity correlations in order to determine enthalpies and internal energies. Under these conditions the definition of h_V^0 in Eq.(25) reduces to:

$$h_V^0 = L_V(T^*) + (C_L - C_{p,V}) T^*, \quad (27)$$

which again must be independent of the reference temperature T^* . The reference enthalpy is ‘best’ determined using correlations for the latent heat and constant heat capacities evaluated at a reference temperature T^* equal to the approximated average droplet temperature for the specific flow under consideration. Thereafter, the heat capacities and h_V^0 retain their constant values and L_V takes the linear form implicitly suggested by Eq.(27). With this procedure, the latent heat is ‘exact’ when the droplets are at temperature $T_d = T^*$ and deviates from the ‘real’ correlation for $T_d \neq T^*$ only in as much as the correlated L_V deviates from the linear approximation. One example of an appropriate T^* is the liquid wet bulb temperature (T_{WB}) as suggested by Miller, Harstad & Bellan (1998)[35] for constant property evaluations for use in single droplet evaporation models; they provide an empirical relation for estimating T_{WB} as a function of the free stream temperature for several hydrocarbon species and also provide all necessary property correlations for benzene, decane, heptane, hexane and water.

In view of the above discussions, expressions for the vapor surface enthalpy, the latent heat and the gas phase mixture internal energy are now specified for calorically perfect species as:

$$h_{V,s} = C_{p,V}T_d + h_V^0, \quad (28)$$

$$L_V = h_V^0 - (C_L - C_{p,V})T_d, \quad (29)$$

$$e_G = (1 - Y_V) [C_{v,C}T_G] + Y_V [C_{v,V}T_G + h_V^0], \quad (30)$$

respectively (the droplet surface temperature is $T_{d,s} = T_d$ due to the assumption of infinite liquid thermal conductivity). Note that an assumption of constant latent heat is only consistent with $C_L = C_{p,V}$ from Eq.(26): This approach, which was used by Mashayek (1998a)[30]; Mashayek (1998b)[31], removes the necessity of calculating the reference enthalpy [which reduces to $h_V^0 = L_V = \text{constant}$, by Eq.(27)] and therefore simplifies the specification of the gas temperature through Eq.(30). Furthermore, by utilizing the definitions of h_V^0 , L_V and Eqs.(9)-(11), the phase coupling terms given by Eqs.(19)-(21) may now be expressed equivalently as

$$S_I = - \sum_{\alpha} \left\{ \frac{w_{\alpha}}{\Delta V_{\alpha}} \left[\frac{d}{dt} (m_d) \right]_{\alpha} \right\}, \quad (31)$$

$$S_{II,i} = - \sum_{\alpha} \left\{ \frac{w_{\alpha}}{\Delta V_{\alpha}} \left[\frac{d}{dt} (m_d v_i) \right]_{\alpha} \right\}, \quad (32)$$

$$S_{III} = - \sum_{\alpha} \left\{ \frac{w_{\alpha}}{\Delta V_{\alpha}} \left[\frac{d}{dt} \left(m_d C_L T_d + \frac{1}{2} m_d v_i v_i \right) \right]_{\alpha} \right\}, \quad (33)$$

where the three time derivatives clearly depict the total rates of change of the individual droplet mass, momentum and total energy, respectively.

3 Mixing Layer Configuration and Approach

The flow configuration considered is that of a 3D, temporally developing, mixing layer formed by the merging of a pure gas stream with a hydrocarbon-droplet laden, parallel flowing stream. In the temporally developing reference frame the numerical domain moves with the mean convective velocity of the primary spanwise vortices which are therefore observed to grow in time, in contrast to spatial growth observed in experiments and spatially developing simulations (see e.g. Riley, Metcalfe & Orszag 1986[41] for a discussion of the temporally developing mixing layer simulation technique). Figure 1 shows a schematic of the simulation domain used in this study. In this coordinate system the free stream mean velocities are equal and opposite ($\pm U_0$), and the streamwise, cross stream and spanwise coordinate directions are denoted as x_1 , x_2 , x_3 (with corresponding domain lengths L_1 , L_2 , L_3), respectively. In this reference frame, boundary conditions are periodic in both the streamwise and spanwise directions, whereas we choose to use adiabatic slip wall conditions for the cross stream (x_2) boundaries (discussed below). The initially unladen stream ($x_2 > 0$) is a pure gas phase flow with parameters denoted by the subscript (US), whereas the initially laden stream ($x_2 < 0$; subscript LS) is initially randomly seeded

within homogeneous $x_1 - x_3$ planes with specified mean number density profile as a function of x_2 . The initial cross stream dependencies of the mean velocity, tracer scalar magnitude and droplet number density profiles are specified using an error function profile; $A(x_2) = A_{LS} + 0.5[1 + \text{erf}(\sqrt{\pi}x_2/\delta_{\omega,0})](A_{US} - A_{LS})$, where A is the specific field amplitude, $\delta_{\omega,0}$ is the specified initial value of the vorticity thickness (subscript 0 denotes initial conditions). The vorticity thickness is defined by $\delta_{\omega}(t) = \Delta U_0 / \langle \partial u_1 / \partial x_2 \rangle_{\text{max}}$, where $\Delta U_0 = 2U_0$ is the mean velocity difference across the layer and the brackets $\langle \rangle$ denote spatial averaging of Eulerian variables over homogeneous $x_1 - x_3$ planes.

Both 2D and 3D instabilities are excited through flow forcing using a procedure described in Moser & Rogers (1991)[37]. Spanwise and streamwise velocity disturbances are generated and then superimposed onto the initial mean error function velocity profile. In practice, the initial velocity perturbation is extracted from a more conveniently specified vorticity perturbation using an iterative Jacobi Poisson solver. Following Moser & Rogers (1991)[37], a fundamental spanwise vorticity disturbance is here first generated as $\omega_3(x_1, x_2) = -f(x_2) \sin(\pi x_1/\lambda_1)$, with wavelength $\lambda_1 = 7.29\delta_{\omega,0}$ and Gaussian cross stream distribution $f(x_2) = \exp(-\pi x_2^2/\delta_{\omega,0}^2)$. A single vortex pairing is obtained by superimposing an additional disturbance with wavelength equal to $2\lambda_1$ and having a relative amplitude of $0.5f(x_2)$. Three dimensionality is introduced by superimposing a secondary streamwise vorticity disturbance with distribution $\omega_1(x_2, x_3) = f(x_2) \cos\{2\pi x_3/(0.6\lambda_1)\}$. The relative amplitudes of the specified spanwise (F_{2D}) and streamwise (F_{3D}) perturbations are equal to the ratio of the respective disturbance circulations relative to the approximated circulation of the mean velocity profile ($\lambda_1 \Delta U_0$).

3.1 Numerical Procedure

The numerical solution procedure is based on a scheme derived by Kennedy & Carpenter (1994)[19] and uses an explicit fourth order accurate Runge-Kutta temporal integration (for both the gas phase and the Lagrangian droplet equations) coupled with eighth order accurate central finite difference approximations for all spatial derivatives (seventh order inward boundary closures for the x_2 coordinate). The numerical mesh is analytically compressed in the cross stream direction with maximum compression along the centerline. Both the streamwise and spanwise directions employ periodic boundary conditions, whereas the cross stream adiabatic slip wall conditions in the free streams ($x_2 = \pm L_2/2$) are implemented using the viscous compressible flow boundary method of Poinso & Lele (1992)[38]. In this procedure for slip conditions, the governing equations are solved in characteristic form on the x_2 boundaries whereby inwardly propagating waves are modeled as the negative of the corresponding outgoing wave decompositions (i.e. perfectly reflecting conditions). Slip walls are chosen for two primary reasons: (1) to remove the treatment of droplets entering and exiting the domain which must be addressed for free shear flow boundaries, and (2) the resulting ‘closed system’ simplifies the numerical confirmation of mass and energy conservation since a fixed quantity of mass and energy are tracked and the x_2 boundaries are adiabatic impermeable walls.

The Lagrangian droplet transport equations (8)-(11) require the knowledge of the gas phase flow variables evaluated at the local droplet position. In general, these locations will not coincide with grid point locations; therefore, a fourth order Lagrange procedure employed by Mashayek, Jaber, Miller & Givi (1997)[32] is modified for compressed grids and is used for the necessary interpolations. This interpolation procedure has been shown by Balachandar & Maxey (1989)[1] to compare well with a complete spectral interpolation. Furthermore, the droplet evaporation rate [Eq.(11)] is only iterated once, during initialization, for reasons described above. Thereafter, Eq.(11) is explicitly marched forward in time using the previous time step value for the non-dimensional evaporation parameter β appearing in Eq.(15).

Due to the mixed Eulerian/Lagrangian formulations for the gas/droplets, the local summations appearing in the rhs source terms in Eqs.(19)-(21) are necessarily grid dependent functions. In this case, the summation is over the geometrically weighted (w_{α}) contributions from all individual droplets (denoted by subscript α) residing within the discretization range $(i-1, i+1), (j-1, j+1), (k-1, k+1)$ centered around each numerical grid point with array indices (i, j, k) and $\Delta V_{\alpha} = (\Delta x_1 \Delta x_2 \Delta x_3)_{\alpha}$ is the computational grid volume at the location of droplet α . In practice, the contributions from each individual droplet are added to its eight nearest neighbor grid points

using a geometrical weighting based on the distance between the droplet and each of the surrounding nodes. The resulting source terms [Eqs.(19)-(21)] are then minimally smoothed using a local procedure whereby the source at each individual grid node is shifted towards the surrounding six nearest node average (with coefficient 0.75). This procedure is found to be necessary even for very small droplet mass loadings due to the spatial ‘spottiness’ of the source terms which can lead to artificial oscillations with large stencil finite differences (this occurs particularly near the $x_2 = -L_2/2$ boundary; see also Kennedy & Carpenter 1994[19] for a related discussion). Thorough testing performed during the course of the present work showed that the solutions are stabilized and well resolved using this smoothing procedure, and that the results are essentially independent of the smoothing coefficient. Additionally, the smoothing procedure is conservative so that the integrated transfer source terms are unaltered by the operation, in contrast to the high wavenumber energy truncation associated with pseudo-spectral simulations or with ‘filtering’ in large eddy simulations.

Specification of the time step for each simulation is based on consideration of both a maximum unity Courant number and on the particle time constant such that initially $\Delta t/\tau_{d,0} < 0.1$. Further consideration of Δt is related to the decreasing τ_d ’s (due to evaporation); when the droplet’s Stokes number, $St \equiv \tau_d \Delta U_0/\delta_{\omega,0}$, reaches 0.05 (equivalent to a 99% mass reduction for droplets with $St_0 = 1$) evaporation is stopped so as not to render Δt overly large. Therefore, the maximum relative time step is $\Delta t/\tau_d \approx 2$, which is the same value used by Martin & Meiburg (1994)[29] in studying solid particle dispersion in a 2D mixing layer. The Lagrangian droplet equations are therefore well resolved for all times, regardless of the decrease in τ_d due to evaporation. The governing equations for the ‘completely evaporated’ droplets are thereafter integrated with the evaporation artificially halted ($\dot{m}_d \equiv 0$), so that only droplet drag and convective heat transfer effects are included (note that the corresponding droplet mass is relatively small and no significant velocity slip or flow modulation is expected to be incurred by these droplets).

3.2 Flow Parameters and Properties

The majority of the available flow parameters and dimensions corresponding to the gas flow are held constant for all simulations in order to simplify the analysis of the results: The domain dimensions are chosen to be $L_1 = L_2/1.25 = L_3/0.6 = 0.2m$. The elongated cross stream domain size reduces boundary condition effects and provides adequate room for the mixing layer to grow, whereas the value $L_3/0.6$ corresponds to the most unstable spanwise disturbance wavelength for incompressible flow (see e.g. Moser & Rogers 1991[37]). The convective Mach number is chosen to be $M_c = U_0/a_0 = 0.5$ (the speed of sound, a , is initially uniform) in order to yield reasonable computational time steps while retaining the general behavior of low speed mixing layers. This choice is justified by the linear stability analysis performed by Sandham & Reynolds (1989)[44] which showed that compressible stability modes are not significant for $M_c < 0.6$, and also by the DNS performed by Samimy & Lele (1991)[43] of the dispersion of solid particles in a 2D planar mixing layer which found no significant compressibility effects on the dispersion process over the range $0.2 \leq M_c \leq 0.6$. The initial Reynolds number is $Re_\omega = \rho_{G,0} \Delta U_0 \delta_{\omega,0}/\mu_G = 200$, and the initial flow field is isobaric with $P_0 = P_{atm}$ and isothermal with $T_{G,0} = 350K$. The passive tracer is used to mark the initially laden and unladen stream fluids, and is initialized as $\phi = 0$ in the laden stream and $\phi = 1$ in the unladen stream (the tracer is only utilized in a limited manner in the following discussions in order to conditionally average variables on the laden stream gas flow; i.e. $\phi < 0.5$). As already discussed, the droplets are initially randomly distributed throughout $x_1 - x_3$ planes using the error function for the mean number density profile as a function of x_2 . The initial droplet slip velocity is null, the initial diameter (D_0) is based on a specified value for St_0 , and the constant initial droplet temperature is $T_{d,0} = 325K$ unless otherwise noted. The above set of parameters are chosen in order to yield evaporation time scales approximately equal to the mixing layer growth time scale; the limiting behavior of very slow (or rapid) evaporation rate is similar to solid particle (or single-phase) flow, and is therefore not of interest in the present study. Furthermore, the grid resolution is in all cases chosen to be $96 \times 128 \times 64$ grid points in the x_1, x_2, x_3 directions, respectively, and is compressed in x_2 with $\Delta x_2/\Delta x_1|_{\min} \approx 0.6$ at $x_2 = 0$. The normalized forcing amplitudes are $F_{2D} = 0.10$ and $F_{3D} = 0.0175$ (unless otherwise noted) which are found to provide relatively

strong 2D and 3D rollup and vortex pairing (see Moser & Rogers 1991[37] for a discussion of the effects of the forcing amplitudes in single-phase flow).

The two species chosen for consideration in this study are: (1) air for the carrier gas, and (2) decane for the liquid/vapor hydrocarbon (chosen for its large molecular weight and latent heat). Only relatively small evaporation rates are studied as quantified by the gas temperature relative to the liquid boiling temperature. In this case, the deviations between the initial droplet temperature, wet bulb temperature and gas temperature are relatively small and it is considered appropriate to use $T^* = T_{G,0}$ as an appropriate reference condition for property evaluations. Therefore, all heat capacities, the gas Prandtl number, the ‘true’ air viscosity and vapor reference enthalpy are all evaluated at $T^* = 350K$ from correlations found in Miller, Harstad & Bellan (1998)[35], and the Lewis number (Le_G) is assumed to be unity (i.e. $Sc_G = Pr_G$). However, in order to provide a full resolution of the flow, the gas phase viscosity is defined using an artificially inflated value calculated from a specified Reynolds number, Re_w . In this sense, the species are essentially ‘pseudo-air’ and ‘pseudo-decane’; however, effects due to realistic air-hydrocarbon molecular weight ratios, heat capacity ratios and latent heat magnitude are retained. The constant property values used in the simulations are provided in Table 1. Simple evaluations show that the thermal response time for these properties is somewhat larger than the corresponding velocity and evaporation (\dot{m}_d/m_d) response times because $f_2 Nu/(3 Pr_G) C_{p,G}/C_L \approx 0.4$ in Eq.(10) for small Re_{sl} and Re_b , whereas $f_1 \approx 1$ in Eq.(9) and $Sh/(3 Sc_G) \approx 0.96$ in Eq.(11) under the same conditions.

Property	Value
W_C	$28.97 \text{ kg}(\text{kg} \cdot \text{mole})^{-1}$
W_V	$142.0 \text{ kg}(\text{kg} \cdot \text{mole})^{-1}$
$C_{p,C}$	$1004.8 \text{ J.kg}^{-1}\text{K}^{-1}$
$C_{p,V}$	$1939.6 \text{ J.kg}^{-1}\text{K}^{-1}$
C_L	$2520.5 \text{ J.kg}^{-1}\text{K}^{-1}$
Pr_G	0.697
μ_G^T	$2.094 \times 10^{-5} \text{ kg m}^{-1}\text{s}^{-1}$
ρ_L	642 kg m^{-3}
$T_{B,L}$	447.7 K
h_V^0	$5.35 \times 10^5 \text{ J.K}^{-1}$

Table 1: Property values used in the simulations (evaluated at $T^* = 350K$ and atmospheric pressure from correlations for air and decane found in Miller, Harstad & Bellan 1998[35]). The subscripts C and V denote the carrier gas and evaporated vapor, respectively.

4 Results

Table 2 presents the parameters of the simulations which were performed for this study. The two primary parameters describing the simulations are the liquid mass loading ratio $ML = Nm_{d,0}/(\rho_{G,0}L_1L_2L_3/2)$, defined as the total mass of liquid relative to the total mass of gas in the laden stream at time $t = 0$ (N is the total number of droplets), and the initial droplet Stokes number $St_0 = \tau_{d,0}\Delta U_0/\delta_{w,0}$. The results of simulations Run 0-Run 7 elucidate the effects of these parameters over the ranges $0 \leq ML \leq 0.35$ (with fixed $St_0 = 1.02$) and $0.50 \leq St_0 \leq 2.00$ (with fixed $ML = 0.125$). The effects of the streamwise forcing amplitude and initial droplet temperature are explained by comparing results from simulations Run 8 and Run 9 to those of Run 4, while simulations Run 10 and Run 11 correspond to ‘solid particle’ dispersion with and without convective thermal energy exchange between phases. We denote as ‘solid particles’ droplets having the evaporation rate artificially nulled ($\dot{m}_d \equiv 0$) in order to isolate drag force and convective droplet thermal energy exchange effects.

The range of parameters in Table 2 is entirely consistent with the model assumptions. For example, the maximal initial volume fraction of droplets in the laden stream is 5.5×10^{-4} (for Run 5) which is sufficiently

Run	ML	St_0	N	Note
0	0	-	0	-
1	0.02	1.02	40,000	-
2	0.075	1.02	150,000	-
3	0.125	1.02	250,000	-
4	0.225	1.02	450,000	-
5	0.35	1.02	700,000	-
6	0.125	0.50	728,863	-
7	0.125	2.00	91,295	-
8	0.225	1.02	450,000	$F_{3D} = 0.00175$
9	0.225	1.02	450,000	$T_{d,0} = 350K$
10	0.225	1.02	450,000	$T_{d,0} = 350K; \dot{m}_d \equiv 0$
11	0.225	1.02	450,000	$T_{d,0} = 350K; \dot{m}_d \equiv Q \equiv 0^\dagger$

Table 2: Simulation parameters. All runs have $96 \times 128 \times 64$ grid points with $M_c = 0.5$, $Re_\omega = 200$, $T_{G,0} = 350K$ and $T_{d,0} = 325K$ (except as noted). Initial droplet sizes are $D_0 = 115.5\mu m$, $165\mu m$ and $231\mu m$ for $St_0 = 0.50$, 1.02 and 2.00 , respectively, and the dagger (\dagger) indicates that $Q \equiv 0$ applies only to the phase coupling in Eq.(21) and not to the droplet energy equation (10).

small to satisfy the assumptions of the flow model. Also, extensive testing showed that the single-phase mixing layer is well resolved for a substantially higher Reynolds number ($Re_\omega \approx 275$) than is used for the simulations. The above parameters were chosen in order to ensure that all simulations are fully resolved, and *a posteriori* testing confirmed that this is true. Furthermore, conservation of total mass and total energy (internal plus kinetic for both phases) for the closed system mixing layer was monitored and confirmed for all simulations (except for Run 11 which does not conserve energy due to $Q \equiv 0$ in the Eq.(21) coupling terms; although the total relative loss is very small).

All simulations were performed on a Cray J90 supercomputer. The majority of the computational expenditure occurs in simulating the droplet phase; in particular, in interpolating the six gas phase variables (u_i , T_G , P_G , Y_V) to the droplet locations, and also in calculating the phase coupling source terms. The run times range from approximately 4.7 hours of CPU time for the pure gas flow (Run 0), to approximately 27 CPU hours for Run 5 with 7.29×10^5 droplets.

In presenting the simulation results, we first describe the general evolution of the mixing layer and the process of evaporative flow saturation (Section 4.1). This is followed by a detailed analysis of the instantaneous state of the droplet distribution and its relationship to vortical structures within the layer (Section 4.2). These physical descriptions then aid in interpreting the statistical flow analysis presented in Section 4.3. The discussions focus primarily on the effects of droplet loading and the initial Stokes number, with only occasional comments regarding solid particle and other results as they become relevant (Run 8-Run 11). In order to keep the presentation as concise as possible, the majority of statistical analyses will be presented for instantaneous results from the fully developed mixing layers (at the final simulation times); however, temporal evolutions of statistical quantities will also be discussed but only in a more limited extent, as necessary.

4.1 Mixing Layer Growth and Evaporative Saturation

An examination of the temporal evolution of integral flow statistics provides insight into the development of the two-phase mixing layer and the influences of the various droplet parameters. Figure 2 shows the growth of the layer as characterized by the normalized vorticity thickness evolution for various values of both the mass loading ratio and the initial Stokes number. A substantial and increasing attenuation of the mixing layer growth is observed in Fig.2a during the latter stages of mixing for increasing droplet loadings (at fixed $St_0 = 1.02$). Flow

visualizations of our results reveal that the initial spanwise vortex rollup is completed at a normalized time of $t\Delta U_0/\delta_{\omega,0} \approx 25$. Prior to this time there does not appear to be any significant influence from the droplets on the layer growth rate; an analysis of the generated data reveals that this is primarily due to the fact that the droplets are initialized with zero slip velocity, and hence zero drag force. It is only after the primary rollers fully develop and begin the pairing event ($t\Delta U_0/\delta_{\omega,0} > 25$) that the flow field becomes sufficiently ‘turbulent’ to result in significant velocity slip, and therefore droplet drag acting on the fluid. Although substantial phase exchanges of mass and thermal energy occur prior to the first vortex rollup ($t\Delta U_0/\delta_{\omega,0} < 25$), it will become apparent that these exchanges primarily affect the thermodynamic development of the layer, whereas the kinematic flow attenuation is primarily governed by the drag force. Figure 2b suggests that there is essentially no influence of the initial droplet Stokes number (for fixed mass loading $ML = 0.125$) on the large scale development of the layer as characterized by the vorticity thickness (explained below). The oscillations in the vorticity thickness occurring during the pairing process are created by both vortical rollup and pressure reflections from walls and occur at approximately the same time, and with similar phase and amplitude, for all curves. When considered together with flow visualizations (not shown), this suggests that it is the rate of mixing layer growth, and not the relative vortex rollup and pairing times, that are modulated by the liquid phase (i.e. at any given time, all of the simulations are at the same relative point of roller development, but have different thickness); even simulation Run 5, having the largest mass loading $ML = 0.35$, displays discernible (though retarded) rollup and pairing events. In all cases, the pairing event is completed by $t\Delta U_0/\delta_{\omega,0} \approx 50$ at which point the simulations are terminated.

The flow modulation discussed above appears to be entirely due to effects of mass loading, with negligible effects from the initial droplet size (Fig.2b). This can be explained by considering the momentum coupling term [analogous to Eq.(20)] due to Stokes drag which results from stochastic Eulerian dispersed phase descriptions (e.g. Zhou 1993[55]):

$$S_{II,i} = -nF_i'' = -n \left(m_d \frac{dv_i}{dt} \right)'' \sim -\hat{\rho}_L \left(\frac{u_{sl,i}}{\tau_d} \right)'' , \quad (34)$$

where n is the Eulerian droplet number density, the superscript double-prime denotes ‘average’ Eulerian variables characterizing local ensembles of droplets, and $\hat{\rho}_L = nm_d''$ is the Eulerian dispersed phase mass density (liquid mass per total mixture volume). Equation (34) shows that the total drag force exerted on the gas phase scales directly with $\hat{\rho}_L$, and therefore also with ML in the simulations. However, the scaling with droplet size (for fixed $\hat{\rho}_L$ or ML) is not obvious as the droplet time constant (τ_d) and the slip velocity ($u_{sl,i} = u_i - v_i$) are both expected to be increasing functions of the droplet size. In fact, for steady gravitational drift at low droplet slip Reynolds numbers, $u_{sl,i}/\tau_d = g_i$; i.e. the ratio of the slip velocity relative to the droplet time constant is independent of the droplet size for uniform accelerations. This argument can be extended to time dependent accelerations [i.e. $g \rightarrow g(t)$] if the characteristic time scale for $g(t)$ is significantly larger than the droplet response time (τ_d). For the present flow, the time scale $\delta_{\omega,0}/\Delta U_0$ characterizes the acceleration field acting on the droplets; this means that $u_{sl,i}/\tau_d$ is approximately constant for Stokes numbers sufficiently smaller than unity. Since St decreases from initial values due to evaporation (quantified below), the total drag force should also be relatively independent of the droplet size for fixed liquid mass loading (as observed in Fig.2b). Of course, the relatively simple analysis using Eq.(34) neglects non-linear f_1 corrections due to finite droplet Reynolds numbers which may change the scaling for sufficiently large slip velocity. Effects due to variations of the Stokes number may therefore occur if a sufficiently large St_0 values are considered. Nevertheless, the results of Fig.2 clearly reveal that the mass loading ratio has the dominant effect on the mixing layer evolution, and that variations in the droplet size over the range $0.5 \leq St_0 \leq 2.0$ have a negligible influence on the flow modulation. These results support previous trends suggested by Squires & Eaton (1990)[47] from DNS of stationary isotropic turbulence laden with solid particles. Their tabulated data show relatively negligible effects of the particle size on the integrated turbulence energy for cases with $St = 0.15$ and $St = 0.52$ (for fixed particle loadings in the range $0.1 \leq ML \leq 1.0$). In contrast, Elghobashi & Truesdell (1993)[13] reported variations in turbulence energy and dissipation as a function of the Stokes number in their DNS study of solid particle dispersion in two-way coupled isotropic turbulence when fixing the total number of particles instead of ML ; the present results indicate that this is not an appropriate

manner for studying Stokes number effects.

The normalized total mass of liquid in the mixing layer domain ($M_L = \sum^N m_d$) and the corresponding normalized total mass of evaporated vapor $[(M_{L,0} - M_L)/M_C]$; the total mass of carrier gas is M_C and is a constant for all simulations and all times] are depicted in Fig.3 as a function of time for the same simulations presented in Fig.2. These results show that the only simulation which achieves complete evaporation of the liquid droplets is Run 1, characterized by the smallest mass loading $ML = 0.02$. All other simulations appear to approach a state of quasi-steady evaporative saturation for which a zero rate of liquid loss is asymptotically approached; furthermore, the total mass of liquid at the saturation stage is nearly independent of the initial loading ratio (discussed below). The Stokes number effects observed for early times in Figs.3c and 3d (although the same final saturation state is apparently approached by all curves) are attributed to the fact that small droplet size distributions lose mass at a faster rate relative to larger droplets with fixed total liquid mass. Indeed, if the superscripts a and b denote two different monodisperse size classes for droplets evaporating according to the ‘ D^2 law’ (i.e. with $dD^2/dt = K$, where K is constant), it can be shown that at fixed ML :

$$\frac{N^{(a)} \dot{m}_d^{(a)}}{N^{(b)} \dot{m}_d^{(b)}} = \left(\frac{D^{(b)}}{D^{(a)}} \right)^2. \quad (35)$$

Thus, if $D^{(b)} > D^{(a)}$, then the total liquid evaporation rate integrated over all droplets is larger for the small droplets with diameter $D^{(a)}$. As should be expected, the relative ratio of the total mass loss rates is a function of the droplet surface areas available for evaporation. These arguments explain the early time deviations between the various curves in Figs. 3c and 3d due to the initially smaller Stokes numbers evaporating total liquid mass more rapidly. Nevertheless, the asymptotic total mass of liquid evaporated is nearly independent of St_0 .

4.1.1 Effects of Initial Droplet Temperature and Flow Three-Dimensionality

An examination of the evolutions of the mean droplet temperature (averaged over all droplets) and the normalized total liquid mass are presented in Fig.4 for simulations Run 4 and Run 9 which have $T_{d,0} = 325K$ and $T_{d,0} = 350K$, respectively ($ML = 0.225$, $St_0 = 1.02$). The mixing layer is non-homogeneous and Fig.4 therefore does not carry any information as to the cross stream variations of the droplet temperatures and sizes; however, these figures are useful in explaining the saturation process. Evaporation commences immediately, even when the slip temperature is initially null because the slip vapor fraction is non-zero. Thereafter, the latent heat acts to drive the droplet temperature towards the quasi-steady wet bulb temperature as observed in Fig.4a (for a given fuel the wet bulb temperature is predominantly a function of the local gas temperature and not the droplet size; see e.g. Miller, Harstad & Bellan 1998[35]). The flow then continues to develop in a manner similar to that already observed in the previous figures (the small temperature oscillation in Fig.4a at intermediate times coincides with the conclusion of the primary spanwise vortical rollup). The mean temperatures in Fig.4a adjust from their initial values relatively rapidly, on a time scale approximately equal to $\tau_{d,0}$, consistent with Eq.(10). In a related issue, these results indicate that for initial conditions using arbitrary initial droplet velocities, the slip velocity will also be equilibrated on the same time scale (τ_d) as the droplet temperature [see Eq.(9)]; this was confirmed using an additional simulation (with $v_{i,0} = 2u_{i,0}$) not reported in this paper. Finally, the liquid mass evolutions in Fig.4b suggest that saturation occurs for both flows with slightly more evaporated mass for larger initial droplet temperatures.

As an additional observation, we note that the weak F_{3D} forcing used in Run 8 shows some expected change in the development of the vorticity thickness due to the weaker integrated initial velocity disturbance and very weak streamwise vortices; however, the overall effect on saturation is not qualitatively significant (not shown). The above discussions therefore illustrate that while the influence of the initial droplet temperature and flow three dimensionality have quantitative effects on the final state of the flow, the qualitative droplet evolutions are not significantly affected by these parameters. The remaining discussions therefore focus primarily on the effects of ML and St_0 ; with the influences of F_{3D} and $T_{d,0}$ understood to be qualitatively similar.

4.1.2 Mean Slip Variable Profiles

The physical mechanisms responsible for the evaporative saturation observed in the previous figures can be explained in terms of the two primary slip variables driving the individual droplet evaporation rates [note that the slip velocity also contributes to the evaporation rate through the Nusselt and Sherwood numbers; however, in the present simulations the droplet Reynolds numbers are generally $Re_{sl} \sim 1$ (not shown) and therefore effects due to U_{sl} should be of second order]. An examination of the droplet temperature and mass transport equations [Eqs.(10) and (11)] shows that the evaporation rate is: (1) related directly to the slip vapor fraction, and (2) related (indirectly) to the slip temperature through the droplet energy equation. Therefore, in order to saturate the flow and cease the liquid evaporation, these slip variables must be nulled by either changing the droplet surface conditions and/or by modulating the flow in an appropriate manner (see also Bellan & Cuffel 1983[2] on criteria for saturation).

In order to aid in the analysis of the slip variables and other forthcoming statistical analyses, we introduce two averaging operators. Hereinafter, the single bracket notation $\langle \rangle$ is used to denote averages of Eulerian (gas phase) variables over grid points, whereas the double bracket notation $\langle\langle \rangle\rangle$ denotes averaging of Lagrangian (droplet) variables over the ensemble number of droplets. These statistics quantities are generally presented as a function of x_2 with the averages being performed over homogeneous $x_1 - x_3$ planes, and therefore conditionally on the cross stream coordinate location. This is achieved for Eulerian variables using the ensemble of grid points defining each homogeneous computational plane, whereas Lagrangian droplet statistics are calculated by averaging over the number of droplets located within each of 25 equal interval bins dividing the x_2 length of the domain.

Figure 5 illustrates $\langle Y_V \rangle$ and $\langle\langle Y_{V,s} \rangle\rangle$ and thus provides insight into the first order statistical behavior of the slip vapor fraction as a function of the cross stream coordinate at the final simulation time $t\Delta U_0/\delta_{\omega,0} = 50$. The profiles in Fig.5a show that the vapor fraction in the laden stream approaches a nearly uniform value which is independent of the initial mass loading ratio for cases in which saturation occurs ($0.075 \leq ML \leq 0.35$). This uniform mass fraction is approximately equal to the corresponding mean surface fraction ($Y_{V,s}$) for droplets in the laden stream (Fig.5b) indicating that the mean evaporation has essentially ceased. However, within the layer the slip vapor fractions are relatively large indicating that droplets which are entrained into the layer continue to evaporate. At the final simulation time shown in the figure, both the gas phase vapor and the droplets penetrate approximately one vorticity thickness into the pure gas stream for all cases studied. The increase in gas phase vapor fractions with ML at the center of the layer (Fig.5a) is directly related to the available liquid mass in the non-saturated regions. An analysis of the simulated results suggests that a continual entrainment of droplets caused by the growth of the layer is the primary reason that the total liquid evolutions in Fig.3 do not reach exactly steady values. The absence of a curve for case $ML = 0.02$ in Fig.5b is due to the droplets having reached the minimum size corresponding to $St = 0.05$ and being treated as solid particles at this time.

The mean temperature profiles presented in Fig.6 show that it is not only the build up of vapor in the gas phase which is responsible for saturation. At time $t = 0$ the droplets (at $T_{d,0} = 325K$) are exposed instantaneously to the relatively higher temperature isothermal flow at $T_{G,0} = 350K$. The droplets are then quickly heated to a quasi-steady wet bulb temperature as was shown previously in Fig.4 with the thermal equilibration occurring on a time scale approximately equal to τ_d [see Eq.(10)]. Therefore, for $St < 1$ the droplet temperature is able to adjust to the surrounding flow conditions relatively rapidly. Simultaneously, the phase coupling terms act to reduce the gas temperature in the laden stream through convective heat exchange. Figure 6a shows the final time mean gas temperature profiles which clearly reveal the decrease in T_G both within the layer and in the laden stream ($x_2 < 0$). All of the evaporating simulations reach an approximately equal thermodynamic state in the laden stream, except for $ML = 0.02$ which completes evaporation before this state is obtained. The droplets and gas in the laden stream therefore appear to be driven towards an equilibrium at a temperature of approximately $330K$, which is primarily a function of the liquid properties (e.g. L_V , C_L) and not ML . On the other hand, the mean droplet temperature profiles (Fig.6b) appear qualitatively similar to those of the surrounding gas phase with the exception of case $ML = 0.02$ which displays a large peak at the $x_2 = 0$ centerplane in addition to a minor peak at $x_2/\delta_\omega \approx 0.8$. In this case, the droplets are completely evaporated at the final time (Fig.3a) and are in approximate

thermal equilibrium with the surrounding gas due to small thermal inertia; therefore, $\langle T_d \rangle \neq \langle T_G \rangle$ from Fig.6a because the droplets are preferentially concentrated into streak structures (to be shown) and only a biased sample of locations are represented in the averaging of Fig.6b.

The mean slip temperature calculated at the droplet locations, quantified in Fig.6c, shows nearly zero mean slip temperature in the laden stream, but mean positive slip temperatures within the layer. The mean slip temperature of the $ML = 0.02$ simulation droplets (solid particles at this time) is insignificant for all cross stream locations [although local regions of persistent slip temperature do exist (see below) for solid particles within the layer, these effects become negligible through averaging]. The curve for case $ML = 0.075$ crosses the remaining curves within the layer for $x_2 > 0$ (see Fig.6c) which can be attributed to the fact that a significant percentage ($\approx 10\%$) of droplets are completely evaporated at the final simulation time. Additional analyses of the results presented in Figs.5 and 6 show that they are essentially unchanged by variations in the initial Stokes number (not shown) due to the relative independence of the wet bulb temperature on the droplet size. Finally, the above results indicate that the saturation process observed within the laden stream portion of the domain is qualitatively the same as that observed in homogeneous turbulence by Mashayek (1998a)[30] and Mashayek (1998b)[31]; however, the continued evaporation of droplets penetrating the layer is a unique feature of the non-homogeneous mixing layer.

It is interesting to note that a relatively simple algebraic relationship between the slip temperature and the slip vapor fraction can be derived for droplets with Stokes number sufficiently smaller than unity. In this case, since the droplet temperature time constant is approximately equal to τ_d by Eq.(10), the droplet temperature adjusts to changes in the surroundings more rapidly than the characteristic flow time scale ($\delta_{w,0}/\Delta U_0$). This results in a quasi-steady balance between convective heating and latent heat effects in the droplet energy equation, which can therefore be combined with the mass evaporation rate equation [Eq.(11)] to yield:

$$\left(\frac{L_V}{C_{p,G}} \right) \ln[1 + B_M] = T_{sl}, \quad (36)$$

where the Lewis number has been assumed equal to unity and the droplet slip Reynolds number has been assumed to be small (valid for $St \ll 1$). Furthermore, noting that the logarithmic term can be expanded for small B_M (small evaporation rates) leads to the following relationship:

$$Y_{V,sl} \approx \left(\frac{C_{p,G}}{L_V} \right) T_{sl}, \quad (37)$$

where the denominator in the mass transfer number ($1 - Y_{V,s}$) has been assumed to be approximately equal to unity [this assumption is employed in the ‘mass-analogy’ class of evaporation models (Miller, Harstad & Bellan 1998[35]) used in past studies by Crowe, Sharma & Stock 1977[9]; Mashayek 1998a[30]; Mashayek 1998b[31], and explains why these models are strictly valid only for small evaporation rates]. Equation (37) predicts a nearly linear relationship between the slip temperature and slip vapor fraction under the assumptions of $Le_G = 1$, $St \ll 1$ and $B_M \ll 1$. For the present flow conditions, the droplet Stokes numbers are all less than unity during the latter stages of mixing due to evaporation, and the calculated transfer numbers are typically $\sim 10^{-2}$. Evaluating the latent heat at $T_{G,0} = 350K$ (note that $\langle L_V \rangle$ varies by less than 3% across the layer) and taking $C_{p,G} = C_{p,C}$ suggests that the data presented in Figs.5 and 6 are related by $Y_{sl} \approx T_{V,sl}/330$. Our evaluations indicate that Eq.(37) holds approximately for the DNS results (not shown).

4.1.3 Droplet Mass Profiles and PDF

One consequence of the saturation process is that a quasi-steady distribution of droplet sizes is formed within the layer. Figure 7 reveals the mean form of this distribution by presenting the average droplet mass across the layer as a function of both the mass loading and the initial droplet Stokes number at the final simulation time. An essentially uniform mean droplet size is found within the laden stream portion of the domain for all simulations. Droplets penetrating into the layer are in contact with higher temperature gas flow and therefore display a mean size distribution that decreases with penetration depth. The differences in droplet mass observed in Fig.7b for

varying initial Stokes numbers can be attributed to the fact that the larger Stokes number simulation has not completely reached the asymptotic saturation state; this was explained previously as being due to slower total evaporation rates resulting from less total surface area available for evaporation for large droplet size distributions [see Fig.3d, Eq.(35) and related discussions]. Note also that the above droplet mass results do not indicate the relative number density of droplets across the layer. In fact, the mean number density profiles (deferred until Fig.16) show a somewhat similar form with near uniform values in the laden stream and with decreasing concentration as a function of penetration depth into the layer.

The complete droplet size distributions corresponding to cases with $ML = 0.125$ and $ML = 0.35$ (with $St_0 = 1.02$) are illustrated by the probability density function (PDF) of the normalized droplet mass as a function of the cross stream coordinate in Fig.8 (not joint PDFs). The PDF's are calculated by summing the local droplet contributions to each of 25 equal interval bins dividing both the droplet mass and the x_2 coordinate. In both cases, an approximate Gaussian droplet mass distribution is found in the laden stream. Mashayek, Jaber, Miller & Givi (1997)[32] also observed near Gaussian droplet diameter PDF's from DNS of one-way coupled isotropic turbulence with evaporating droplets obeying the ' D^2 law.' For two-way coupled DNS of isotropic turbulence laden with evaporating droplets, Mashayek (1998a)[30] found that the droplet diameter PDFs approach a Gaussian for $ML \leq 0.25$, but become highly skewed for larger mass loadings; these findings are consistent with the present results in the laden stream portion of the domain. On the other hand, the interior of the layer is characterized by a wide range of droplet sizes which decreases in the mean with penetration depth. The slight bulge in the PDF in Fig.8a at $x_2/\delta_\omega \approx +0.5$ and $m_d \approx 0$ is due to droplets that have achieved complete evaporation; however, Fig.8b shows that no droplets have reached this state for the $ML = 0.35$ simulation. These PDF's seem to present essential features of the two-way mass interactions; in fact, the vapor mass fraction (Y_V) PDF's in the gas phase are similar to those observed in Fig.8 (see Miller & Bellan 1998[34] for related results from simulation Run 4). Additional examinations of droplet mass PDF's reveal that the total range of droplet sizes present within the mixing layer (i.e. the polydispersity) at the final simulation times increases with both increasing ML and St_0 .

4.2 Droplet Organization and Preferential Concentration

Before proceeding with a more detailed statistical analysis of the two-phase mixing layer, it is helpful to first elucidate the instantaneous structure of the dispersed droplet field. Such an analysis aids in understanding the cross stream averaged properties presented thus far, which reveal no information on the actual droplet distributions within $x_1 - x_3$ planes. The following discussions therefore include both flow visualization and quantitative graphical results corresponding to instantaneous mixing layer flow fields; they are meant to explain the local distribution and behavior of droplets relative to the large scale flow structures. Such information not only helps in the interpretation of the statistical results, but may also be of importance to the future development of turbulence models and structural dynamical descriptions of two-phase evaporating droplets flows.

4.2.1 Flow Visualizations

4.2.1.1 Number Density Distribution

Figure 9 presents contours of the droplet number density for three different planes within the instantaneous mixing layer results generated in Run 4 ($ML = 0.225$, $St_0 = 1.02$). The contours are presented at the final simulation time ($t\Delta U_0/\delta_{\omega,0} = 50$), after the completion of the spanwise vortex pairing. The number density is calculated as an Eulerian field from the instantaneous Lagrangian droplet locations:

$$n = \sum_{\alpha} \frac{w_{\alpha}}{\Delta V_{\alpha}}, \quad (38)$$

where the summation and the geometric weighting factor (w_{α}) were described previously in Section 3.1. Inverse shading is used in the figure which highlights larger droplet concentrations with darker shading. The maximum local number density found in the results of Fig.9 corresponds to a value approximately seven times the initial mean number density in the laden stream. The number density contours give no indication as to the liquid mass

because they do not contain information on the actual droplet sizes, which are decreasing in the mean with the penetration depth (see Figs.7 and 8).

The number density contours presented in Fig.9a are for a spanwise symmetry plane located between the primary streamwise vortices at $x_3 = 0$, and therefore represent the optimal results for comparisons with both previous 2D particle dispersion simulations and unforced experiments. The most obvious feature of this figure is that the primary spanwise vortical region (at $x_1/\delta_\omega \approx 2$) formed by the pairing event is essentially devoid of droplets, whereas a ‘streak’ formation of enhanced concentration occurs having a maximum in the strained braid region and wrapping around the outer periphery of the vortical structure (on the laden stream edge). Similar concentration streaks have been observed previously for solid particles with $\tau_d \sim 1$ by Wen, Kamalu, Chung & Crowe (1992)[51]; Longmire & Eaton (1992)[28] (for a jet); Martin & Meiburg 1994[29]; Kiger & Lasheras (1997)[22]). For evaporating droplets, this streak brings droplets into close contact with the higher temperature unladen stream fluid in the braid region, thereby enhancing evaporation rates (the gas temperature gradients are largest across the braids; not shown). As with solid particles, these droplet configurations are explained by the droplets being centrifuged away from vortical fluid due to inertia (particularly at earlier times before substantial evaporation occurs; $St \sim 1$) and congregating in high strain ‘convergence’ regions of the flow; this is the preferential concentration phenomena described in Section 1 (e.g. Eaton & Fessler 1994[11] for a review). However, we do not find that droplets are laterally dispersed farther into the unladen stream than fluid particles as described previously by Chein & Chung (1987)[7], Lazaro & Lasheras (1992b)[26] and Martin & Meiburg (1994)[29] for solid particles with $St \sim 1$, because the Stokes numbers for evaporating droplets become $\ll 1$ by the time that they fully cross to the unladen stream side of the layer (Figs.7 and 8). These droplets are therefore small enough to closely follow fluid motions and have insufficient inertia to exhibit enhanced lateral dispersion. Moreover, the homogenizing influence of the vortex pairing previously observed by Kiger & Lasheras (1995)[21] and Kiger & Lasheras (1997)[22] is here somewhat counteracted by evaporation which drives the droplet size towards a non-homogeneous, monotonically decreasing (with penetration depth) size distribution (Figs.7 and 8).

The number density contours corresponding to a spanwise plane bisecting one of the streamwise vortices (at $x_3/\delta_\omega = 1.2$) are illustrated in Fig. 9b. In this case, the presence of the streamwise vortical structure dramatically changes the appearance of the number density field. The droplets are now centrifuged away from both the central spanwise and the elongated streamwise vortical regions. The high concentration streak formations are now located in the highly strained fluid surrounding the streamwise vortices. This is further illustrated in Fig.9c which shows the number density contours in a streamwise plane within the braid region at $x_1 = 0$. The four counter rotating streamwise vortices draw the laden stream fluid containing droplets upwards and into the unladen stream, while conversely drawing unladen fluid downwards into the laden stream. This results in the formation of concentration ‘mushroom’ structures similar to passive scalar formations found previously for single phase mixing layers in both experiments (Bernal & Roshko 1986[4]) and in direct simulations (Metcalf, Orszag, Brachet, Menon & Riley 1987[33]; Miller, Madnia & Givi 1994[36]). These results reveal that concentration streaks continue to persist for strongly 3D flow; however, the streaks are highly convoluted in the third dimension. Thus, for 3D mixing layers, streaks form in strained fluid regions between spanwise rollers, and are simultaneously wrapped around the periphery of streamwise vortices resulting in the formation of secondary concentration mushroom structures. The implication of the number density contours and the small Stokes numbers (indicating that the droplets approximately follow the local fluid motions which also convect the vapor) is that the vapor mass fraction contours have similar mushroom structures and regions of enhanced vapor ‘streaks’ because the vapor is produced by the droplets (not shown).

4.2.1.2 Slip Velocity Distribution

Kiger & Lasheras (1997)[22] presented results from particle dispersion in an experimental mixing layer revealing the existence of persistent regions of positive and negative slip velocity related to accelerating and decelerating fluid regions, respectively. The distribution of these regions determines the corresponding distribution of kinetic energy exchange between phases due to the drag force (e.g. Kiger & Lasheras 1997[22]). Figure 10 presents

contours of the Eulerian slip velocity field, where the Eulerian representation of any arbitrary droplet variable Ψ is denoted by a superscript double-prime and is defined as:

$$\Psi'' = \frac{1}{n} \sum_{\alpha} \frac{w_{\alpha}}{\Delta V_{\alpha}} \Psi_{\alpha}, \quad \Psi'' \equiv 0 \text{ if } n = 0, \quad (39)$$

which is an average over local droplets; in Fig.10 $\Psi = u_{sl} = |u_i| - |v_i|$ is the slip velocity magnitude. The Eulerian variable u_{sl}'' can be used to identify regions of the flow within which turbulence energy is ‘generally’ dissipated by the droplet drag force ($u_{sl}'' > 0$) as well as the regions where the droplet drag ‘generally’ enhances the kinetic energy of the flow ($u_{sl}'' < 0$). The three planes in Fig.10 correspond to the same data presented in Fig.9, and the contours are labeled in units of m/s . Note that the ‘spottiness’ of these fields is related to the intermittent distribution of droplets, and not to resolution problems. As before, the spanwise plane between streamwise rollers ($x_3 = 0$) provides for the best comparisons with the approximately 2D mixing layer experiments of Kiger & Lasheras (1997)[22]. As the fluid is accelerated around the primary spanwise roller in Fig.10a (the flow is from right to left for the laden stream), inertia reduces the acceleration rate of droplets relative to that of the flow. This results in a region of persistent positive slip velocity below, and on the leading edge of, the roller (region I; Fig.10a). As the fluid then enters the braid region and is decelerated, inertia causes the droplets to retain momentum resulting in negative slip velocity (region II; Fig.10a). Similarly, region III flow is experiencing acceleration, whereas two more deceleration regions are identified: regions IV and V in Fig.10a. These observations are in excellent qualitative agreement with similar persistent slip regions indicated by Kiger & Lasheras (1997)[22] who plotted experimentally measured slip velocity vectors (see e.g. Figs.5 and 6 of the citation); however, their results do not make a clear distinction between regions II and V identified in Fig.10a.

Figures 10b and 10c show the effects of flow three-dimensionality on the mean local slip velocities for planes corresponding to those described in Fig.9. For the spanwise plane bisecting the secondary roller (Fig.10b), both the accelerating and decelerating flow regions below the primary spanwise vortex are clearly identifiable (regions I and II). However, within the initially unladen stream portion of the layer all slip velocities are observed to be positive for both the core and braid regions of the flow. This is indicative of the fluid being accelerated around the edges of the streamwise vortices (i.e. x_3 motion). Although the primary vortical structures exhibit some flow deceleration, the vortical cores are essentially devoid of droplets (see Fig.9b) and therefore Fig.10b displays no significant negative slip velocity in the vortical fluid analogous to region IV in Fig.10a. Figure 10c helps to explain these observations using slip velocity contours in a streamwise plane at $x_1 = 0$. The region denoted I contains accelerating fluid and therefore positive slip velocity which is wrapped around the periphery of streamwise vortices. The decelerating region II fluid corresponds to braid deceleration fluid analogous to region V depicted in Fig.10a. Finally, as the laden stream fluid is drawn upwards into the concentration mushrooms, its x_2 motion is decelerated in the cores of the mushrooms, resulting in secondary regions of persistent negative slip velocity (region III; within both mushrooms).

4.2.1.3 Slip Temperature Distribution

The above observations lead to the obvious question of whether or not the temperature field exhibits similar persistent slip regions corresponding to the distribution of thermal energy exchange between the phases. Since, to the author’s knowledge, this point has never been addressed, it is useful to first examine the behavior of solid particles representing a baseline behavior. Figure 11 shows the spanwise $x_3 = 0$ plane contours of the locally averaged Eulerian slip temperature, T_{sl}'' , calculated from the instantaneous droplet field from Run 10 ($ML = 0.225$, $St = 1.02$) using the procedure defined by Eq.(39). These contours can be compared directly to those of Fig.10a (although the instantaneous flows are not identical, their qualitative features are the same). Since there is no evaporation, and since the slip temperatures are everywhere equal to zero at $t = 0$, the mean gas and droplet temperatures are both approximately uniform across the layer and equal to $T_{G,0}$ (not shown). The regions denoted I-V in Fig.11 are observed to be completely analogous, but inversely related, to regions I-V for the slip velocity presented in Fig.10a. In Run10, as the fluid is accelerated around the spanwise structure, it is

entering a lower flow temperature area associated with the low pressure spanwise vortex core (it is not obvious that this occurs when density variations are present; however, flow visualizations of our results confirm it to be true, even in the presence of evaporation); therefore thermal inertia causes a temperature lag for droplets and the slip temperature in region I is negative. Similar arguments can be made for the remaining regions II-V, explaining the results by either the relatively high temperature braided fluid or by the relatively low temperature vortical fluid. The reason that the slip velocity and slip temperature are so closely correlated is in part due to the fact that the droplet's velocity and thermal response time constants are both approximately equal to τ_d [see Eqs.(10) and (11)]. Similarly, we found that the slip temperature for solid particles in the spanwise ($x_3/L_3 = 0.4$) and streamwise ($x_1 = 0$) planes also parallels that of the slip velocity presented in Figs.10b and 10c (not shown).

Figure 12 reveals a markedly different behavior of the slip temperature distribution for evaporating droplets: due to the laden stream fluid temperature being substantially reduced by latent heat effects (see Fig.6), all droplets penetrating across the $x_2 = 0$ centerplane of the layer experience positive slip temperatures in all three planes (region IV in Fig.12a; region III in Fig.12b; region II in Fig.12c). The spanwise plane in Fig.12a ($x_3 = 0$) between secondary vortices does exhibit a small region (III) of negative slip temperature due to the low pressure vortex core acting to maintain a slight reduction in fluid temperature; however very few droplets are found in the vortex core (i.e. n is small). Inside of the laden stream portion of the domain, the slip temperature is essentially the same as for solid particles (i.e. inversely related to the slip velocity) because the laden stream flow is quasi-saturated and the latent heat effects are relatively weak. The concentration mushrooms (Fig.12c) enhance evaporation by drawing droplets with low slip temperatures up and into the high temperature unladen stream fluid (region I). A parallel study of contours of the slip vapor mass fraction ($Y_{V,sl} = Y_{V,s} - Y_V$) is moot because our results show that there are no discernible regions of condensation within the flow; thus, the slip mass fraction is positive definite throughout the domain (not shown).

4.2.2 Conditional Averaging on the Second Invariant

Squires & Eaton (1990)[47] showed that the preferential concentration of solid particles in isotropic turbulence can be quantified by conditionally averaging the number density on the second invariant of the fluid deformation tensor. Their results indicate that particles tend to be centrifuged away from high vorticity regions and collect in high strain regions of the turbulence. The second invariant (II_u) of the tensor field $u_{i,j} = \partial u_i / \partial x_j$ can be written in terms of the symmetric [$s_{ij} = (u_{i,j} + u_{j,i})/2$] and anti-symmetric [$\Omega_{ij} = (u_{i,j} - u_{j,i})/2$] tensor decompositions as:

$$II_u = -\frac{1}{2} \frac{\partial u_i}{\partial x_j} \frac{\partial u_j}{\partial x_i} = -\frac{1}{2} (s_{ij} + \Omega_{ij}) (s_{ji} + \Omega_{ji}) = -\frac{1}{2} (s_{ij}s_{ji} + \Omega_{ij}\Omega_{ji}) = -\frac{1}{2} \left(S^2 - \frac{1}{4} \omega_i \omega_i \right), \quad (40)$$

where S^2 is the squared strain magnitude and $\omega_i \omega_i$ is the squared vorticity magnitude (enstrophy). In this form, Eq.(40) clearly reveals that strong positive second invariant values are composed of predominantly rotational fluid, whereas strong negative values delineate regions where strain dominates. Squires & Eaton (1990)[47] considered Stokes number in the range $0.075 \leq St \leq 1.50$, and showed that particles with small (but finite) Stokes numbers display the strongest preferential concentration effects. This was elucidated through the presentation of conditional averages of the number density, conditioned on II_u (i.e. $\langle n | II_u \rangle$), which showed increased concentrations in high strain regions (i.e. $II_u < 0$).

4.2.2.1 Conditional Number Density and Droplet Mass

Figure 13 presents the number density field conditionally averaged on both the second invariant of the deformation tensor and on passive scalar tracer values $\phi < 0.5$ (i.e. considering primarily only laden stream fluid) at the final simulation times for various values of both the mass loading ($St_0 = 1.02$) and the initial Stokes number ($ML = 0.125$). The number density is in all cases normalized by its initial mean value in the laden stream; $n_0 = N/(L_1 L_2 L_3/2)$. For the present mixing layer configuration, the second invariant quantitatively separates the three primary regions of the flow: (1) vortical structures (both spanwise and streamwise) for $II_u > 0$, (2) high strain regions predominantly located in the braids for $II_u < 0$, and (3) free stream fluid outside of the layer for

$II_u \approx 0$. The curves in Fig.13a indicate that increasing the mass loading ratio results in an increasing tendency for droplets to be concentrated in high strain regions of the flow. These curves provide quantitative evidence of the previously observed concentration streak formations. At the smallest loading $ML = 0.02$ the vortical regions are essentially devoid of droplets, whereas strained regions show a nearly uniform droplet concentration. This is due to the droplets having sufficient inertia to be centrifuged away from vortical structures during the early stages of mixing before substantial evaporation occurs; since evaporation is completed for the $ML = 0.02$ droplets at $t\Delta U_0/\delta_{\omega,0} \approx 40$ (see Fig.3a), thereafter they behave as fluid elements. Once in the strain regions these droplets show no further tendency to concentrate (although there is no mechanism to return them to vorticity regions). Saturation occurs for the remaining cases resulting in larger mean droplet size distributions as a function of the initial loading ratio (Fig.7a); therefore, the heavier droplets corresponding to larger mass loadings show the strongest preferential concentration effects in Fig.13a due to their larger inertia (the crossing of the $ML = 0.35$ and $ML = 0.225$ curves at the negative II_u extrema is due to sample size). This same argument explains the stronger concentrations in $II_u < 0$ regions observed for large St_0 droplets in Fig.13b. Our findings are opposite to those reported by Squires & Eaton (1990)[47] for isotropic turbulence: they suggest decreasing preferential concentration for increasing solid particle Stokes number. However, if this occurred in mixing layers, it would be inconsistent with many experimental and simulation results which reveal that particle streaks are optimally formed for $St \sim 1$ (Wen, Kamalu, Chung & Crowe (1992)[51]; Martin & Meiburg 1994[29]; Kiger & Lasheras (1995)[21]; Kiger & Lasheras (1997)[22]). We conjecture that the large scale mixing layer structures are responsible for this discrepancy because they are primarily responsible for the droplet centrifugation. For example, Lazaro & Lasheras (1992a)[25]; Lazaro & Lasheras (1992b)[26] only observed enhanced lateral particle dispersion for forced mixing layers, and not for unforced cases. This possibility cannot be addressed by the present DNS because the Reynolds numbers are too small to perform physically meaningful unforced simulations.

In addition to the number density, the structural distribution of the droplet mass for evaporating flows can also be illustrated through conditional averaging on the second invariant. These results are presented in Fig.14 for the same simulations as in Fig.13; however, the averaging is over Lagrangian droplet quantities and II_u has been interpolated to the droplet locations. At the final simulation time, the averages in Fig.14a show that the droplet mass is highly dependent on the location within the flow field. The largest droplet masses are in all cases found in the laden stream fluid outside of the layer. For all flow regions, the mean droplet mass is an increasing function of the mass loading ratio due to the saturation process (see Figs.7 and 8). Inside the strained flow regions ($II_u < 0$) the mean droplet mass is observed to decrease with increasing strain, because strained braid structures are associated with relatively large local temperature. Moreover, droplets within the strain region ($II_u < 0$) are generally larger than those in vortical regions ($II_u > 0$) despite the fact that low pressure vortices are generally at a lower temperature than the strained braid regions. This occurs for two primary reasons: (1) The number density is reduced within vortices (Fig.13) and therefore so is the vapor mass fraction; this allows for increased droplet mass loss prior to saturation. (2) It is only the smaller droplets that are able to closely follow fluid motions and resist centrifugal expulsion from the vortices. Finally, as discussed previously, larger initial Stokes numbers result in larger droplets within the layer at saturation (see Fig7b), thus accounting for the effects of St_0 observed in Fig.14b.

4.2.2.2 Conditional Slip Temperature

The structural distribution of the slip temperature field is addressed in Fig.15 for both solid particles and evaporating droplets. The results from simulations with solid particles depicted in Fig.15a correspond to flows for which thermal coupling with the gas phase is either considered ($Q \neq 0$ in S_{III}) or is not considered ($Q = 0$ in S_{III}), although the droplet energy equation is solved in both cases. In both of these simulations, the droplets in vortical regions ($II_u > 0$) tend to be at temperatures greater than the surrounding fluid temperature, whereas droplets in strained regions ($II_u < 0$) are on average at a lower temperature than the fluid (see also Fig.11). As will be discussed below, thermal coupling with the condensed phase acts to reduce fluctuations in the gas temperature; therefore, the thermally uncoupled case illustrated in Fig. 15a shows a larger variance in the gas phase

temperature field, which explains the differences between the two slip temperature curves. For cases involving evaporation, an entirely different behavior of the conditionally averaged slip temperature is found (Fig.15b; see also Fig.12): droplets in both the vortical and strained regions are being mixed with relatively high temperature unladen stream fluid. This results in enhanced evaporation rates and positive mean slip temperatures due to latent heat effects for all cases except the completely evaporated $ML = 0.02$ droplets (see also Figs.6c and 12). An inverse dependence of the conditional slip temperature magnitude as a function of ML is found for droplets residing within the vortical and strained fluid regions. These observations can be explained after noting that the ‘wet bulb depression’ (i.e. $T_G - T_{WB}$) is an increasing function of the local gas temperature (e.g. Miller, Harstad & Bellan 1998[35]). The droplets corresponding to larger mass loading ratios are characterized at the final simulation times by larger total liquid mass (Fig.3a) in addition to larger individual droplet mass and therefore also larger thermal inertia (Fig.7a). Therefore, large mass loadings are more efficient at dampening the gas phase temperature (this is discussed in more detail below) and result in the decreased slip temperatures found in Fig.15b for strained flow regions ($II_u < 0$). A plausible explanation for why the opposite trends are found in the vortical regions ($II_u > 0$) is based on the previous observation that preferential concentration effects are simultaneously being enhanced with increasing ML (Fig.13a): Since fewer droplets reside within the vortices, the gas phase temperature is less dampened by the droplets, and therefore the slip temperature increases with ML .

4.3 Statistical Profiles and Flow Modulation

Attention is now turned to describing the nature of the two-phase mixing layer as illustrated by the cross stream profiles of pertinent mean and fluctuating statistical quantities. In particular, we are interested in determining the extent of similarity which may (or may not) exist for the mixing layer, as well as the structure and modulation of both first and second order statistics. Furthermore, the effects of the initial droplet Stokes number (within the range $0.5 \leq St_0 \leq 2.0$) have already been observed to be essentially negligible and will hereinafter be discussed only as necessary.

4.3.1 First Order Statistics

The mean Eulerian droplet number density cross stream profiles are shown as a function of both the initial mass loading and the initial droplet Stokes number at the final simulation times in Fig.16. The two most prominent aspects of these curves are the approximate coincidence (or ‘collapse’) with variation of ML and the occurrence of an overshoot at the inner edge of the layer. The coincidence of the curves is attributed to a similar coincidence of the mean streamwise velocity (discussed below) which convect the droplets. The enhanced number density magnitudes on the inner edge of the layer ($x_2/\delta_w \approx -1$), which in all cases exceed the laden stream number density, has been found previously for solid particle laden mixing layer simulations (Martin & Meiburg 1994[29]) as well as for both unforced and forced experiments (Lazaro & Lasheras 1992a[25]; Lazaro & Lasheras 1992b[26]). In particular, Martin & Meiburg (1994)[29] studied a wide range of droplet Stokes numbers ($10^{-2} \leq St \leq 10^2$) and observed this peak in the concentration profiles for all Stokes numbers larger than $St \sim 10^{-1}$; the peaks were attributed to the lateral dispersion of the concentration streaks (see Fig.9) into the laden stream fluid. Martin & Meiburg also found a second complementary peak in the number density profiles on the unladen stream side of the layer in many cases; this does not occur in the present simulations because the Stokes numbers for droplets penetrating into/through the layer are substantially reduced by evaporation such that these droplets behave as fluid elements. Note also that Lazaro & Lasheras (1989)[24]; Kiger & Lasheras (1995)[21] both report similar peaks in Sauter mean diameter profiles (for polydisperse solid particles) and attribute them to a preferential lateral dispersion of heavy particles. Our results do not show any corresponding peaks in the droplet size profiles (see Fig.7) which is again due to evaporation reducing the size of droplets penetrating the layer (note that our solid particle simulations Run 10 and Run 11 are monodisperse, so we cannot compare these results to the experiments). Furthermore, two additional minor peak regions are found in both Figs.16a and 16b at $x_2/\delta_w \approx -0.5$ and $x_2/\delta_w \approx +0.5$ which are also due to the distribution of the droplets with respect to the vortical and strain regions (Fig.9). In particular, these secondary peaks in the mean number density profiles are enhanced (or retarded at $x_2/\delta_w \approx +0.5$) as preferential

concentration is enhanced; i.e. for both increasing ML (Fig.13a) and for increasing St_0 (Fig.13b). This effect is most obvious in Fig.16b because the turbulence energy is relatively unaffected by changes in St_0 , whereas increased mass loadings reduce the gas phase vortical development (to be shown) which counteracts somewhat the preferential concentration process.

The cross stream variations of the mean gas and droplet velocities are presented in Fig.17 at the final simulation time for various values of the liquid loading ratio; the mean free stream u_1 velocity is slightly larger in magnitude than the initialization U_0 due to the superimposed forcing disturbance and the impermeable wall x_2 boundaries (i.e. the flow must increase its velocity near the walls to compensate for the expansion of the layer). The most obvious feature of these curves is that the mean gas velocity profiles (Fig.17a) coincide for all liquid loadings when the x_2 coordinate is normalized with the instantaneous vorticity thickness (note that δ_ω is a function of ML ; see Fig.2). This is somewhat unexpected since both the mixing layer growth rate and the cross stream variation of the mean gas temperature (Fig.6a) have already been shown to be strongly modulated by droplet loading. However, this finding is not unprecedented: Kulick, Fessler & Eaton (1994)[23] also observed that the normalized mean velocity profile for turbulent channel flow is unaltered for solid particle mass loadings as large as 80%. Similarly to our results, the mean channel flow profiles coincided despite the fact that the turbulence energy was strongly attenuated by the particles. At the present time we have no completely satisfying explanation for either the present or the channel flow results. This issue therefore deserves future scrutiny.

Further consideration of Figs.17a and 17b shows that the mean streamwise droplet velocities are smaller than the corresponding fluid velocity for all mass loadings and cross stream locations. This indicates that the droplets are actually moving faster on average than the gas within the laden stream portion of the layer where the velocities are negative (note that this does not require the droplet velocities to be *locally* larger than the fluid velocity because $\langle u_1 \rangle$ is not calculated at the droplet locations). This somewhat unexpected result occurs for all of the simulations and can be attributed to the fact that droplets tend to concentrate into decelerating fluid regions within this portion of the domain, as seen by identifying negative slip velocity regions in Fig.10 and comparing them to corresponding concentrations in Fig.9. The mean streamwise droplet velocity exhibits a small reduction with increased liquid mass loadings due to saturation at larger droplet inertia for large ML (Fig.7a). For incompressible flow, the mean cross stream gas velocity $\langle u_2 \rangle$ must be zero due to divergence free velocity and the homogeneity of the x_1 and x_3 coordinate directions. For the present slightly compressible flow, Fig.17c shows that dilatational effects result in a small finite $\langle u_2 \rangle$ profile in the absence of evaporation ($ML = 0$) which is indicative of symmetric layer expansion away from the $x_2 = 0$ plane. As will be shown below, evaporation causes a reduction in the laden stream pressure which acts to draw fluid towards the $x_2 < 0$ portion of the domain for $ML > 0$ and results in slightly negative $\langle u_2 \rangle$ values across the entire layer (Fig.17c). On the other hand, the droplets are initialized non-symmetrically about the $x_2 = 0$ plane and therefore display a significant mean velocity ($\langle \langle v_2 \rangle \rangle$) corresponding to penetration into and across the layer (Fig.17d); i.e. droplets crossing the layer are not statistically offset by reverse motions because only the $x_2 < 0$ portion of the domain is seeded (see e.g. Fig.9). Therefore, even the $ML = 0.02$ droplets, which closely follow fluid motions due to their very small Stokes numbers (completely evaporated), are characterized by positive cross stream motion within the layer. On the laden stream side of the layer $\langle \langle v_2 \rangle \rangle$ is negative corresponding to a decrease in the laden stream pressure which is an indirect result of evaporation for the present mixing layer (explained below). It is only the $ML = 0.02$ droplets that do not display this negative peak near $x_2/\delta_\omega \approx -1$ due to the relatively low mass loading and correspondingly small pressure and/or dilatational effects. These results suggest that the dispersed phase mean velocity profiles do not coincide under the coordinate scaling: this is in agreement with the channel flow measurements of Kulick, Fessler & Eaton (1994)[23].

Figure 18 displays the cross stream variations of the normalized mean gas phase pressure and density at the final simulation times for various initial droplet mass loading ratios. In contrast to the mean streamwise gas velocity, these profiles do not coincide under the coordinate scaling. The pressure profiles display a minimum point within the layer at $x_2 = 0$ for all cases, which is due to the presence of the low pressure vortex cores. Evaporation causes an increase in the gas density in the laden stream which intuitively may be expected to result

a corresponding *increase* in the laden stream pressure. However, the simultaneous decrease in the laden stream temperature (Fig.6a) due to latent heat effects counteracts this expected effect resulting in a net decrease in the laden stream pressure as observed in Fig.18a. An examination of the pressure profiles near the $x_2 = -L_2/2$ wall reveals a dissimilarity between the various curves which results from interaction of the layer expansion with the wall: The $ML = 0.35$ layer is relatively thin (Fig.2a) and interacts only minimally with the wall showing a small pressure bulge on the edge of the layer; however, as the mass loading is reduced and the layer becomes wider, the corresponding pressure bulges on the layer's edge come in contact with the wall. On the unladen stream portion of the domain the mean pressure is also found to decrease with increasing ML even though there are no droplets present for $x_2/\delta_\omega > 1$; this reduction results from both the mean pressure imbalance and the mean gas temperature gradient (Fig.6a) across the layer, resulting in the correspondingly larger net fluid motion towards the laden stream with increasing ML (Fig.17c). The mean density profiles in Fig.18b follow directly from the state equation and the already explained physical processes associated with the gas temperature (Fig.6a), the vapor mass fraction (Fig.5a) and the gas pressure (Fig.18a). As expected, the laden stream density is increased by evaporation through mass addition to the gas phase. In the center of the layer, the density is found to increase with ML despite the fact that essentially the same total mass of liquid has been evaporated for the cases with $ML > 0.075$ (Fig.3b); this is due to the combined effects of the density along the $x_2 = -L_2/2$ wall being modified by the above mentioned wall-pressure interaction, and to the requirement that the integral $\int < \rho_G > dx_2$ must be approximately constant for cases with $ML > 0.075$ due to approximately the same evaporative gas phase mass additions (see Fig.3b). Finally, note that the non-coinciding density profiles reveal that the mean streamwise momentum profiles, in contrast to the streamwise velocity profiles in Fig.17a, do not coincide.

4.3.2 Second Order Statistics

We now turn our attention to the cross stream profiles of second order statistical quantities, with particular emphasis on the modulation and possible profile coincidence of statistics related to small scale flow features. The root mean square (rms) statistics are calculated as:

$$\Psi_{G,rms} = \sqrt{(\langle \Psi_G'^2 \rangle)}, \quad \Psi_{d,rms} = \sqrt{(\langle \Psi_d'^2 \rangle)}, \quad (41)$$

where Ψ_G and Ψ_d are arbitrary gas phase (Eulerian) and droplet (Lagrangian) variables, respectively. Hereinafter, the rms notation will be understood to be defined with the appropriate averaging shown here for either Eulerian or Lagrangian droplet variables. Rms statistics of the Eulerian number density are highly sensitive to the grid spacing due to the appearance of the computational volume in Eq.(38): For example, consider a 1D (x) domain with uniformly distributed droplets spaced at equal intervals Δs . If the grid spacing is $\Delta x = \Delta s$ with the droplets placed exactly at the grid nodes, then the number density is $n = \langle n \rangle = 1/\Delta s$ at all grid points; the rms number density is therefore equal to zero everywhere as it should be for the uniform distribution. On the other hand, if an increased resolution is used with $\Delta x^* = \Delta x/2 = \Delta s/2$, then the local number density alternates between values of $n = 2/\Delta s$ and $n = 0$ at alternating grid points, and the rms is $n_{rms} = 1/\Delta s$ (although the mean remains correct with $\langle n \rangle = 1/\Delta s$). These relations are extended to the general 3D case in Table 3 which shows that $\langle n \rangle$ is correctly calculated independent of the grid for all cases; however, n_{rms} is only grid independent when the grid spacing is larger than the droplet spacing (which is not generally the case, even for very large numbers of droplets, due to preferential concentration). The symbol \cong used in the table indicates that the values can vary slightly depending on the weighting factor (w) and the relative alignment of the grid relative to the droplets. This grid dependency is related to the necessity of assuming that many droplets are contained within averaging volumes when deriving Eulerian-Eulerian two-phase flow models (e.g. Zhou 1993[55]; Elghobashi 1994[12]). In light of these discussions we will not present second order statistics of the Eulerian number density in this paper; however, statistics of Lagrangian droplet variables are not grid dependent and will be presented below.

Figure 19 presents profiles of the rms fluctuations of both the gas and droplet phase velocities at the final simulation times and for various droplet loadings. Several important features are displayed by the rms velocity profiles. First, none of the fluctuating quantities has coinciding profiles under the coordinate scaling, in contrast

$\zeta \geq 1$	$\zeta < 1$
$n \cong \zeta/(\Delta s)^3$ or 0	$n \cong 1/(\Delta s)^3$
$\langle n \rangle \cong 1/(\Delta s)^3$	$\langle n \rangle \cong 1/(\Delta s)^3$
$n_{rms} \cong (\zeta - 1)^{1/2}/(\Delta s)^3$	$n_{rms} \cong 0$

Table 3: Derived grid dependency of uniformly spaced (Δs) droplets calculated from Eq.(38) on a uniformly spaced (Δx) computational grid as a function of the relative volumes,
 $\zeta = (\Delta s)^3/(\Delta x)^3$.

to the mean number density and the mean streamwise gas velocity which do coincide (Figs.16 and 17a) for varying ML . Second, the turbulence energy becomes increasingly attenuated with increasing mass loadings; this effect is most strongly apparent in the cross stream component ($u_{2,rms}$) due to the droplets impeding the large scale vortical rollup. In no cases do we find increased total gas phase kinetic energy as has been found in several past experiments involving large solid particles (see e.g. Kenning & Crowe 1997[20]); however, these kinetic energy increases were generally attributed to either droplet wake or gravitational effects and occurred only for large droplets having $D/l > 10^{-1}$ where l is the integral length scale of the turbulence (e.g. Elghobashi & Truesdell 1993[13]). Third, the streamwise component energy is slightly increased by the droplets at the centerline (Fig.19a); this is due to the influence of negative slip velocities in regions of decelerating gas flow within the high concentration braids structures (Fig.10a) which serve as a source of gas phase kinetic energy. The trends observed for the droplet velocity fluctuations as a function of ML are readily explained in terms of the larger inertia for the larger ML cases at the time of saturation. The secondary ‘bulge’ in the $v_{1,rms}$ profiles at the inner edge of the layer (Fig.19b) forms because of the lateral dispersion of the concentration streaks which are being drawn around the primary spanwise roller (Fig.10a). However, as the liquid loading is increased the formation of streaks and spanwise rollers is impeded, and the secondary peak fades. The effects of the initial droplet Stokes number are essentially negligible for second order gas velocity component modulation (not shown).

A comparison of the respective gas and droplet profiles in Fig.19 shows that both the streamwise and spanwise droplet velocity component energies are larger than the corresponding gas phase intensities within the unladen stream portion of the profiles ($x_2 > 0$), in contrast to the cross stream component for which $u_{2,rms} > v_{2,rms}$ for all x_2 . Elevated streamwise component intensities for a dispersed phase have previously been observed in turbulent channel flow by Kulick, Fessler & Eaton (1994)[23], detected in turbulent boundary layer flow by Rogers & Eaton (1990)[42], and found in homogeneous shear turbulence by Mashayek (1998b)[31] (for evaporating droplets), as well as in other turbulent flows containing a mean velocity gradient (Soo, Ihrig & El Kouh 1960[45]; Carlson & Peskin 1975[6]; Tsuji & Morikawa 1982[50]; Steimke & Dukler 1983[49]). This phenomena has also been predicted theoretically for the streamwise velocity components in the presence of a constant mean gas velocity gradient by Liljegren (1993)[27] for solid particles. However, to our knowledge this has never been identified for the spanwise component as is observed by comparing Figs.19e and 19f. The reason for this is two-fold: First, none of the above experiments or simulations have treated flows with strong large scale three-dimensionality. Second, the concentration of droplets/particles must be non-symmetric about the $x_2 = 0$ plane to create this effect. In the present mixing layer, droplets that are ‘flung’ into the unladen stream by spanwise motions (v_3) due to the secondary vortices experience a decelerating u_3 field because the streamwise vortices are strongest near the middle of the layer. Therefore, inertia effects cause the slip velocity component $u_3 - v_3$ to be negative. However, since there are no droplets in the unladen stream penetrating the layer in the opposite direction, there is no statistical offset from inverse droplet motions: The net effect is that $v_{3,rms} > u_{3,rms}$ for $x_2 > 0$.

The final time cross stream profiles of the rms gas and droplet temperatures are shown in Fig.20 as functions of both the initial droplet loading and the initial Stokes number. The presence of the liquid phase substantially attenuates the gas temperature fluctuations on the laden stream side of the layer (Fig.20a) due to convective thermal energy absorption (Q) by the evaporating droplets. On the initially unladen side of the layer, the mass of liquid penetrating it is relatively small, and therefore only negligible thermal energy attenuation is found for

$x_2 > 0$ in Fig.20a. The level of attenuation increases with increasing droplet loading, but is unaltered by changes in the initial droplet Stokes number due to the fixed ML (Fig.20c). In contrast to the rms gas temperature, the rms droplet temperatures in Figs.20b and 20d show two distinct enhanced thermal fluctuation intensity peaks located on both the inner and outer edges of the layer. This behavior occurs even for the $ML = 0.02$ ‘fluid element’ droplets due to the droplet devoid vorticity regions located approximately along the $x_2 = 0$ plane (see Figs.12 and 13). Therefore the averaging procedure which produces the $ML = 0.02$ profile in Fig.20b is essentially an average of the gas phase temperature (because $T_d \approx T_G$ locally for $ML = 0.02$ droplets) conditioned primarily only on high strain (and temperature) regions near the $x_2 = 0$ plane of the layer; the small spatial sampling therefore has a reduced rms due to the more uniform gas and droplet temperatures within the confined spatial braid region. However, near $x_2/\delta_\omega = +0.5$ the number density contours in Fig.9 suggest that the number droplets on the edge of the primary vortex becomes significant, thereby increasing $T_{d,rms}$ due to more widespread sampling, thus producing the second peak in the profile. As the mass loading is increased, the added total thermal inertia reduces both the gas phase temperature fluctuations through Q effects and the vortical development of the layer, while simultaneously reducing the effective response of droplets to changes in the surrounding gas temperature. Therefore, both $T_{d,rms}$ and the formation of double peaks is reduced for increasing ML in Fig.20b. Changes in the initial droplet Stokes number for constant mass loading are not found to cause significant changes in the gas phase temperature fluctuations (Fig.20c), as has been observed previously for the vorticity development and the velocity component energies. Finally, the $T_{d,rms}$ profiles in Fig.20d as a function of St_0 behave similarly to those in Fig.20b for changes in ML ; however, the appearance of the double peaks is in this case enhanced for large droplets. This occurs because the vortical development and gas phase temperature rms are both unaffected by St_0 , whereas the preferential concentration mechanism is considerably increased for larger initial droplet Stokes numbers (Fig.13b).

5 Conclusions

Results have been presented from direct numerical simulations (DNS) of a three-dimensional, temporally developing, initially isothermal gas mixing layer with one evaporating hydrocarbon-droplet laden stream. The simulations were conducted in the Eulerian-Lagrangian reference frame in which every individual droplet is tracked through the solution of time dependent equations for each droplet position, velocity, temperature and mass. The evaporation model is based on the non-equilibrium Langmuir-Knudsen law, and the interior droplet temperature is considered to be uniform through the assumption of infinite liquid thermal conductivity. Complete two-way phase coupling was incorporated based on a new formulation of the energy coupling term which is valid for non-equal liquid and vapor heat capacities. This formulation was shown to be dependent on proper specifications for the vapor enthalpy, internal energy and the latent heat of vaporization. It was shown that the latent heat must be defined as a linear function of temperature for the calorically perfect species considered in this study. The carrier gas and liquid/vapor species correspond to ‘pseudo-air’ and ‘pseudo-decane,’ respectively. For the present conditions, ‘pseudo’ refers to the fact that viscous properties are defined using artificially inflated values to match a specified initial Reynolds number; however, heat capacities, molecular weights, reference enthalpy and remaining properties are calculated from correlations for the ‘real’ species defined at an appropriate reference temperature. Using this formulation, a variety of simulations were conducted under fixed gas flow conditions by varying several of the pertinent droplet parameters, including the initial liquid mass loading ratio and the initial monodisperse droplet Stokes number. The DNS results were used primarily for studying the issues of evaporative flow saturation, preferential concentration and flow modulation.

The growth rate and kinetic energy development of the mixing layer were both found to be increasingly attenuated by the droplets for increasing mass loading ratios; however, changes in the initial Stokes numbers in the range $0.50 \leq St_0 \leq 2.00$ at fixed mass loading showed no significant effects on the evolution of the layer. In all but the smallest mass loading cases, the mixing layer saturates during the early stages of mixing as characterized by premature cessation of evaporation in the laden stream resulting from: (1) build up of vapor mass fraction, and

(2) a reduction in the gas temperature caused by latent heat effects. However, as the mixing layer grows, droplets are continually entrained into the layer where they are further evaporated by contact with the higher temperature unladen stream fluid. The saturation process was shown to result in a quasi-steady distribution of droplets sizes characterized by a nearly constant mean droplet mass in the laden stream, and by a monotonically decreasing mean size profile across the interior of the layer. The total range of droplet sizes (polydispersity) found within the layer at final times increases with both increasing mass loading and increasing initial droplet Stokes number. The qualitative nature of the saturation is essentially the same for all of the performed simulations; however, the quantitative final state of the layer is determined primarily by the mass loading ratio, and to a lesser extent by the initial droplet temperature.

Both flow visualizations and statistical analyses based on conditionally averaged flow variables on the second invariant of the deformation tensor were used to study the instantaneous organization of the droplets as well as the extent of preferential concentration in the two-phase mixing layer. Concentration streaks were observed to form in the braid regions between spanwise vortices similar to previous results from two-dimensional simulations and experiments using solid particles. However, the strong three-dimensionality of the present flow field additionally causes the streaks to wrap around the periphery of streamwise vortices, thus causing the formation of concentration 'mushroom' structures in the braid regions. The flow visualization was further used to extend past observations from solid particle dispersion experiments which noted the existence of regions of persistent positive and negative velocity slip. These regions and their locations relative to the primary spanwise vortices were found to form in a similar, though somewhat more complex, manner for evaporating droplets in highly three-dimensional shear flow. Furthermore, these ideas were extended to the temperature field which was found to contain similar regions of persistent positive and negative temperature slip. The slip temperature regions we found to correspond inversely to the velocity slip regions for solid particles; however, they have a substantially more complex distribution for evaporating droplets. Conditional averaging on the second invariant showed that droplets are preferentially concentrated in high strain regions of the flow and have larger sizes than the relatively fewer droplets remaining within vortical structures. Effects of evaporation, mass loading and initial Stokes number on the preferential concentration were also discussed.

Cross stream profiles of first and second order flow statistics at the final simulation times were used in order to examine the structure of the velocity and temperature fields of both phases, as well as the extent of flow modulation imposed on the gas phase by the droplets. The results show that both the mean streamwise gas velocity and the Eulerian number density profiles coincide for all droplet mass loadings when the cross stream coordinate is normalized by the instantaneous vorticity thickness. In contrast, mean profiles of thermodynamic flow variables do not coincide. Peaks in all of the mean number density profiles indicated a region of enhanced droplet concentration at the inner edge of the layer, similar to existing observations of solid particle dispersion. Both the kinetic and thermal energies of the gas phase were observed to be attenuated by the droplets as shown through the cross stream profiles of second order statistics of the gas velocity components and temperature. The kinetic energy attenuation is strongest for the cross stream velocity component. On the other hand, the streamwise velocity component energy is slightly increased by droplets at the center of the layer, but attenuated on either edge of the layer. The gas phase thermal energy was also found to be attenuated by droplets, but primarily only on the laden stream side of the layer. A comparison with the second order statistics of the droplet velocity showed that the component energies are larger for the droplets than for the gas phase in both the streamwise and spanwise directions within the unladen stream side of the layer; the latter finding was attributed to the strong three-dimensionality of the present flow. However, the intensities of both the cross stream velocity and the temperature fluctuations were found to be largest for the gas phase in all cases. In all of the above, the primary effects of the droplets on the quantitative results were found to be due to the liquid mass loading ratio; changes in the initial Stokes number (within the range $0.5 \leq St_0 \leq 2.0$) for fixed loading had a nearly negligible influence on the gas flow modulation.

Acknowledgments

This research was conducted at the California Institute of Technology's Jet Propulsion Laboratory (JPL) and sponsored by General Electric (GE) through the Air Force Office of Scientific Research (AFOSR) Focused Research Initiative program with Dr. Hukam Mongia from GE serving as contract monitor. The authors would like to thank Dr. Kenneth Harstad of JPL and Dr. Farzad Mashayek of the University of Hawaii for helpful discussions. Computational resources were provided by the supercomputing facility at JPL.

References

- B. Balachandar and M.R. Maxey. Methods for evaluating fluid velocities in spectral simulations of turbulence. *J. Comp. Phys.*, 83:96–125, 1989.
- J. Bellan and R. Cuffel. A theory of nondilute spray evaporation based upon multiple drop interactions. *Comb. and Flame*, 51:55–67, 1983.
- J. Bellan and K. Harstad. Analysis of the convective evaporation of nondilute clusters of drops. *Int. J. Heat Mass Transfer*, 30(1):125–136, 1987.
- L.P. Bernal and A. Roshko. Streamwise vortex structures in plane mixing layers. *J. Fluid Mech.*, 170:499–525, 1986.
- G.L. Brown and A. Roshko. On density effects and large scale structure in turbulent mixing layers. *J. Fluid Mech.*, 64:775–816, 1974.
- C.R. Carlson and R.L. Peskin. One-dimensional particle velocity probability densities measured in turbulent gas-particle duct flow. *Int. J. Multiphase Flow*, 2:67–78, 1975.
- R. Chein and J.N. Chung. Effects of vortex pairing on particle dispersion in turbulent shear flows. *Int. J. Multiphase Flows*, 13(6):785–802, 1987.
- K.A. Cliffe and D.A. Lever. Isothermal flow past a blowing sphere. *Int. J. Numerical Methods Fluids*, 5:709–725, 1985.
- C.T. Crowe, M.P. Sharma, and D.E. Stock. The particle source in cell (psi-cell) model for gas-droplet flows. *J Fluids Eng.*, 6:325–332, 1977.
- C.T. Crowe, T.R. Troutt, and J.N. Chung. Particle interaction with vortices. In S.I. Green, editor, *Fluid Vortices*, pages 829–861. Kluwer Academic Publishers, Netherlands, 1995.
- J.K. Eaton and J.R. Fessler. Preferential concentration of particles by turbulence. *Int. J. Multiphase Flow*, 20:169–209, 1994.
- S. Elghobashi. On predicting particle-laden turbulent flows. *Appl. Sci. Res.*, 52:309–329, 1994.
- S. Elghobashi and G.C. Truesdell. On the two-way interaction between homogeneous turbulence and dispersed solid particles. i: Turbulence modification. *Phys. Fluids A*, 5(7):1790–1801, 1993.
- G.A.E. Godsave. Studies of the combustion of drops in a fuel spray: The burning of single drops of fuel. In *Proceedings of the Fourth Symposium (International) on Combustion*, pages 818–830. 1953.
- R.A. Gore and C.T. Crowe. Effect of particle size on modulating turbulent intensity. *Int. J. Multiphase Flow*, 15:279–285, 1989.
- K. Harstad and J. Bellan. Behavior of a polydisperse cluster of interacting drops evaporating in an inviscid vortex. *Int. J. Multiphase Flow*, 23(5):899–925, 1997.
- L.S. Huang and C.M. Ho. Small-scale transition in a plane mixing layer. *J. Fluid Mech.*, 210:475–500, 1990.
- R. Jackson and B.J. Davidson. An equation set for non-equilibrium two phase flow, and an analysis of some aspects of choking, acoustic propagation, and losses in low pressure wet steam. *Int. J. Multiphase Flow*,

- 9(5):491-510, 1983.
- C.A. Kennedy and M.H. Carpenter. Several new numerical methods for compressible shear-layer simulations. *App. Num. Math.*, 14:397-433, 1994.
- V.M. Kenning and C.T. Crowe. On the effect of particles on carrier phase turbulence in gas-particle flows. *Int. J. Multiphase Flow*, 23(2):403-408, 1997.
- K.T. Kiger and J.C. Lasheras. The effect of vortex pairing in particle dispersion and kinetic energy transfer in a two-phase turbulent shear layer. *J. Fluid Mech.*, 302:149-178, 1995.
- K.T. Kiger and J.C. Lasheras. Dissipation due to particle/turbulence interaction in a two-phase, turbulent, shear layer. *Phys. Fluids*, 9(10):3005-3023, 1997.
- J.D. Kulick, J.R. Fessler, and J.K. Eaton. Particle response and turbulence modification in fully developed channel flow. *J. Fluid Mech.*, 277:109-134, 1994.
- B.J. Lazaro and J.C. Lasheras. Particle dispersion in a turbulent, plane, free shear layer. *Phys. Fluids A*, 1:1035-1044, 1989.
- B.J. Lazaro and J.C. Lasheras. Particle dispersion in a developing free shear layer. Part 1. Unforced flow. *J. Fluid Mech.*, 235:143-178, 1992.
- B.J. Lazaro and J.C. Lasheras. Particle dispersion in a developing free shear layer. Part 2. Forced flow. *J. Fluid Mech.*, 235:179-221, 1992.
- L.M. Liljegren. The effect of a mean fluid velocity gradient on the streamwise velocity variance of a particle suspended in a turbulent flow. *Int. J. Multiphase Flow*, 19(5):471-484, 1993.
- E.K. Longmire and J.K. Eaton. Structure and control of a particle laden round jet. *J. Fluid Mech.*, 236:217-258, 1992.
- J.E. Martin and E. Meiburg. The accumulation and dispersion of heavy particles in forced two-dimensional mixing layers. I. The fundamental and subharmonic cases. *Phys. Fluids*, 6(3):1116-1132, 1994.
- F. Mashayek. Direct numerical simulations of evaporating droplet dispersion in forced low mach number turbulence. *Int. J. Heat Mass Transfer*, 1998. In Press.
- F. Mashayek. Droplet-turbulence interactions in low mach number homogeneous shear two-phase flows. *J. Fluid Mech.*, 1998. Submitted.
- F. Mashayek, F.A. Jaber, R.S. Miller, and P. Givi. Dispersion and polydispersity of droplets in stationary isotropic turbulence. *Int. J. Multiphase Flow*, 23(2):337-355, 1997.
- R.W. Metcalfe, S.A. Orszag, M.E. Brachet, S. Menon, and J.J. Riley. Secondary instabilities of a temporally growing mixing layer. *J. Fluid Mech.*, 184:207-243, 1987.
- R.S. Miller and J. Bellan. On the validity of the assumed pdf method for modeling binary mixing/reaction of evaporated vapor in gas/liquid-droplet turbulent shear flow. *Proceedings of the Twenty Seventh Symposium (International) on Combustion*, 1998. Submitted.
- R.S. Miller, K. Harstad, and J. Bellan. Evaluation of equilibrium and non-equilibrium evaporation models for many-droplet gas-liquid flow simulations. *Int. J. Multiphase Flow*, 1998. Submitted.
- R.S. Miller, C.K. Madnia, and P. Givi. Structure of a turbulent reacting mixing layer. *Comb. Sci. Tech.*, 99:1-36, 1994.
- R.D. Moser and M.M. Rogers. Mixing transition and the cascade to small scales in a plane mixing layer. *Physics of Fluids A*, 3(5):1128-1134, 1991.
- T.J. Poinsot and S.K. Lele. Boundary conditions for direct numerical simulations of compressible viscous flows. *J. Comp. Physics*, 101:104-129, 1992.
- W.E. Ranz and W.R. Marshall. Evaporation from drops: I. *Chem. Engng. Prog.*, 48:141-146, 1952.
- W.E. Ranz and W.R. Marshall. Evaporation from drops: II. *Chem. Engng. Prog.*, 48:173-180, 1952.
- J.J. Riley, R.W. Metcalfe, and S.A. Orszag. Direct numerical simulations of chemical reacting mixing layers. *Phys. Fluids*, 29(2):406-422, 1986.
- C.B. Rogers and J.K. Eaton. Particle transport in a vertical turbulent boundary layer. *Int. J. Multiphase Flow*, 16:819-834, 1990.

- M. Samimy and S.K. Lele. Motion of particles with inertia in a compressible free shear layer. *Phys. Fluids*, 3:1915–1923, 1991.
- N. Sandham and W. Reynolds. The compressible mixing layer: Linear theory and direct simulations. *AIAA Paper 89-0371*, 1989.
- S.L. Soo, H.K. Ihrig, and A.F. El Kouh. Experimental determination of statistical properties of two-phase turbulent motion. *J. Bas. Engng*, 20:1–13, 1960.
- D.B. Spalding. The combustion of liquid fuels. In *Proceedings of the Fourth Symposium (International) on Combustion*, pages 847–864. 1953.
- K.D. Squires and J.K. Eaton. Particle response and turbulence modification in isotropic turbulence. *Phys. Fluids A*, 2(7):1191–1203, 1990.
- K.D. Squires and J.K. Eaton. Preferential concentration of particles by turbulence. *Phys. Fluids A*, 3(5):1169–1178, 1991.
- J.L. Steimke and A.E. Dukler. Laser doppler velocimeter measurements of aerosols in turbulent pipe flow. *Int. J. Multiphase Flow*, 9:751–754, 1983.
- Y. Tsuji and Y. Morikawa. LDV measurements of an air-solid two-phase flow in a horizontal pipe. *J. Fluid Mech.*, 120:385–409, 1982.
- F. Wen, N. Kamalu, J.N. Chung, and C.T. Crowe. Particle dispersion by vortex structures in plane mixing layers. *ASME J. Fluids Eng.*, 114(4):657–666, 1992.
- F.A. Williams. *Combustion Theory*. Addison Wesley, Reading, Massachusetts, 1965.
- C.D. Winant and F.K. Browand. Vortex pairing: The mechanisms of turbulent mixing layer growth at moderate Reynolds number. *J. Fluid Mech.*, 63:237–255, 1973.
- J.B. Young. The fundamental equations of gas-droplet multiphase flow. *Int. J. Multiphase Flow*, 21(2):175–191, 1995.
- L. Zhou. *Theory and Numerical Modeling of Turbulent Gas-Particle Flows and Combustion*. Science Press, Beijing, China, 1993.

Figure Captions

Figure 1: Schematic of the two-phase, temporally developing mixing layer.

Figure 2: Temporal evolution of normalized vorticity thickness for (a) various values of the initial liquid loading with $St_0 = 1.02$ (data from simulations Run 0 - Run 5) and (b) for various values of the initial Stokes number with $ML = 0.125$ (data from simulations Run 6, Run 3 and Run 7).

Figure 3: Temporal evolution of the total liquid mass normalized by the initial value [(a),(c)] and the total evaporated liquid mass normalized by the total carrier gas mass [(b),(d)] for; (a),(b) various values of the initial liquid loading with $St_0 = 1.02$ (data from simulations Run 0 - Run 5) and (c),(d) for various values of the initial Stokes number with $ML = 0.125$ (data from simulations Run 6, Run 3 and Run 7).

Figure 4: Temporal evolutions of integral flow statistics for different values of the initial droplet temperature ($ML = 0.225$, $St_0 = 1.02$) corresponding to simulations Run 4 and Run 9: (a) mean droplet temperature averaged over all droplets, (b) total liquid mass normalized by the initial value.

Figure 5: Cross stream variation of the vapor mass fraction statistics at time $t\Delta U_0/\delta_{\omega,0} = 50$ for various values of the initial liquid loading ($St = 1.02$): (a) mean vapor mass fraction in the gas phase (b) mean droplet surface vapor mass fraction. The data correspond to the results of simulations Run 0 - Run 5.

Figure 6: Cross stream variation of temperature statistics at time $t\Delta U_0/\delta_{\omega,0} = 50$ for various values of the initial liquid loading ($St = 1.02$): (a) mean gas temperature (b) mean droplet temperature, (c) mean slip temperature at droplet locations. The data correspond to the results of simulations Run 0 - Run 5.

Figure 7: Cross stream variation of the normalized mean droplet mass at time $t\Delta U_0/\delta_{\omega,0} = 50$ for various values of (a) the initial liquid loading ($St = 1.02$; results from simulations Run 0-Run 5), (b) the initial droplet Stokes number ($ML = 0.125$; results of simulations Run 6, Run 3 and Run 7).

Figure 8: Cross stream variation of the PDF of the normalized droplet mass at time $t\Delta U_0/\delta_{\omega,0} = 50$ ($St = 1.02$): (a) simulation Run 3 with $ML = 0.125$, (b) simulation Run 5 with $ML = 0.35$.

Figure 9: Instantaneous contour plot of the Eulerian droplet number density at time $t\Delta U_0/\delta_{\omega,0} = 50$ from Run 4 with $ML = 0.225$: (a) spanwise plane between streamwise rollers at $x_3/L_3 = 0$, (b) spanwise plane intersecting a streamwise roller at $x_3/L_3 \approx 0.4$, (c) streamwise plane in the braid region at $x_1/L_1 = 0$. Darker regions indicate increased magnitude.

Figure 10: Instantaneous contour plot of the Eulerian droplet slip velocity u''_{sl} at time $t\Delta U_0/\delta_{\omega,0} = 50$ from Run 4 with $ML = 0.225$: (a) spanwise plane between streamwise rollers at $x_3/L_3 = 0$; I and II are positive; II, IV and V are negative, (b) spanwise plane intersecting a streamwise roller at $x_3/L_3 \approx 0.4$ (I and III are positive; II is negative), (c) streamwise plane in the braid region at $x_1/L_1 = 0$ (I is positive; II and III are negative). Units are m/s .

Figure 11: Instantaneous contour plot of the Eulerian droplet slip temperature T''_{sl} at time $t\Delta U_0/\delta_{\omega,0} = 50$ from Run 10 (no evaporation) with $ML = 0.225$, for a spanwise plane between streamwise rollers at $x_3/L_3 = 0$ (I and III are positive; II, IV and V are negative). Units are degrees K .

Figure 12: Instantaneous contour plot of the Eulerian droplet slip temperature T''_{sl} at time $t\Delta U_0/\delta_{\omega,0} = 50$ from Run 4 with $ML = 0.225$: (a) spanwise plane between streamwise rollers at $x_3/L_3 = 0$ (II and IV are positive; I and III are negative), (b) spanwise plane intersecting a streamwise roller at $x_3/L_3 \approx 0.4$ (II and III are positive; I is negative), (c) streamwise plane in the braid region at $x_1/L_1 = 0$ (I and II are both positive). Units are degrees K .

Figure 13: Normalized droplet number density conditionally averaged on both the value of the second invariant of the deformation tensor and on scalar values $\phi < 0.5$, at time $t\Delta U_0/\delta_{\omega,0} = 50$ for various values of (a) the initial liquid loading ($St = 1.02$; results from simulations Run 0-Run 5), (b) the initial droplet Stokes number ($ML = 0.125$; results of simulations Run 6, Run 3 and Run 7).

Figure 14: Normalized droplet mass conditionally averaged on the value of the second invariant of the deformation tensor at the droplet locations at time $t\Delta U_0/\delta_{\omega,0} = 50$ for various values of (a) the initial liquid loading ($St = 1.02$: results from simulations Run 0-Run 5), (b) the initial droplet Stokes number ($ML = 0.125$: results of simulations Run 6, Run 3 and Run 7).

Figure 15: Slip temperature conditionally averaged on the value of the second invariant of the deformation tensor at the droplet locations at time $t\Delta U_0/\delta_{\omega,0} = 50$ from (a) simulations Run 10 and Run 11 for non-evaporating droplets with $ML = 0.225$ and $St = 1.02$, and (b) for various values of the initial liquid loading ($St = 1.02$) from simulations Run 0-Run 5.

Figure 16: Cross stream variations of mean Eulerian number density at time $t\Delta U_0/\delta_{\omega,0} = 50$ for various values of (a) the initial liquid loading ($St = 1.02$: results from simulations Run 0-Run 5) and (b) the initial droplet Stokes number ($ML = 0.125$: results of simulations Run 6, Run 3 and Run 7).

Figure 17: Cross stream variations of mean flow variables at time $t\Delta U_0/\delta_{\omega,0} = 50$ for various values of the initial liquid loading ($St = 1.02$): (a) streamwise gas velocity, (b) streamwise droplet velocity, (c) cross stream gas velocity, (d) cross stream droplet velocity. The data correspond to the results of simulations Run 0 - Run 5.

Figure 18: Cross stream variations of mean thermodynamic flow variables at time $t\Delta U_0/\delta_{\omega,0} = 50$ for various values of the initial liquid loading ($St = 1.02$): (a) gas pressure normalized by the initial pressure (atmospheric), (b) gas density. The data correspond to the results of simulations Run 0 - Run 5.

Figure 19: Cross stream variation of normalized rms velocity statistics at time $t\Delta U_0/\delta_{\omega,0} = 50$ for various values of the initial liquid loading ($St = 1.02$): (a) streamwise gas velocity, (b) streamwise droplet velocity, (c) cross stream gas velocity, (d) cross stream droplet velocity, (e) spanwise gas velocity, (f) spanwise droplet velocity. The data correspond to the results of simulations Run 0 - Run 5.

Figure 20: Cross stream variation of normalized rms temperature statistics at time $t\Delta U_0/\delta_{\omega,0} = 50$ for various values of the initial liquid loading [(a),(b); $St = 1.02$, data from simulations Run 0 - Run 5] and for various values of the initial droplet Stokes number [(c),(d); $ML = 0.125$, data from simulations Run6, Run 3 and Run 7]: (a),(c) gas temperature, (b),(d) droplet temperature.

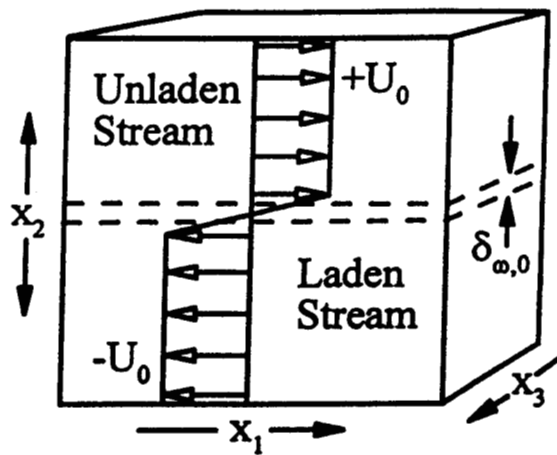


Fig. 1

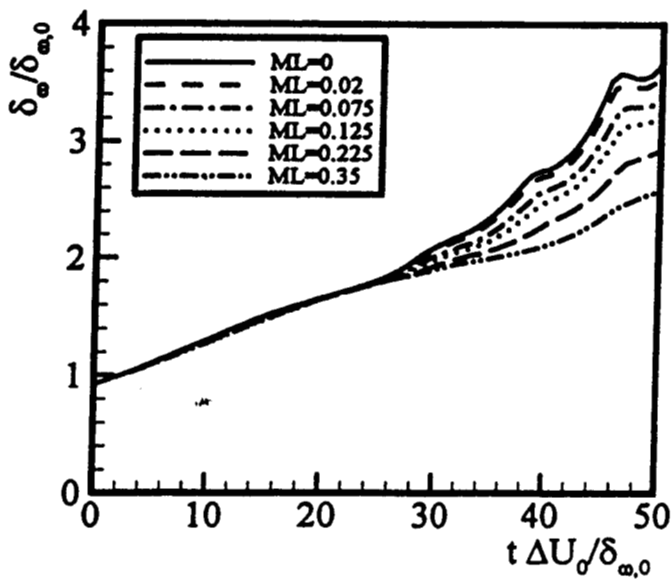


Fig. 2a

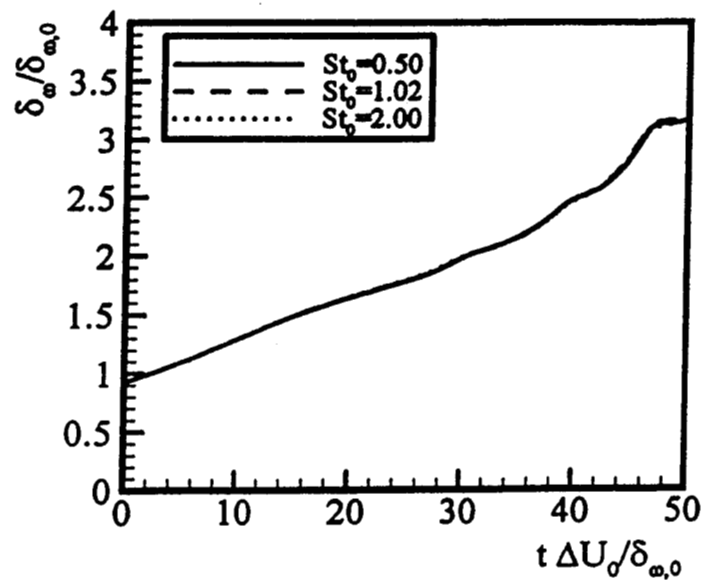


Fig. 2b

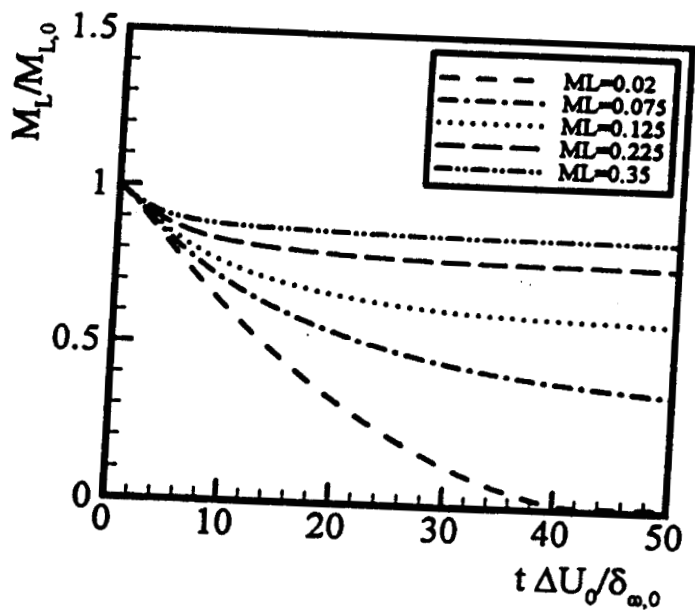


Fig. 3a

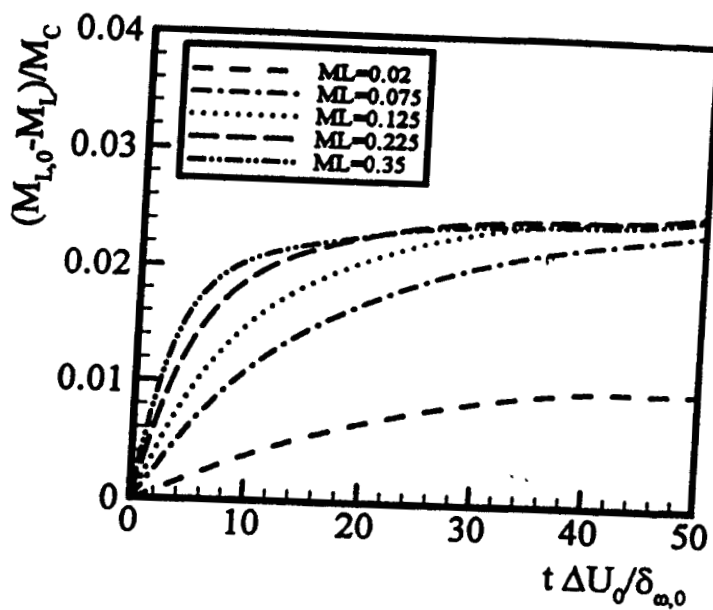


Fig. 3b

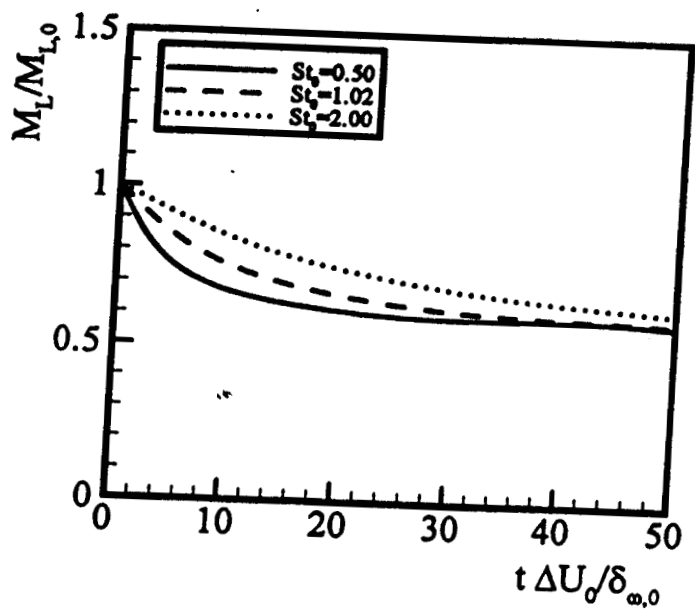


Fig. 3c

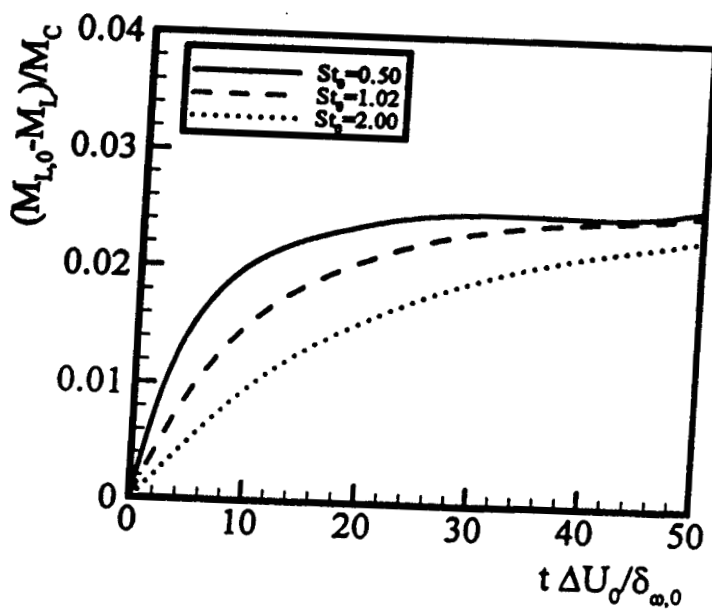


Fig. 3d

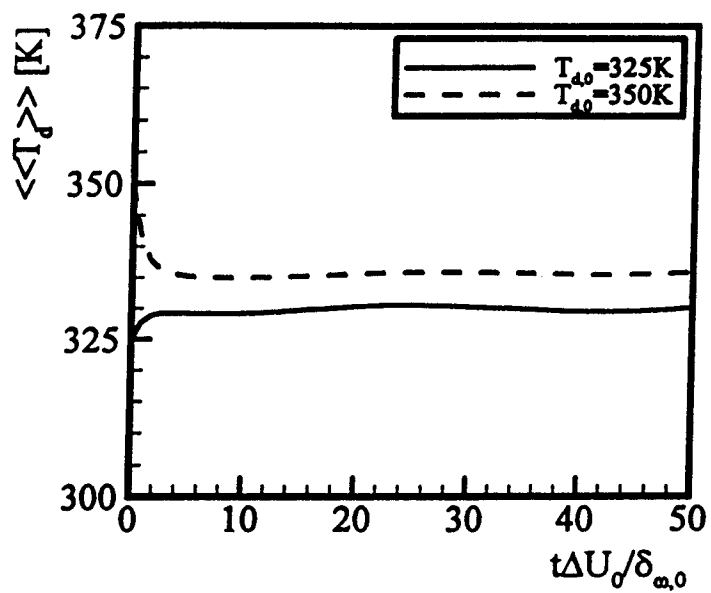


Fig. 4a

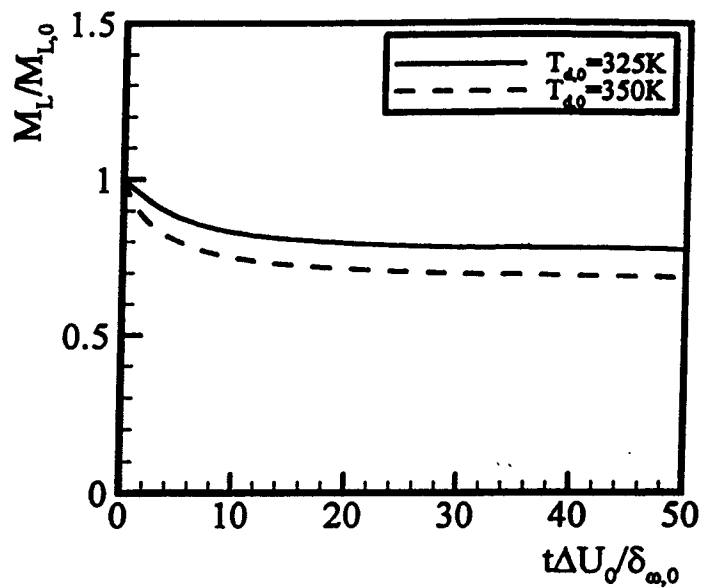


Fig. 4b

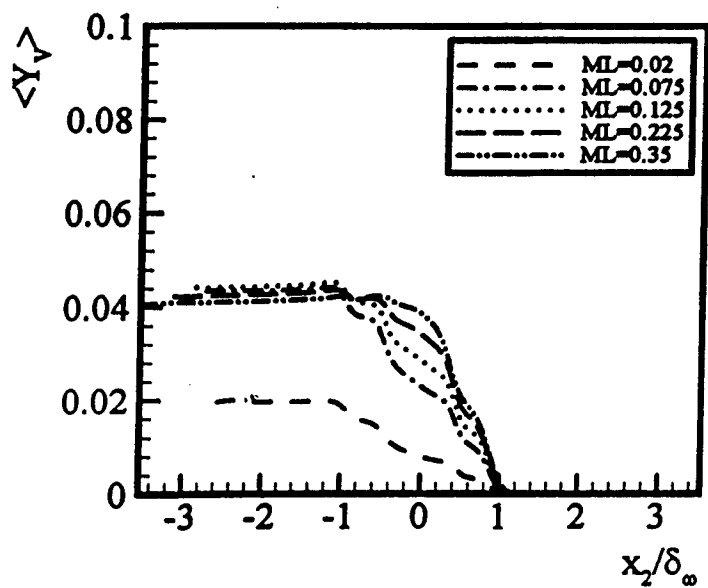


Fig. 5a

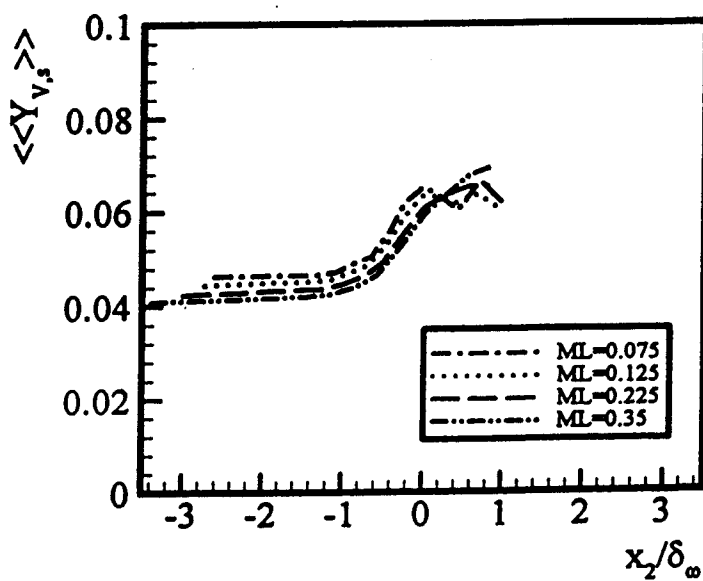


Fig. 5b

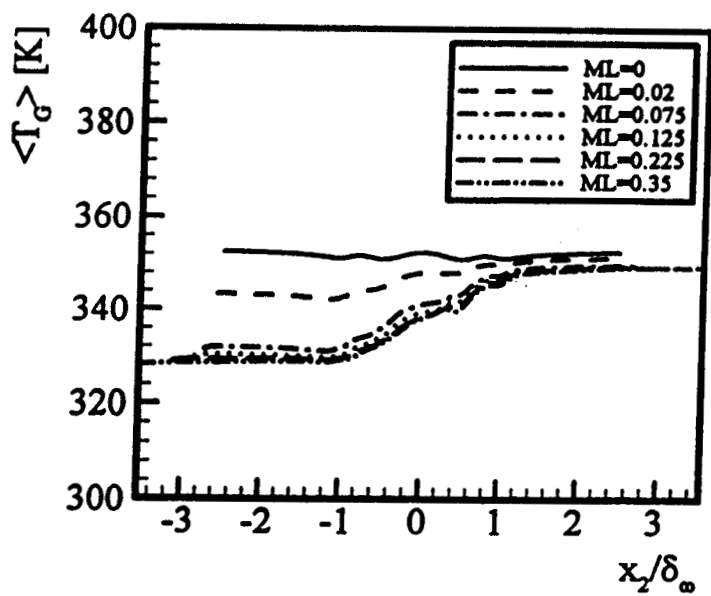


Fig. 6a

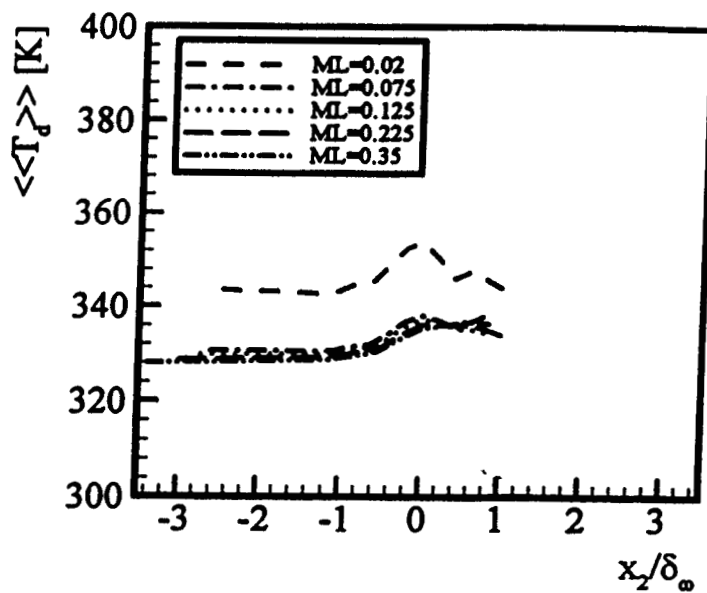


Fig. 6b

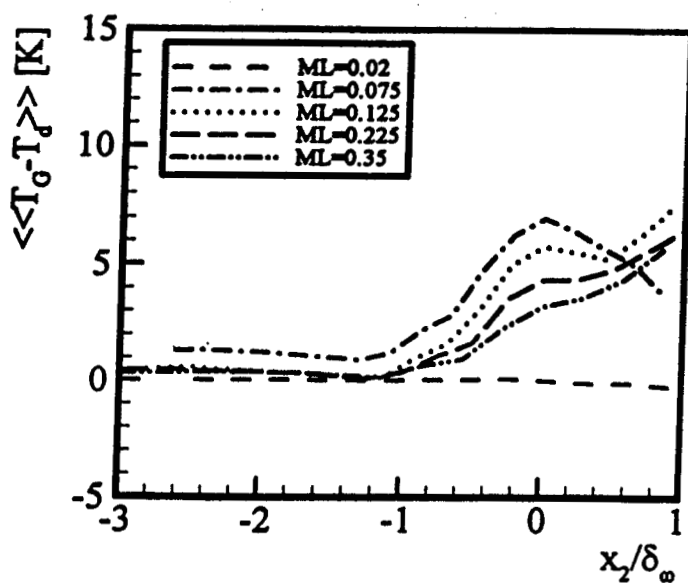


Fig. 6c

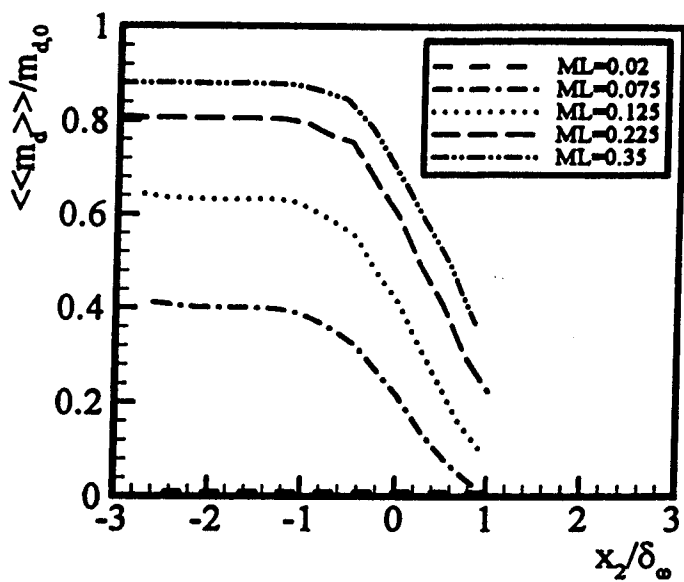


Fig. 7a

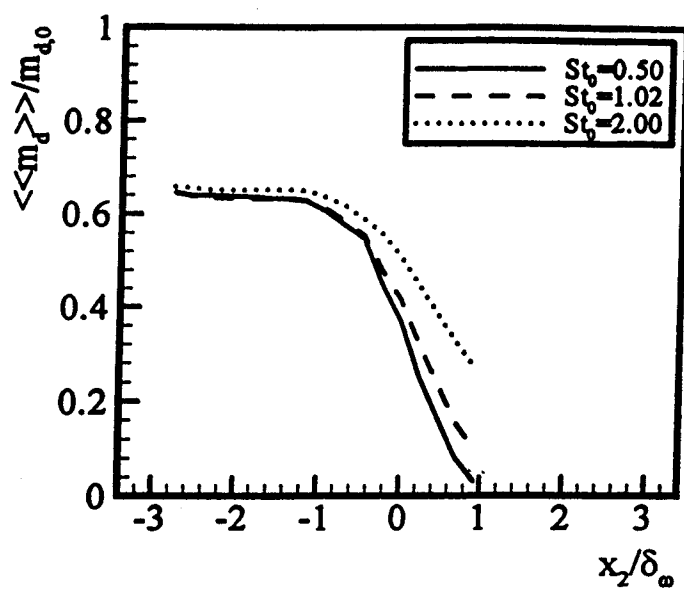


Fig. 7b

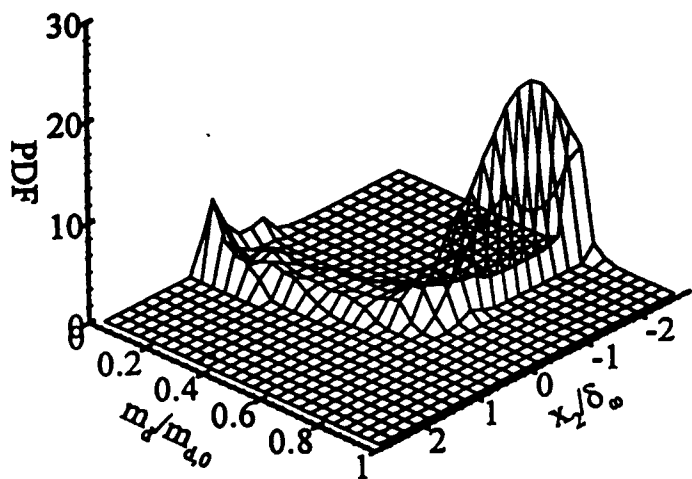


Fig. 8a

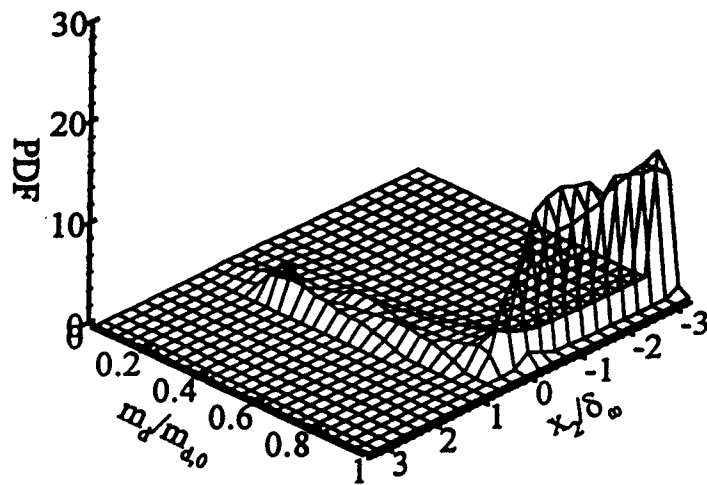


Fig. 8b

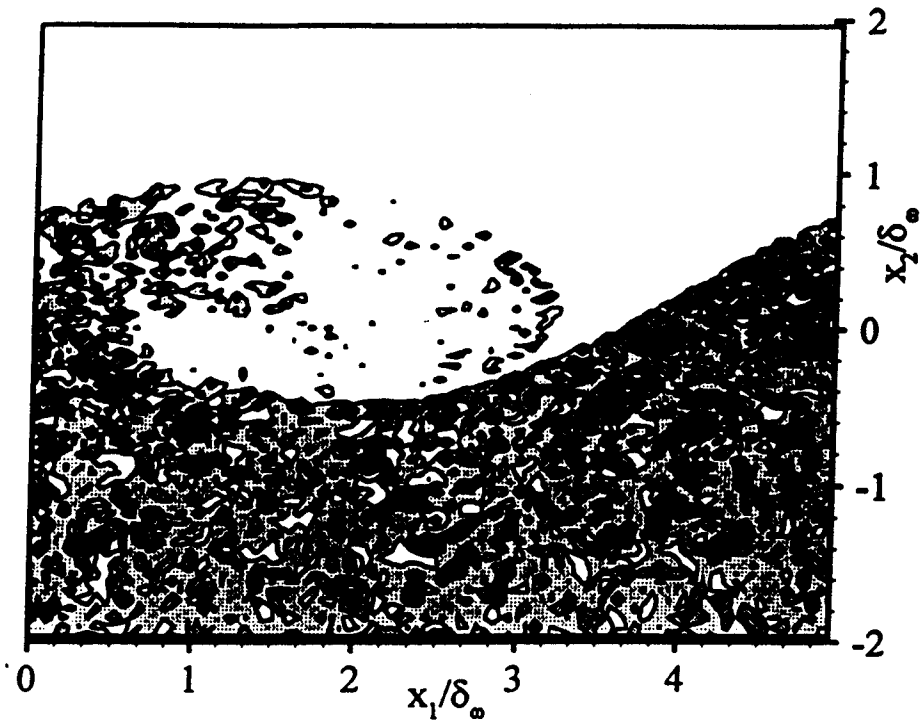


Fig. 9a

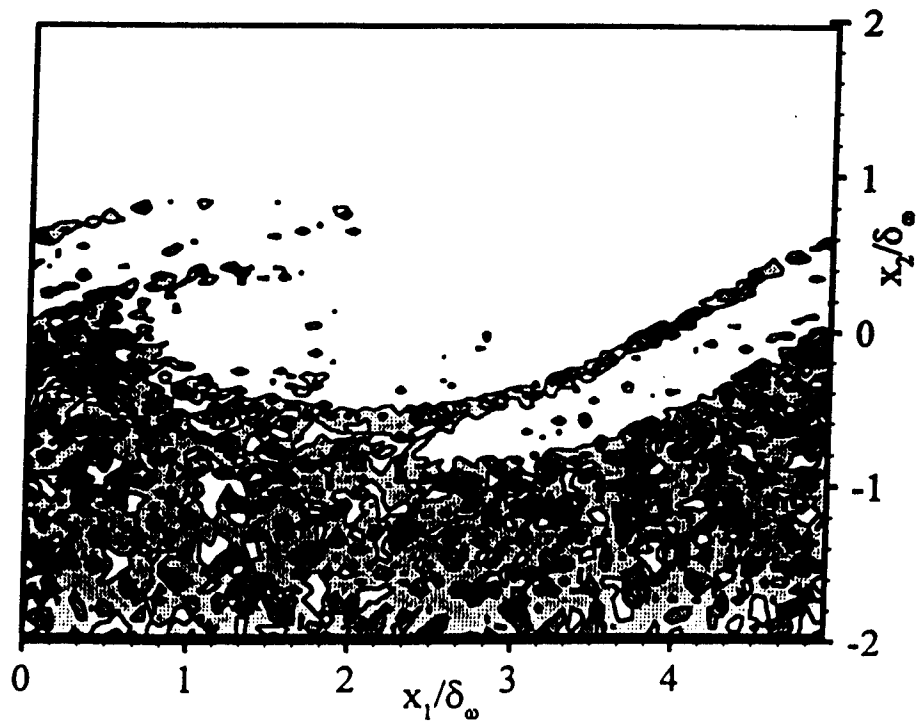


Fig. 9b

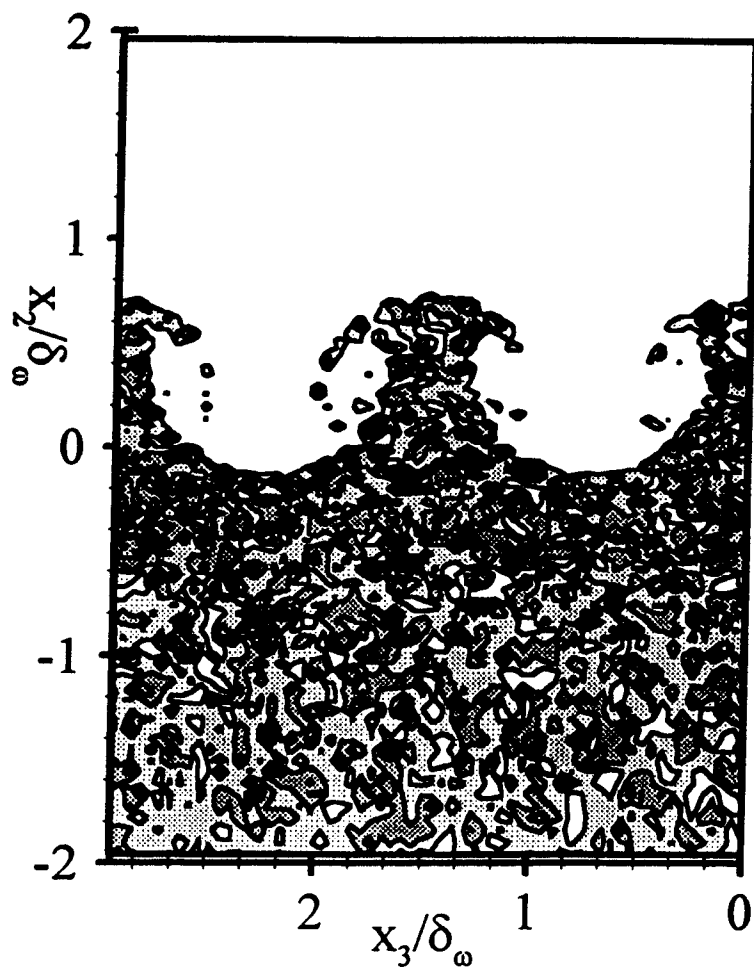


Fig. 9c

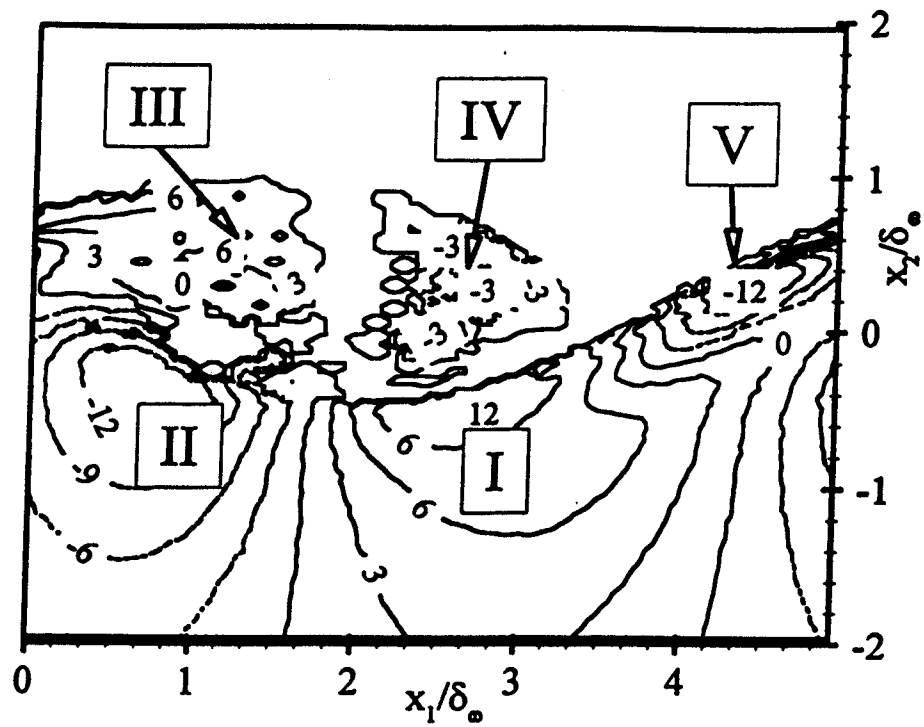


Fig. 10a

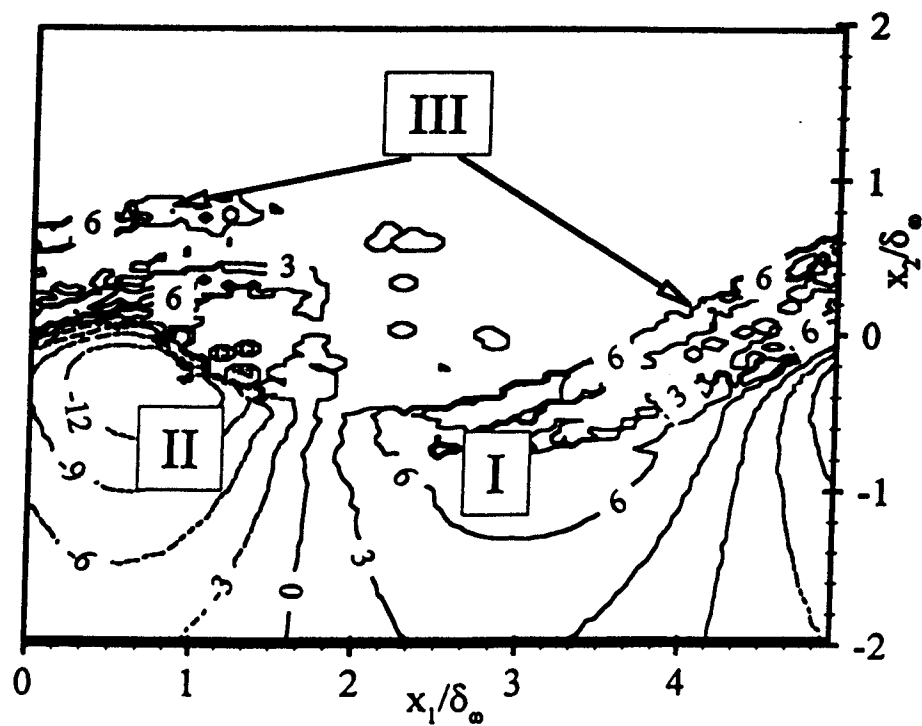


Fig. 10b

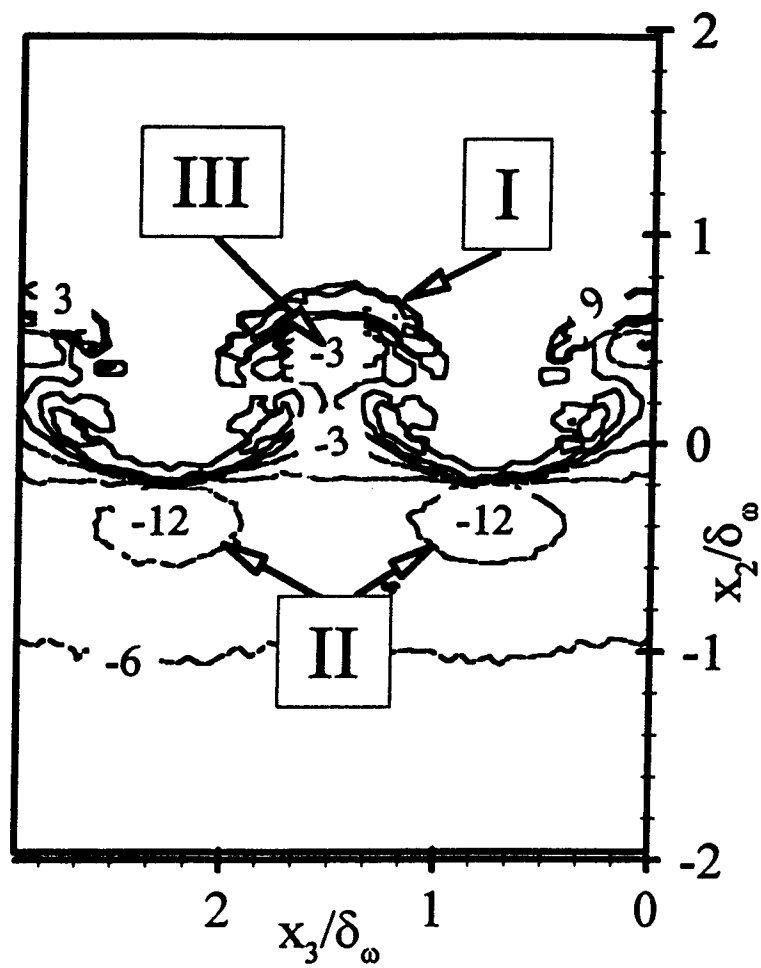


Fig. 10c

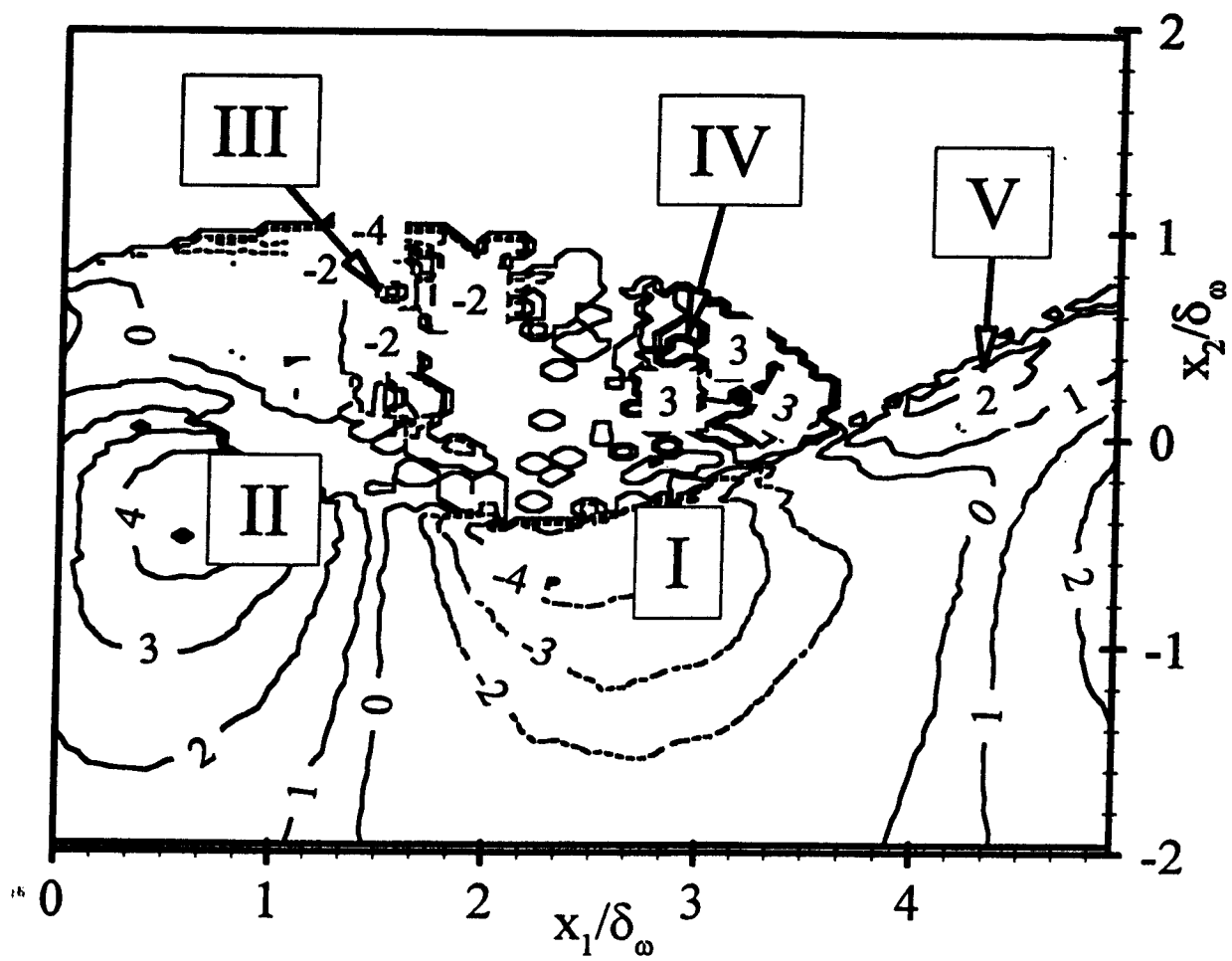


Fig. 11

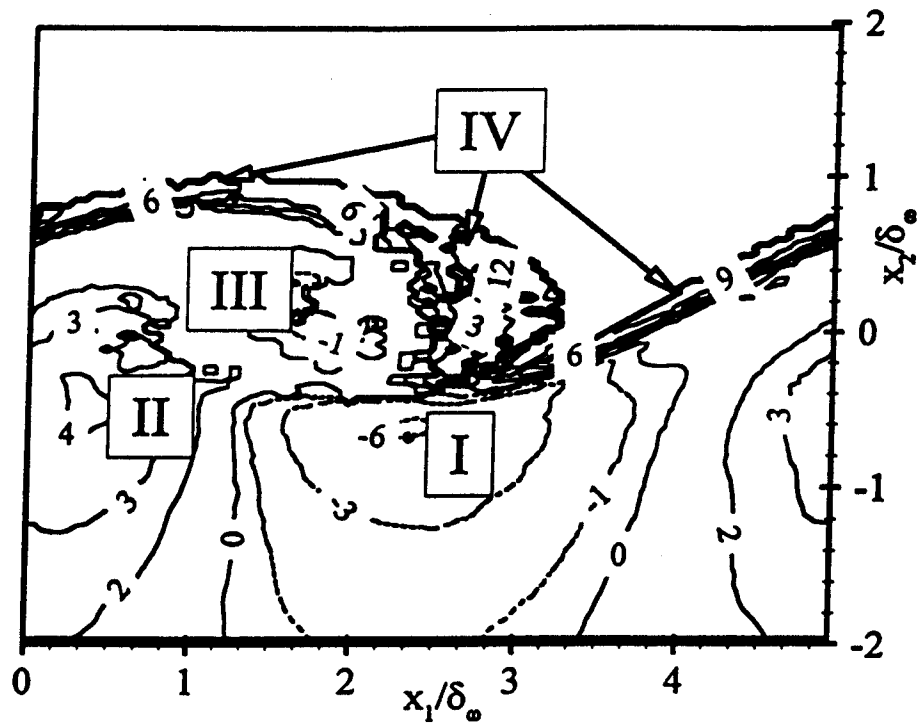


Fig. 12a

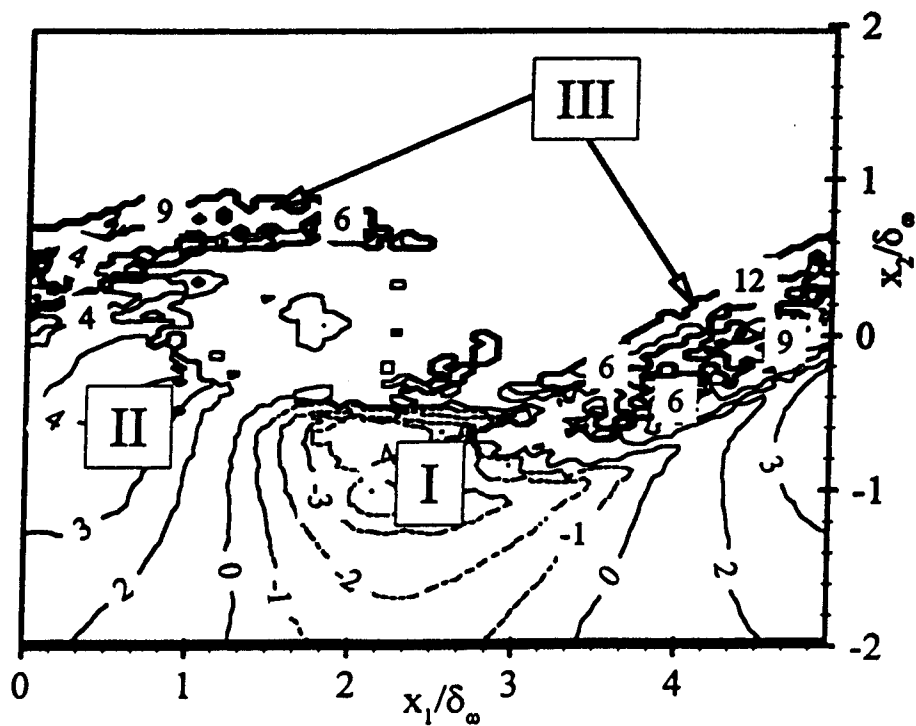


Fig. 12b

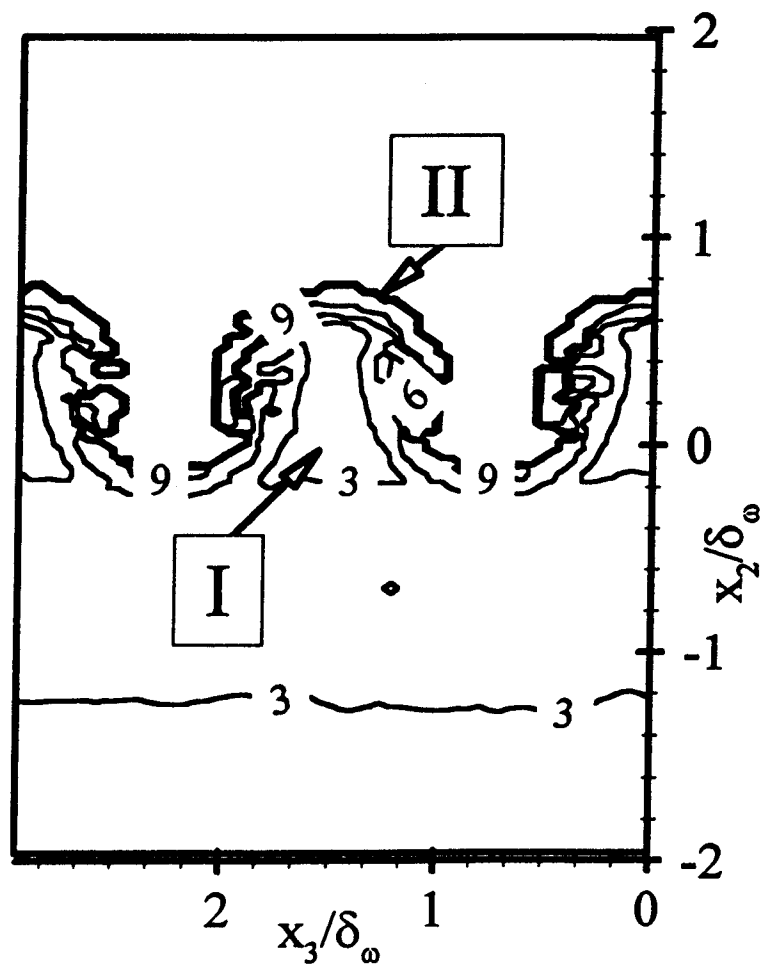


Fig. 12c

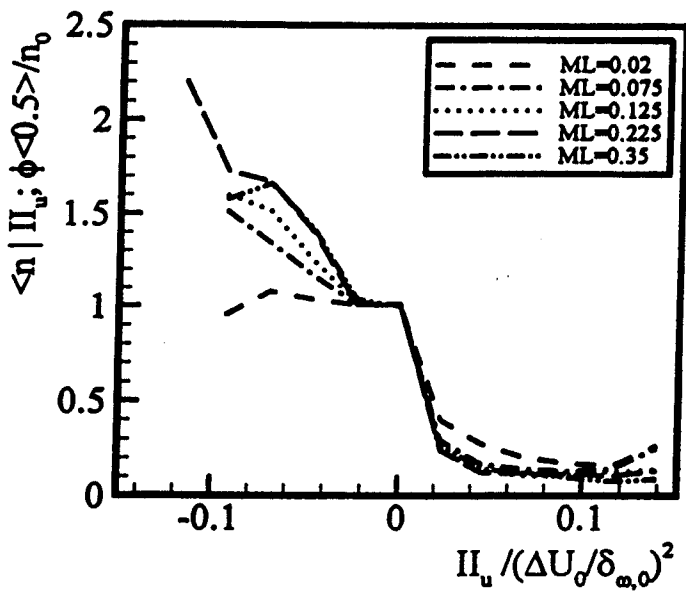


Fig. 13a

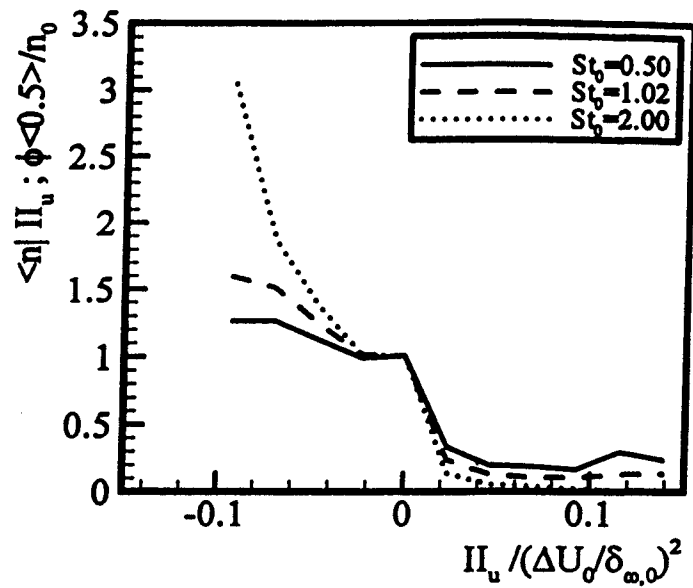


Fig. 13b

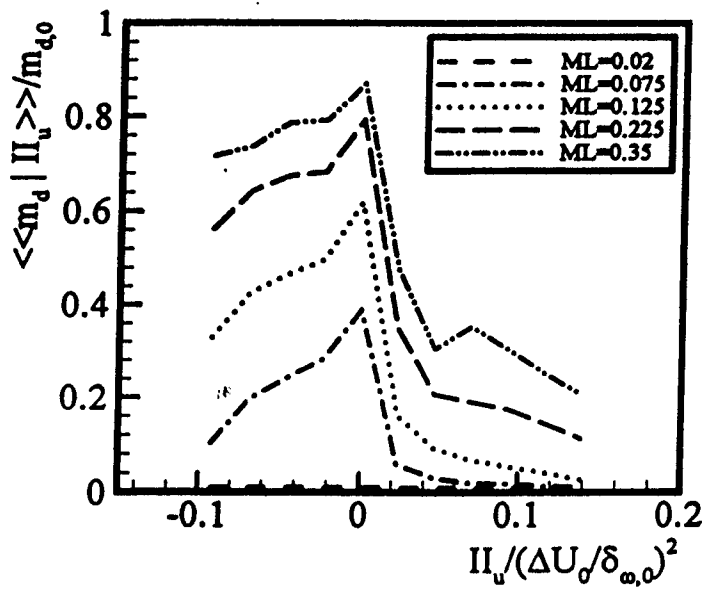


Fig. 14a

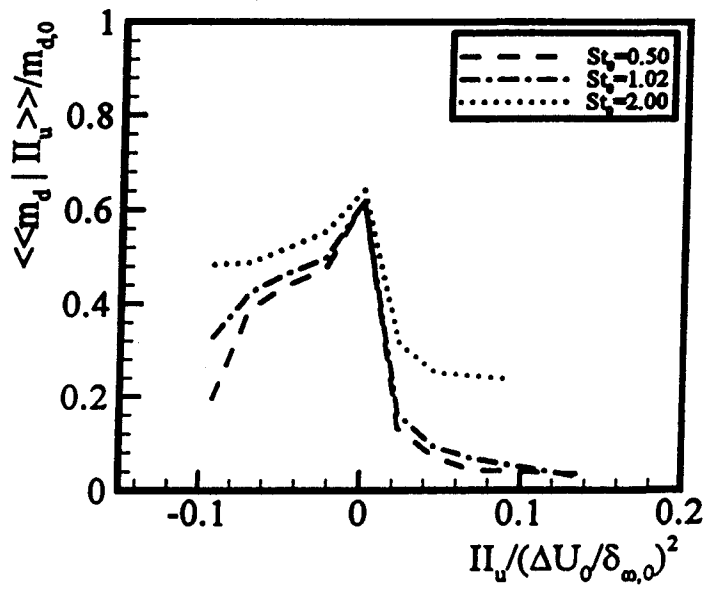


Fig. 14b

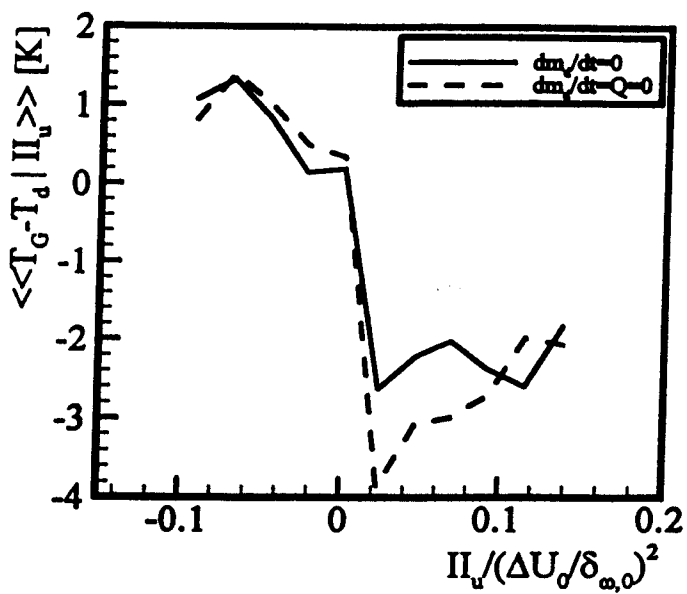


Fig. 15a

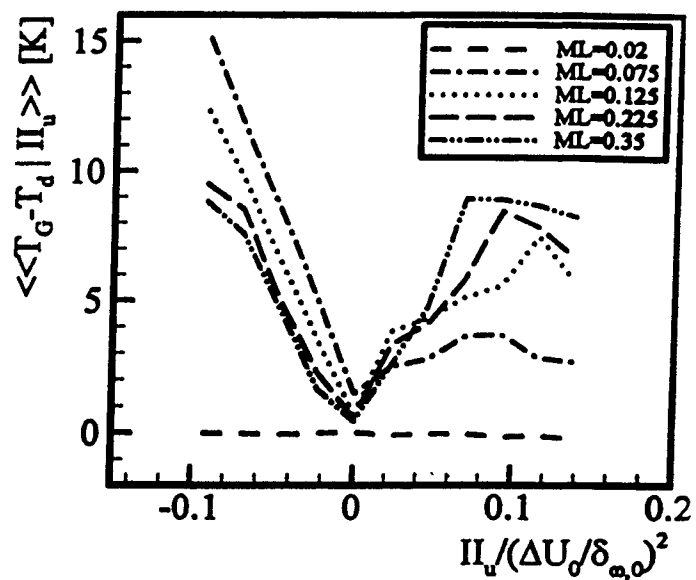


Fig. 15b

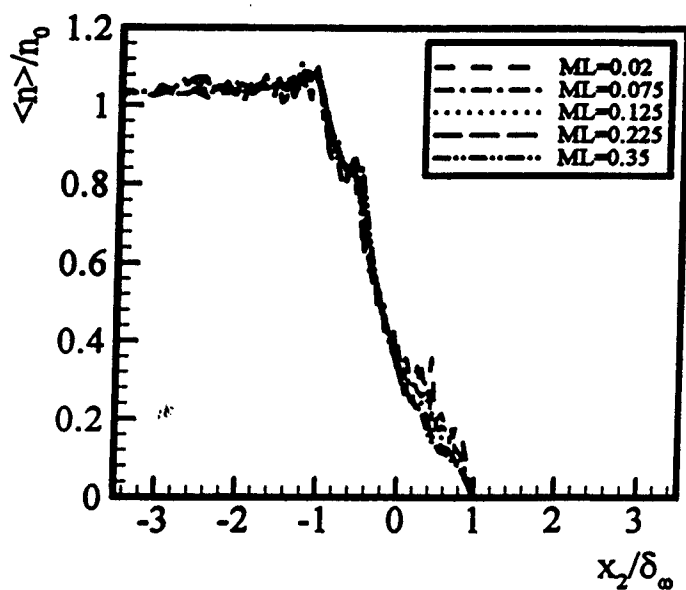


Fig. 16a

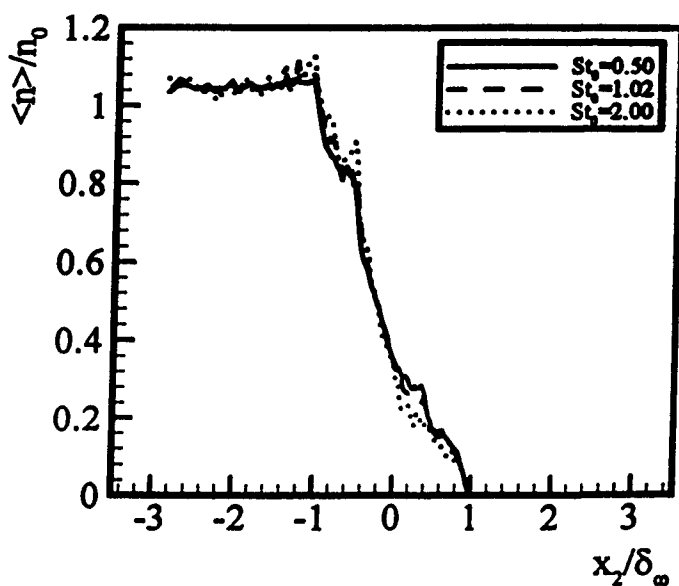


Fig. 16b

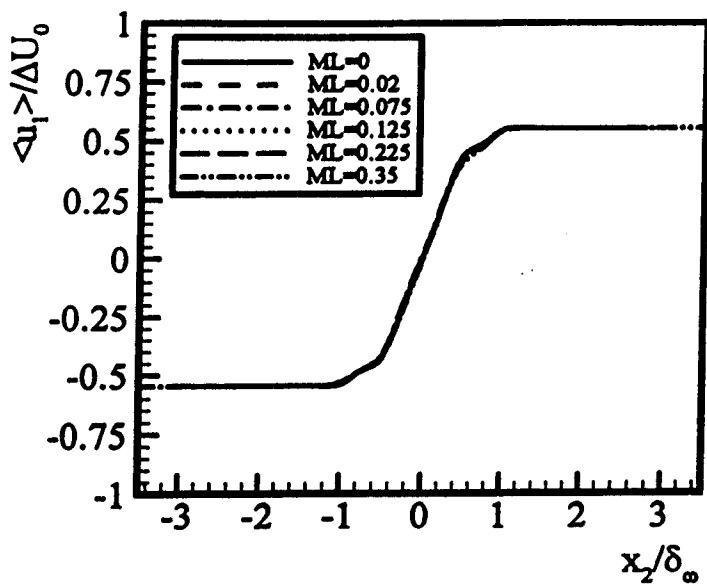


Fig. 17a

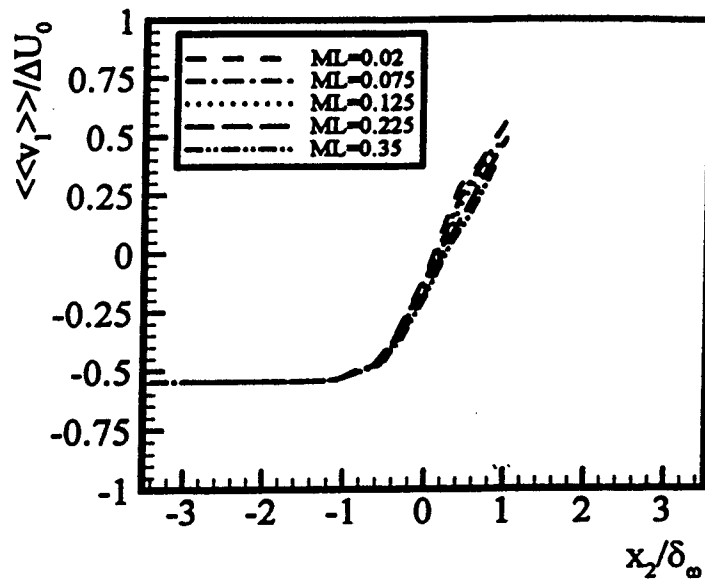


Fig. 17b

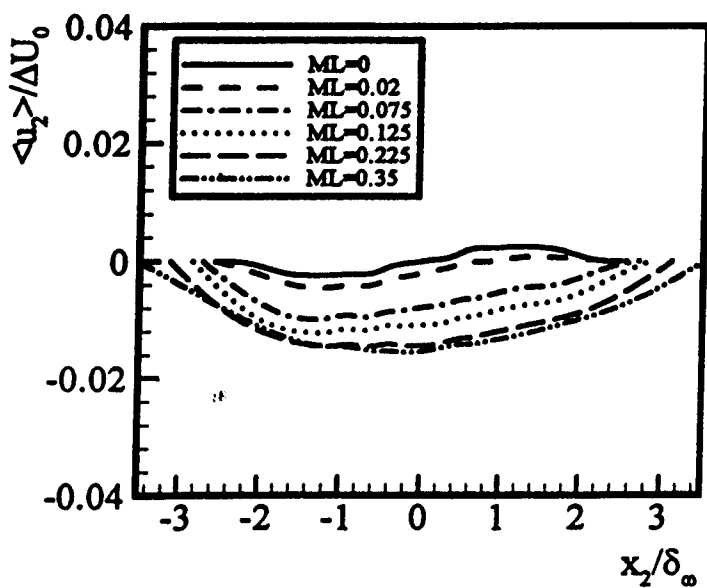


Fig. 17c

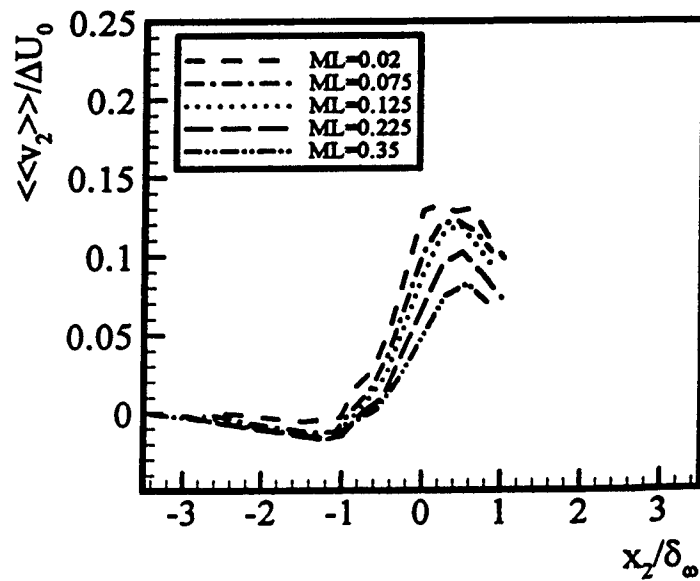


Fig. 17d

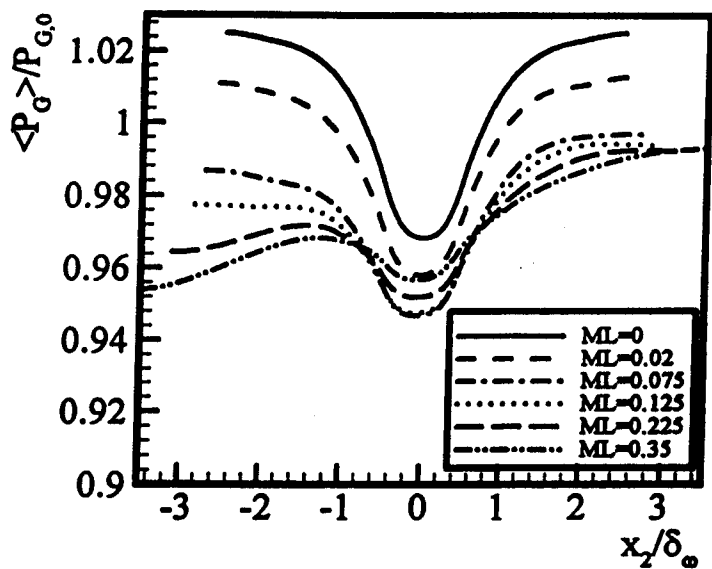


Fig. 18a

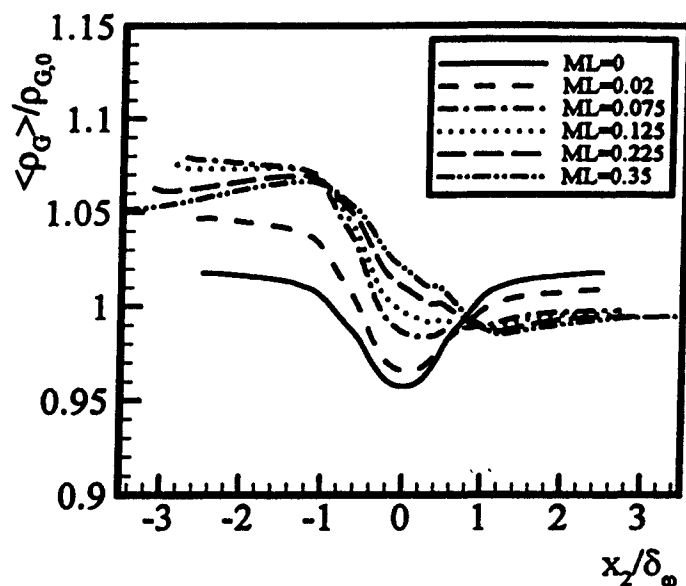


Fig. 18b

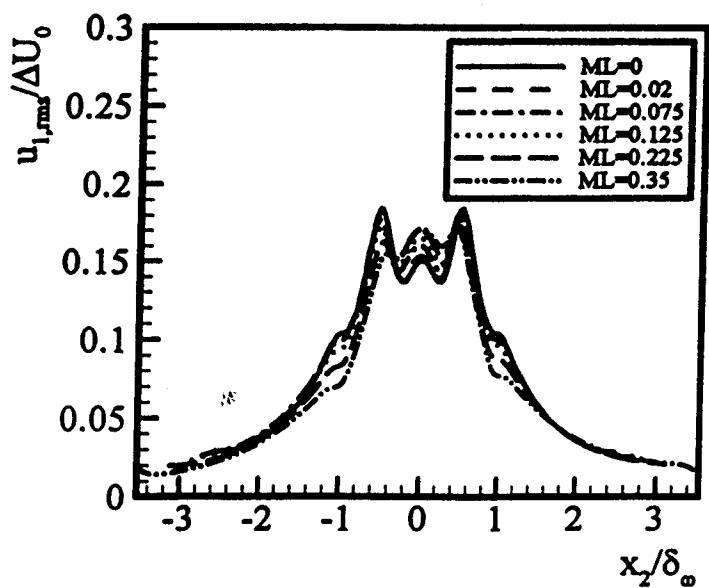


Fig. 19a

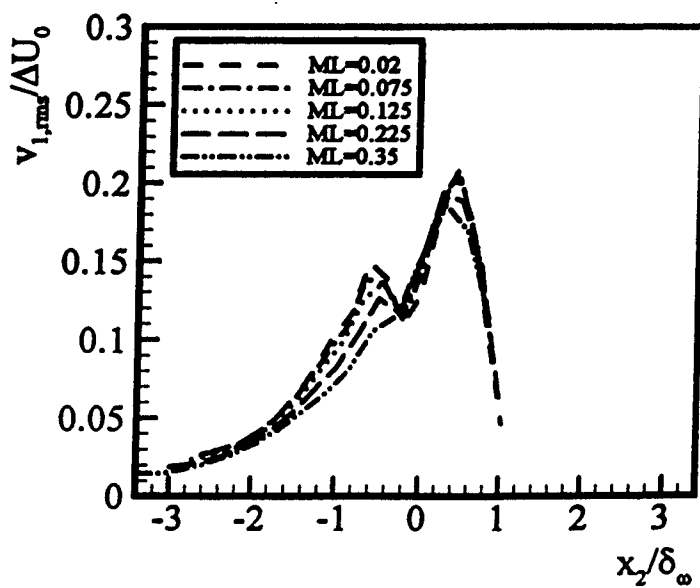


Fig. 19b

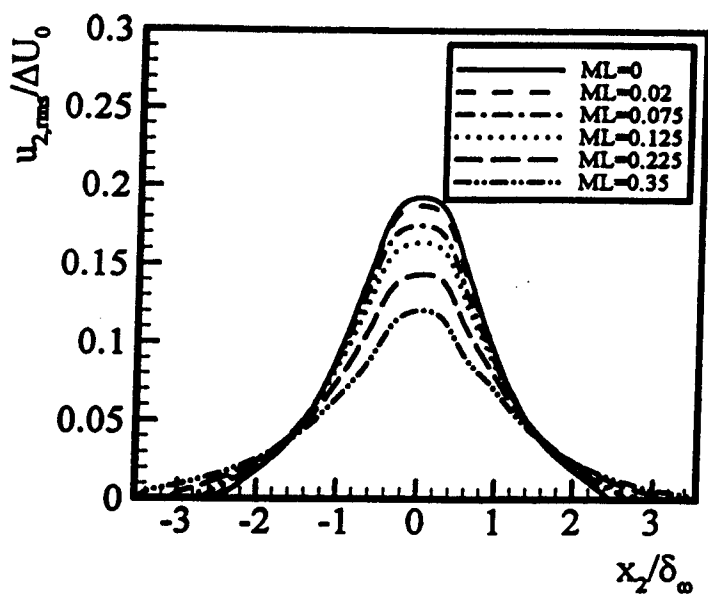


Fig. 19c

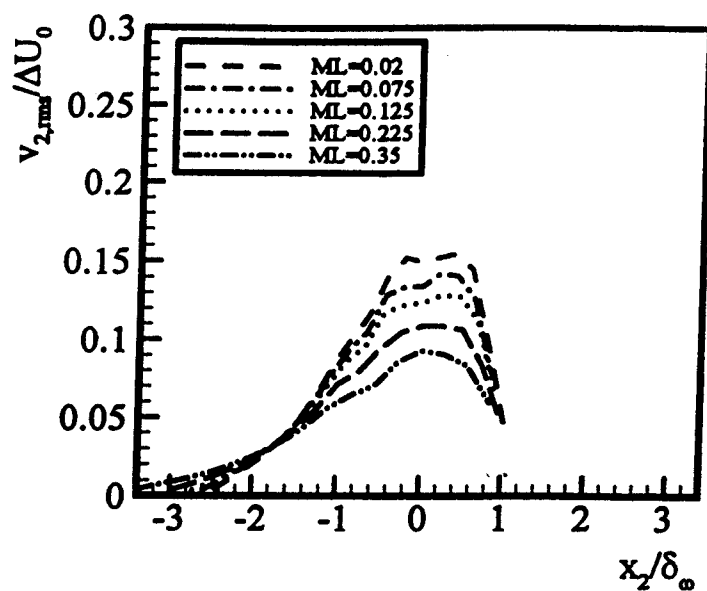


Fig. 19d

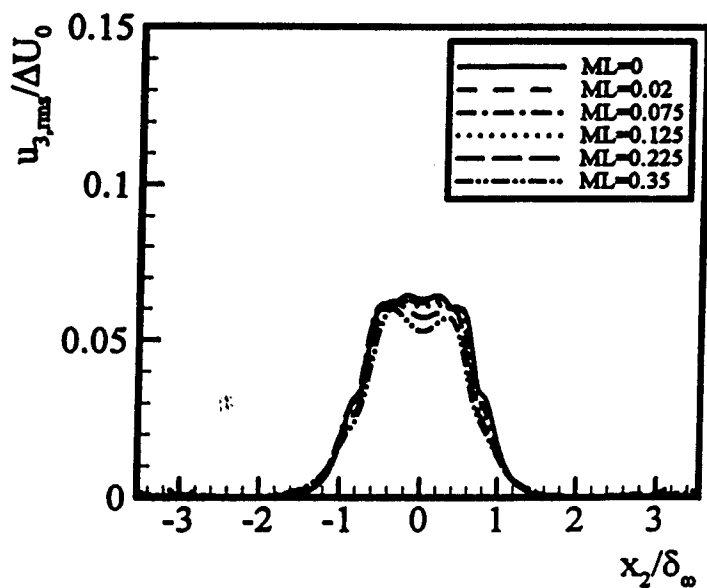


Fig. 19e

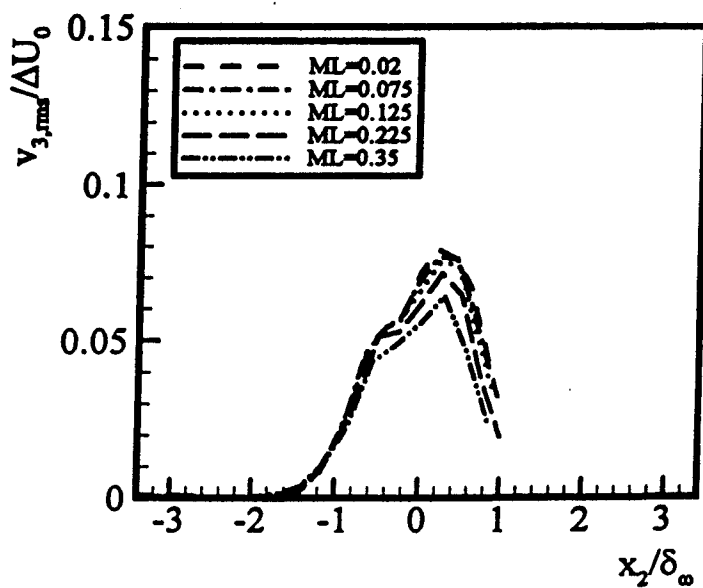


Fig. 19f

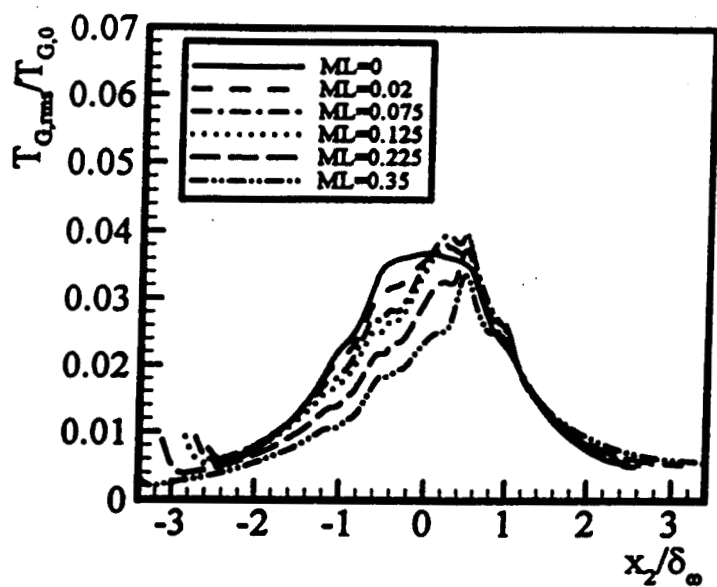


Fig. 20a

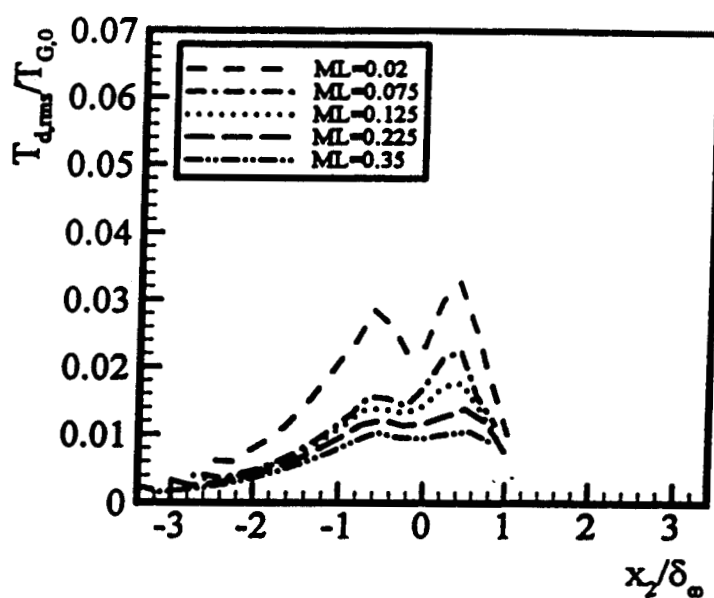


Fig. 20b

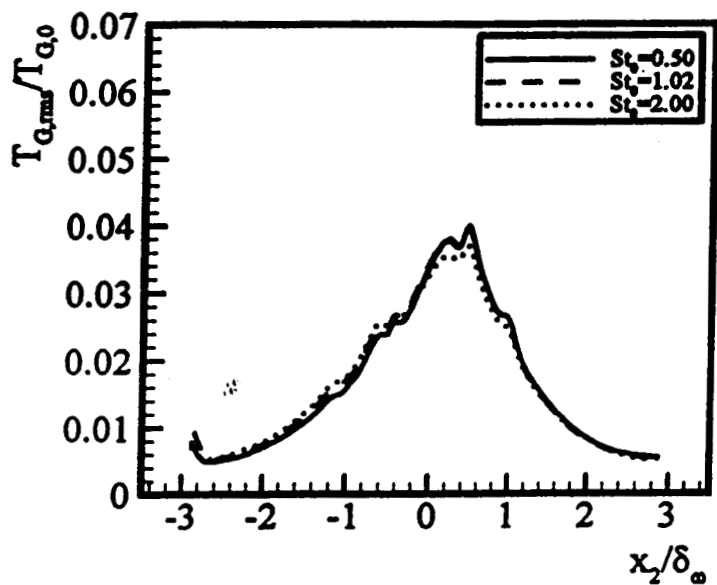


Fig. 20c

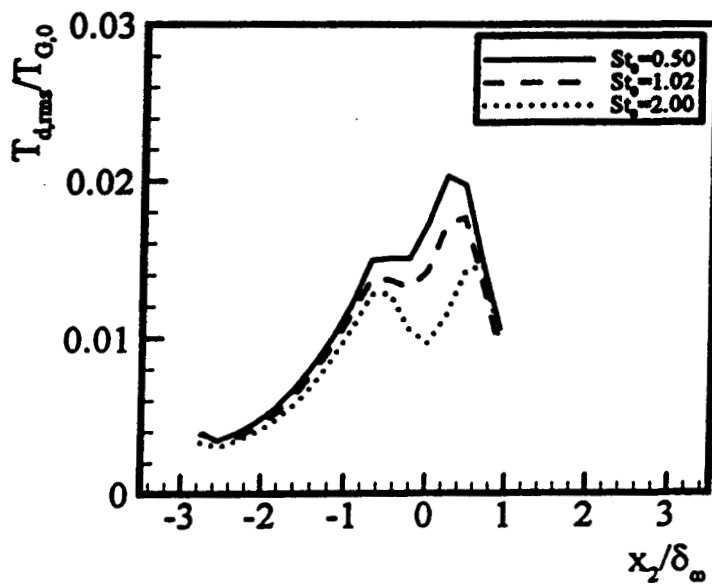


Fig. 20d